Molecular Cell
Article

The Crohn's Disease Risk Factor IRGM Limits NLRP3 Inflammasome Activation by Impeding Its Assembly and by Mediating Its Selective Autophagy

Subhash Mehto,[1,7] Kautilya Kumar Jena,[1,2,7] Parej Nath,[1,2] Swati Chauhan,[1] Srinivasa Prasad Kolapalli,[1] Saroj Kumar Das,[1,8] Pradyumna Kumar Sahoo,[1] Ashish Jain,[3,4] Gregory A. Taylor,[5,6] and Santosh Chauhan[1,9,*]
[1]Cell Biology and Infectious Diseases Unit, Institute of Life Sciences, Bhubaneswar 751023, India
[2]School of Biotechnology, KIIT University, Bhubaneswar 751024, India
[3]Department of Molecular Cell Biology, Institute for Cancer Research, Oslo University Hospital, Oslo, Norway
[4]Centre for Cancer Cell Reprogramming, Institute of Clinical Medicine, Faculty of Medicine, University of Oslo, Oslo, Norway
[5]Geriatric Research, Education, and Clinical Center, VA Medical Center, Durham, NC 27705, USA
[6]Departments of Medicine, Molecular Genetics and Microbiology, and Immunology, Division of Geriatrics and Center for the Study of Aging and Human Development, Duke University Medical Center, Durham, NC 27710, USA
[7]These authors contributed equally
[8]Present address: Centre for Biotechnology, Siksha 'O' Anusandhan (Deemed to be University), Bhubaneswar, Odisha, India
[9]Lead Contact
*Correspondence: schauhan@ils.res.in
https://doi.org/10.1016/j.molcel.2018.11.018

SUMMARY

Several large-scale genome-wide association studies genetically linked IRGM to Crohn's disease and other inflammatory disorders in which the IRGM appears to have a protective function. However, the mechanism by which IRGM accomplishes this anti-inflammatory role remains unclear. Here, we reveal that IRGM/Irgm1 is a negative regulator of the NLRP3 inflammasome activation. We show that IRGM expression, which is increased by PAMPs, DAMPs, and microbes, can suppress the pro-inflammatory responses provoked by the same stimuli. IRGM/Irgm1 negatively regulates IL-1β maturation by suppressing the activation of the NLRP3 inflammasome. Mechanistically, we show that IRGM interacts with NLRP3 and ASC and hinders inflammasome assembly by blocking their oligomerization. Further, IRGM mediates selective autophagic degradation of NLRP3 and ASC. By suppressing inflammasome activation, IRGM/Irgm1 protects from pyroptosis and gut inflammation in a Crohn's disease experimental mouse model. This study for the first time identifies the mechanism by which IRGM is protective against inflammatory disorders.

INTRODUCTION

Acute inflammation is an essential innate immune response to self-protect from harmful stimuli, including irritants and pathogens. However, a chronic inflammatory response is deleterious and leads to several inflammatory diseases (Okin and Medzhitov, 2012). Autophagy is a fundamental cell-survival process that plays a broad homeostatic role in cleaning cells by removing toxic wastes including determinants of surplus inflammation (Deretic et al., 2013; Ma et al., 2013). Recently, several studies have demonstrated the importance of autophagy in protecting against chronic inflammatory diseases (Deretic and Klionsky, 2018).

One of the most critical components of the inflammatory response are inflammasomes, which are molecular complexes that are activated by diverse danger signals of pathogenic and non-pathogenic origin, resulting in the production of the pro-inflammatory cytokines such as interleukin-1β (IL-1β) and IL-18 (Jo et al., 2016; Schroder et al., 2018). A well-studied inflammasome is composed of the NLRP3 (NACHT, LRR, and PYD domains containing protein 3) protein that complexes with ASC (PYCARD) (apoptosis-associated speck-like protein containing a CARD) to form a caspase-1-activating complex that then cleaves and activates IL-1β (Guo et al., 2015). Dysregulation of NLRP3 inflammasome has been linked with several chronic inflammatory, infectious, and autoimmune diseases (Lamkanfi and Dixit, 2012; Strowig et al., 2012). Autophagy has emerged as one of the essential processes in controlling excess inflammasome activation. By mediating the degradation of obsolete mitochondria and by degrading inflammasome components including NLRP3, autophagy keeps unnecessary and aberrant activation of inflammasomes under check (Shi et al., 2012; Yan et al., 2015; Zhong et al., 2016).

Immunity-related GTPase M (IRGM) belongs to a family of interferon-inducible GTPases (IRGs), one of the strongest cell-autonomous resistance systems to intracellular pathogens (Hunn et al., 2011). After a landmark study showing the importance of human IRGM in anti-mycobacterial autophagy (Singh et al., 2006), several genome-wide association studies identified SNPs in the *IRGM* gene and a deletion polymorphism in *IRGM* promoter region as being strongly associated with Crohn's disease (CD) and tuberculosis (Brest et al., 2011; Che et al., 2010; McCarroll et al., 2008; Parkes et al., 2007; Wellcome Trust Case Control, 2007; Craddock et al., 2010). Later, IRGM was genetically and functionally linked with several other chronic

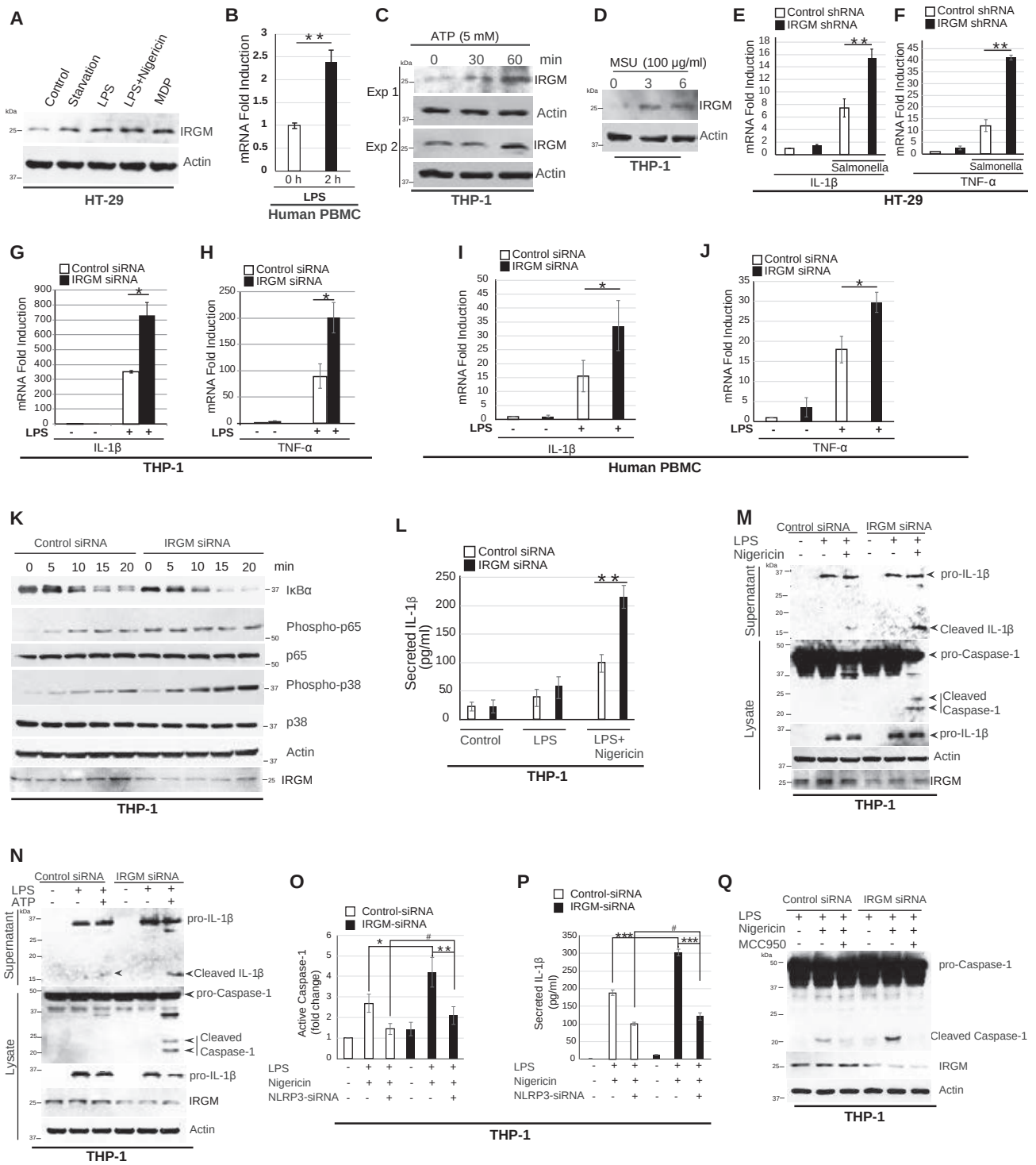

Figure 1. IRGM Suppresses Pro-inflammatory Response and NLRP3-Inflammasome Activation

(A) Human colon epithelial HT-29 cells were starved (2 hr) or stimulated with LPS (100 ng/mL, 2 hr) alone or in combination with nigericin (10 μM, 1 hr) or with MDP (10 μg/mL, 6 hr), and immunoblotting was performed with lysates.

(B) Human PBMCs from healthy volunteers were exposed to LPS (100 ng/mL), and total RNA was subjected to qRT-PCR using IRGM TaqMan probe.

(C and D) THP-1 cells were stimulated with inflammasome inducers (C) ATP or (D) MSU crystals for the indicated time periods, and extracts were subjected to western blotting with IRGM antibody.

(legend continued on next page)

inflammatory and autoimmune diseases (Baskaran et al., 2014; Burada et al., 2012; Glas et al., 2013; Yang et al., 2014). Given the linkage of IRGM with so many inflammatory and autoimmune disorders, it is surprising that IRGM's mechanism of action in regulating inflammation remains unclear.

In this study, our work reveals that human IRGM and its mice ortholog Irgm1 control inflammation by suppressing the activation of NLRP3 inflammasomes. Mechanistically, we found that IRGM physically complexes with NLRP3 inflammasome components and obstructs inflammasome assembly. IRGM interacts with SQSTM1/p62 (henceforth, p62) and mediates p62-dependent selective autophagy of NLRP3 and ASC. Thus, by restricting inflammasome activity, IRGM protects from pyroptosis. Further, we found that mouse Irgm1 suppresses the colon inflammation by inhibiting NLRP3 inflammasome in a DSS-induced colitis mouse model. Taken together, this work identifies a direct role of IRGM in suppressing the inflammation and provides a basis for its protective role in inflammatory diseases including Crohn's.

RESULTS

Human IRGM Suppresses Pro-inflammatory Cytokine Response

Human *IRGM* is mainly expressed in cells of myeloid and epithelial origin, and this expression is increased following exposure of interferon (IFN)-γ (Chauhan et al., 2015). IRGM expression in the colon epithelial cell line HT-29 is increased under starvation conditions and by treatment of cells with the pathogen-associated-molecular-patterns (PAMPs) such as lipopolysaccharide (LPS) and muramyl dipeptide (MDP) (Figures 1A and S1A). In human peripheral blood mononuclear cells (PBMCs), IRGM expression was increased on treatment with LPS (Figure 1B). Further, the treatment of THP-1 cells with danger-associated molecular patterns (DAMPs) such as ATP, MSU (Monosodium urate), and cholesterol crystals increased protein expression of IRGM (Figures 1C, 1D, and S1B). The expression of IRGM was increased on infection of THP-1 cells with *Salmonella typhimurium* (SL1433) (Figure S1C). Thus, *IRGM* expression is induced by DAMPs, PAMPs, and microbes in innate immune cells.

Next, we investigated the role of IRGM in modulating the pro-inflammatory responses induced by LPS treatment and by Salmonella infection. The control and IRGM stable knockdown HT-29 human colon epithelial cells were infected with *Salmonella typhimurium*, and the expression of sentinel pro-inflammatory genes *Il1b*, *Tnfa*, *Il18*, and *Rantes* were monitored by qRT-PCR. As compared to the control cells, IRGM-depleted cells mounted a stronger pro-inflammatory response (Figures 1E, 1F, S1D, and S1E). Similarly, in THP-1 cells, the LPS induced *Il1b* and *Tnfa*, expression was further increased in IRGM small interfering RNA (siRNA) knockdown cells (Figures 1G and 1H). In these cells, *Il18* expression was increased but not significantly, and *Rantes* expression was not affected (Figures S1F and S1G). Further, human PBMCs from healthy donors showed enhanced production of pro-inflammatory cytokine *Il1b* and *Tnfa* when IRGM was knockdown (Figures 1I and 1J). Furthermore, the secretion of IL-6 and tumor necrosis factor alpha (TNF-α) was significantly higher in IRGM-depleted THP-1 cells as compared to the control cells (Figures S1H and S1I). Taken together, the data suggest that IRGM suppresses the pro-inflammatory cytokine response.

To determine the pro-inflammatory signaling pathway controlled by IRGM, we performed a time-course experiment of LPS treatment in control and IRGM-depleted THP-1 cells. As compared to the control cells, the IRGM-depleted cells have lesser IκBα that was degraded faster with LPS treatment (Figure 1K). In the agreement, phospho-NF-κB-p65 levels were higher in IRGM-depleted cells at all the time points (Figure 1K). A previous study in mice indicated the role of p38 MAPK signaling pathway in Irgm1-mediated LPS (TLR4) induced a pro-inflammatory cytokine response (Bafica et al., 2007). Here, in human cells, we found a similar increase in phospho-p38 in IRGM knockdown cells compared to control cells (Figure 1K) suggesting that human IRGM inhibit both NF-κB and p38 MAPK pro-inflammatory signaling pathways to control pro-inflammatory cytokine response.

We note that our several attempts to generate an IRGM knockout human monocytic cell line or a colon epithelial cell lines by different CRISPR-CAS9 methods were unsuccessful. Consequently, in this study, we used siRNA (THP-1 and PBMCs) or small hairpin RNA (shRNA) (HT-29 cells) to transiently or stably knock down the human IRGM; typical knockdown efficiency in any given cell or cell line (PBMC, THP-1, HT-29) was found to be 40%–60% (Figures S1J–S1L).

IRGM Limits NLRP3 Inflammasome Activation

IL-1β is translated as pro-IL-1β that stays in inactivated form until a second signal activates inflammasomes leading to pro-IL-1β

(E and F) HT-29 control and IRGM knockdown cells were infected with *S. typhimurium* (1:10 MOI, 8 hr), and the total RNA was subjected to qRT-PCR with (E) IL-1β and (F) TNF-α.

(G–J) The total RNA isolated from the LPS-stimulated (100 ng/mL, 2 hr) control and IRGM siRNA-transfected (G and H) THP-1 cells or (I and J) PBMCs from five healthy donors were subjected to qRT-PCR for the indicated genes. For (G) and (H), n = 3, mean ± SE, *p < 0.05, Student's unpaired t test. For (I) and (J), n = 5, mean ± SE, *p < 0.05, Student's paired t test.

(K) The LPS (500 ng/mL)-stimulated control and IRGM siRNA-transfected THP-1 cell lysates were subjected to immunoblotting with indicated antibodies.

(L) The supernatants from control and IRGM siRNA-transfected THP-1 cells, which were stimulated with LPS (100 ng/mL, 4 hr) alone or in combination with nigericin (5 μM, 30 min), were subjected to ELISA with IL-1β antibody.

(M and N) The western blotting was performed with control and IRGM siRNA-transfected THP-1 cells, which were stimulated with LPS (1 μg/mL for 3 hr) alone or in combination (M) with nigericin (5 μM, 30 min) or (N) with ATP (2.5 mM, 4 hr).

(O and P) Quantification of (O) active caspase-1 (FLICA assay) and (P) secreted IL-1β (ELISA) in THP-1 cells transfected with control, IRGM, and NLRP3 siRNA and treated with LPS (1 μg/mL, 3 hr) and nigericin (5 μM, 15 min).

(Q) The control and IRGM siRNA-transfected THP-1 cells were treated with LPS (1 μg/mL, 3 hr), nigericin (5 μM, 15 min), or MCC950 (1 μM) as indicated, and western blotting was performed.

Unless otherwise stated above, n = 3, mean ± SD, *p < 0.05, **p < 0.005, ***p < 0.0005, #insignificant, Student's unpaired t test. See also Figure S1.

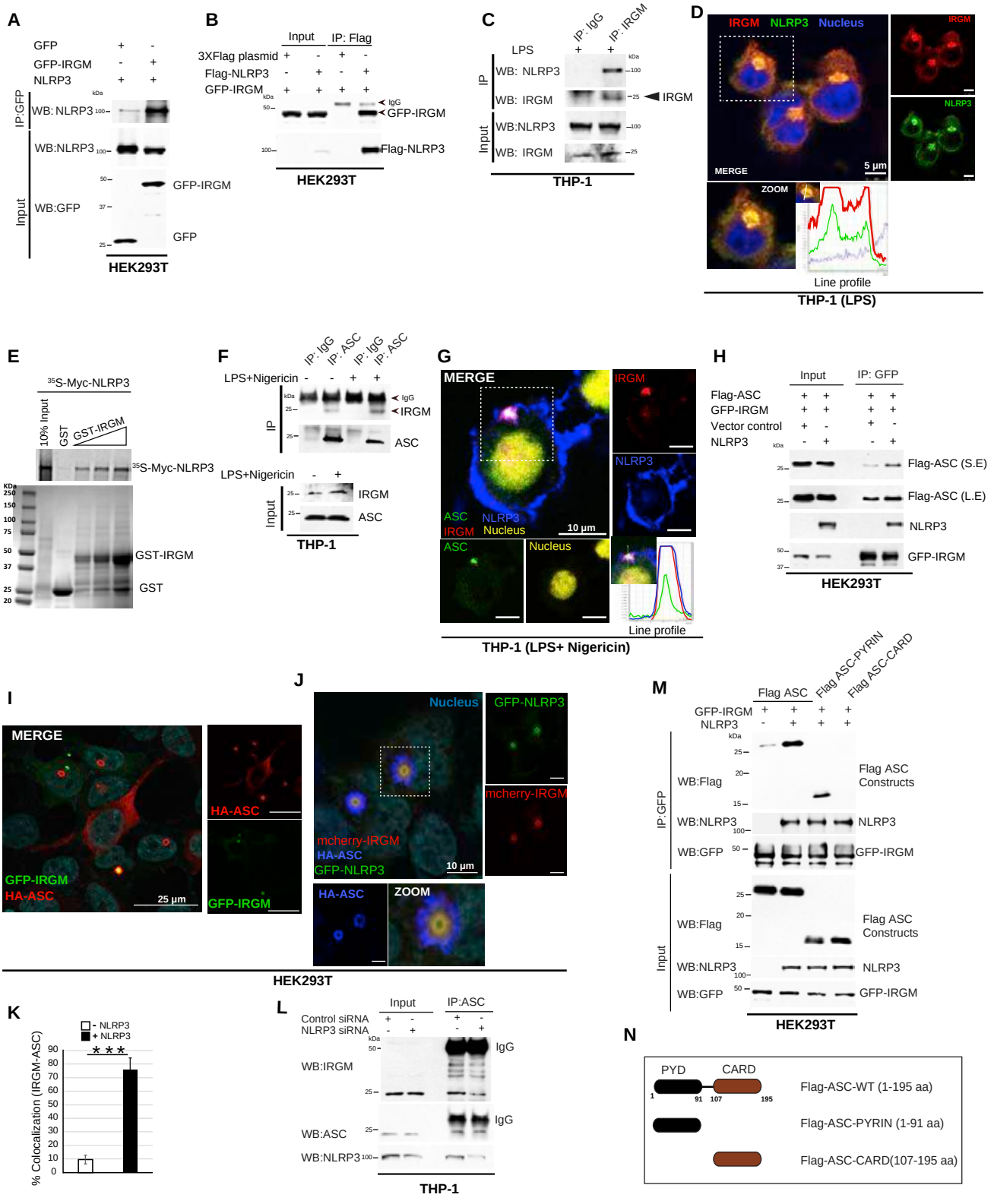

Figure 2. IRGM Interacts and Co-localizes with NLRP3 Inflammasome Components

(A and B) Co-immunoprecipitation (coIP) analysis of interaction between (A) GFP-IRGM and NLRP3 or (B) Flag-NLRP3 and GFP-IRGM in HEK293T cells lysates. (C) IP analysis of interaction between endogenous IRGM and NLRP3 in LPS-stimulated THP-1 cells.

(legend continued on next page)

cleavage by caspase-1 to a mature form that is secreted (Choi and Ryter, 2014). We next investigated whether IRGM controls the levels of secreted IL-1β. In ELISA assays, the secreted IL-1β levels were significantly increased on silencing IRGM (Figure 1L) indicating that IRGM suppresses IL-1β cleavage and secretion. The treatment of THP-1 cells with LPS and the inflammasome inducers nigericin (Figure 1M) or ATP (Figure 1N) resulted in increased cleavage of caspase-1 and IL-1β in IRGM-depleted cells compared to the control cells. The results indicate that IRGM suppresses the cleavage of caspase-1 and IL-1β presumably by suppressing NLRP3 inflammasome. We validated this notion by depleting (by siRNA) and inhibiting (by MCC950) the NLRP3 in IRGM knockdown cells. The enhanced inflammasome activation in IRGM-depleted THP-1 cells was blunted when NLRP3 was depleted or inhibited (Figures 1O–1Q and S1M) suggesting that IRGM inhibits NLRP3 activity to suppress activation of caspase-1 and IL-1β.

IRGM Interacts and Co-localizes with NLRP3 and ASC over the Inflammasomes

Several diverse signals can activate NLRP3 leading to the oligomerization of NLRP3, the adaptor protein ASC, and the caspase-1 enzyme for the assembly of an activated inflammasome (Choi and Ryter, 2014). Since we found that IRGM suppresses cleavage of caspase-1 and IL-1β, next, we examined the mechanism by which IRGM suppresses the activity of NLRP3 inflammasome. First, we investigated whether IRGM physically associates with inflammasome components. In immunoprecipitation assays, IRGM strongly interacted with both exogenous and endogenous NLRP3 (Figures 2A–2C and S1N). The endogenous IRGM and NLRP3 interacted in THP-1 monocytes (Figure 2C), and the interaction was increased in the presence of *Salmonella typhimurium* (Figure S1N). Endogenous as well as exogenously expressed IRGM was found to be completely co-localized with the NLRP3 in the perinuclear regions of the cells (Figures 2D, S1O, and S1P). In GST pull-down assays, purified IRGM directly interacted with NLRP3 in a concentration-dependent manner (Figure 2E). Taken together, the data suggest that IRGM directly interacts and co-localizes with NLRP3.

On inflammasome activation, ASC oligomerizes with itself and with NLRP3 and caspase-1 to form an active inflammasome complex. In immunoprecipitation assays, performed in THP-1 cells, IRGM interacted with ASC, both under basal and inflammasome-inducing conditions (Figure 2F). ASC formed distinct specks in the cells that are hallmarks of inflammasome activation. Under inflammasome-inducing conditions, IRGM co-localized with ASC and NLRP3 in the core region of specks (Figures 2G, S1Q, and S1R). In co-immunoprecipitation (coIP) experiments, IRGM interacted with ASC, and this interaction was increased when NLRP3 was co-expressed (Figure 2H). In agreement with this, the co-localization of overexpressed ASC structures and IRGM was dramatically increased when NLRP3 was co-expressed (Figures 2I–2K). Also, the depletion of NLRP3 reduced the ASC-IRGM interaction (Figure 2L). The data show that NLRP3 is important for bridging IRGM and ASC. Next, in a domain-mapping experiment, we found that IRGM interacts with PYRIN domain but not with the CARD domain of ASC (Figures 2M and 2N). The PYRIN is the oligomerization domain of ASC. Taken together, the data suggest that IRGM is part of NLRP3 inflammasome where it complexes with both NLRP3 and ASC.

IRGM Interferes with NLRP3 Inflammasome Assembly

To further understand the details of the NLRP3-IRGM interaction, we mapped the binding of IRGM to functional domains in NLRP3 (Figure 3A). NLRP3 is composed of PYRIN, NACHT (nucleotide binding domain or NBD), and LRR domains (Figure 3A). We found that IRGM predominantly interacted with the NACHT domain (Figure 3A). A weak interaction with LRR and almost negligible interaction with PYRIN domain were observed (Figure 3A). The NACHT domain of NLRP3 is an ATP binding domain with an ATPase activity (Duncan et al., 2007). An intact NACHT domain of NLRP3 is required for its oligomerization and activation (Duncan et al., 2007). Hence, we examined whether IRGM perturbs the oligomerization of NLRP3. Indeed, in crosslinking experiments, IRGM depletion was sufficient to increase oligomerization of NLRP3 (Figure 3B). In contrast, the oligomeric forms of overexpressed NLRP3 were reduced when IRGM was overexpressed (Figure 3C). Further, in coIP assays, IRGM was able to reduce homotypic interaction between FLAG-NLRP3 and GFP-NLRP3 (Figure 3D). Furthermore, overexpression of IRGM reduced the interaction between full-length NLRP3 and NACHT domain (Figure 3E) and also between FLAG-NACHT and mCherry-NACHT suggesting that IRGM disrupts the homo-oligomerization of the NLRP3 (Figure 3F). In immunofluorescence assays, the size of NLRP3 aggregates was reduced in the presence of IRGM (Figures S2A–S2C). Altogether, the data show that IRGM restricts the oligomerization of NLRP3.

ASC possess prion-like properties of self-association and forms branched fiber-like structure important for inflammasome activation (Cai et al., 2014). A high-resolution microscopy of ASC specks in THP-1 cells revealed a significantly larger and branched ASC specks in IRGM knockdown cells compared to

(D) Representative confocal images of THP-1 macrophages, treated with LPS and processed for immunofluorescence (IF) analysis.
(E) GST pull-down assay of in-vitro-translated and radiolabeled myc-tagged NLRP3 with GST or GST-tagged IRGM.
(F) IP analysis of interaction between endogenous IRGM and ASC in LPS+nigericin-treated THP-1 cells.
(G) Representative confocal images of THP-1 cells, treated with LPS (1 μg/mL, 3 hr) and nigericin (5 μM, 30 min) and processed for IF analysis.
(H) CoIP analysis of interaction between IRGM and ASC in HEK293T cell lysates in absence and in presence of NLRP3. S.E., short exposure; L.E., long exposure.
(I and J) Representative confocal images of HEK293T cells transiently expressing (I) GFP-IRGM and HA-ASC and (J) GFP-NLRP3, mcherry-IRGM, and HA-ASC.
(K) The graph depicts percentage co-localization of ASC specks with IRGM in the absence and presence of NLRP3 (n = 3, mean ± SD, ***$p < 0.0005$).
(L) IP analysis of the interaction between endogenous IRGM and ASC in THP1 cells transfected with control siRNA or NLRP3 siRNA.
(M) CoIP analysis to map the interaction of ASC domains with IRGM in HEK293T cell lysates.
(N) The domain organization map of ASC and deletion constructs cloned as FLAG-tagged proteins. Scale bars are indicated in the respective figures.
See also Figure S1.

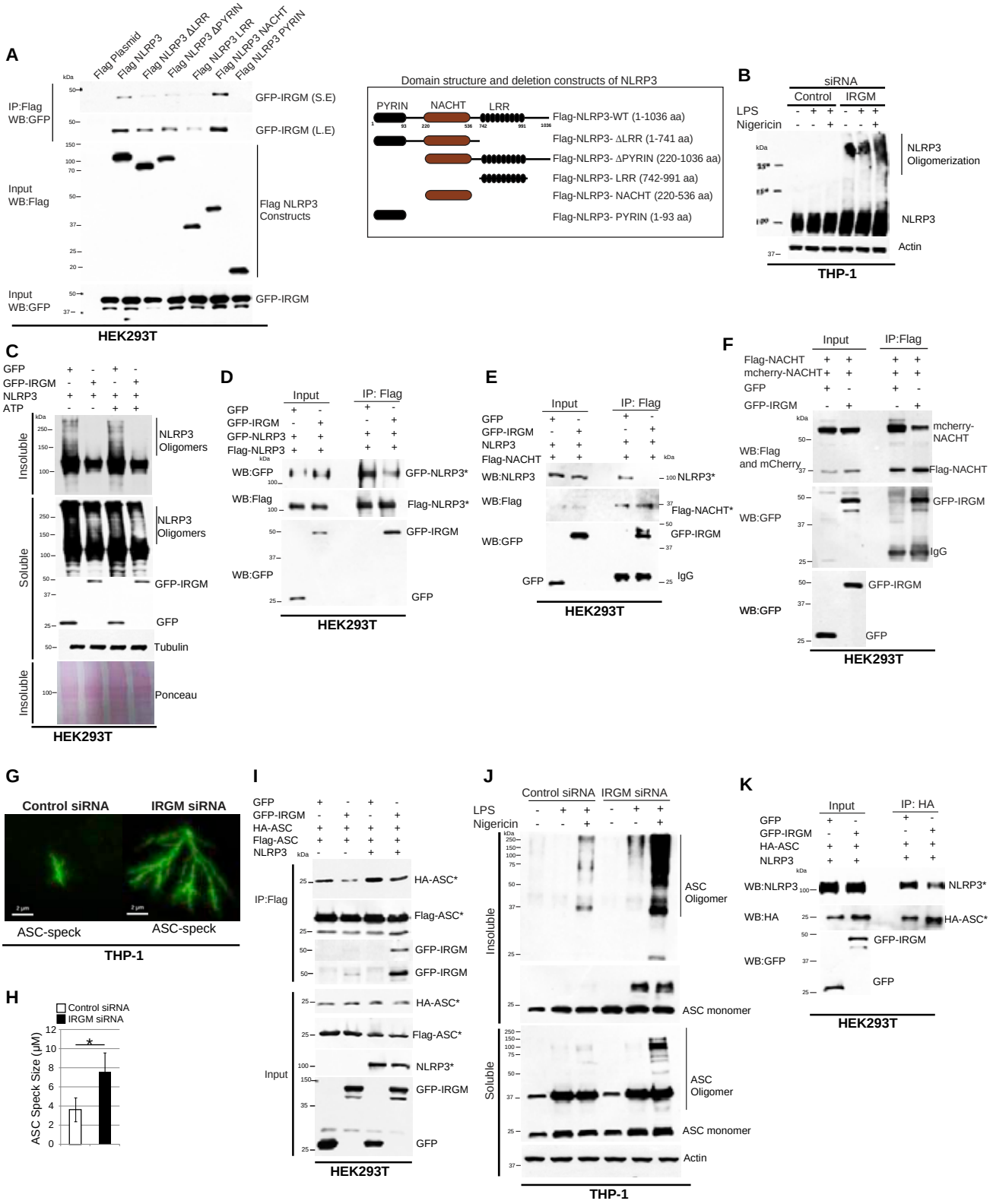

(legend on next page)

the control cells (Figures 3G and 3H). In contrast, when IRGM was overexpressed, ASC specks were found to be significantly smaller in overexpressing cells compared to the control cells (Figures S2D–2F). The data indicate that IRGM suppresses the polymerization of ASC. To corroborate these findings, we performed biochemical assays. In coIP experiments, the overexpression of IRGM reduced interaction between HA-ASC and FLAG-ASC (Figure 3I). In western blotting experiments performed with cross-linked insoluble cellular fraction, ASC oligomerization was inhibited by overexpression of IRGM (Figure S2G). In contrast, the amount of oligomerized ASC in the insoluble fraction of the THP-1 cells was markedly increased in IRGM knockdown cells compared to the control cells (Figure 3J). Taken together, these results suggest that IRGM obstructs the oligomerization of ASC also. The interaction between NLRP3 and ASC was also reduced in the presence of IRGM (Figure 3K, see also Figure 5E), but the interaction between ASC and caspase-1 was unaffected by IRGM (Figure S2H). Overall, we found that IRGM restricts assembly of the inflammasome by impeding the homo- and hetero-oligomerization of NLRP3 and ASC.

IRGM Mediates Autophagic Degradation of NLRP3 Inflammasome Components

We found that the overexpression of IRGM reduced NLRP3 levels (Figure 4A, S2I, and S2J), while silencing IRGM by siRNA increased the total amount of endogenous NLRP3 (Figures 4B and S2K). The data indicate that IRGM mediates degradation of the NLRP3 protein.

NLRP3 is known to be degraded by both the proteasome and autophagy (Kimura et al., 2015; Song et al., 2016). The Bafilomycin A1 (BafA1, an autophagy inhibitor), but not MG132 (a proteasome inhibitor), was able to restore the IRGM-mediated degradation of NLRP3 indicating a role for autophagy in the degradation process (Figures 4C and S2L). In the absence of the essential autophagy proteins, ATG5 or ATG7, IRGM was not able to degrade NLRP3 (Figures 4D–4G and S2M) suggesting that IRGM degrades NLRP3 via autophagy process.

ASC as a part of an inflammasome was previously shown to be degraded by autophagy (Shi et al., 2012). Here, we found that overexpression of IRGM reduced ASC protein levels (Figures 4H and S2N), while IRGM depletion resulted in increased ASC amounts (Figures 4I and S2O). This finding was further supported by immunofluorescence experiments showing that the LPS and nigericin-induced ASC specks (inflammasomes) were significantly increased in number on knocking down IRGM (Figures S2P and S2Q). In contrast, overexpression of IRGM significantly reduced the total number of ASC specks (Figures S2R and S2S). These data suggest that IRGM mediates degradation of ASC. This degradation was completely restored in the presence of BafA1, but only partly in the presence of MG132 (Figures 4J and S2T). In the absence of ATG5 or ATG7, IRGM was not able to degrade ASC (Figures 4F and 4G) suggesting that IRGM degrades ASC via autophagy process.

IRGM Mediates p62-Dependent Selective Autophagy of NLRP3 Inflammasomes

p62 is a selective autophagy adaptor protein that plays a vital role in autophagic degradation of several inflammatory signaling pathway proteins including inflammasomes and their components (Chen et al., 2016; Samie et al., 2018; Shi et al., 2012). Here, we explored whether IRGM acts as a scaffold protein to mediate p62-dependent selective autophagy of NLRP3. We found that IRGM interacted and co-localized with p62 (Figures 4K and 4L). IRGM was also required for expression of p62 under basal and inflammasome-inducing conditions in THP-1 cells (Figure S3A). NLRP3 itself can interact and co-localize with p62 (Figures S3B–3D). In THP-1 cells, p62 was co-localized with NLRP3 (Figure S3D) on perinuclear structures that appeared similar to those on which IRGM and NLRP3 co-localized (Figure 2D) suggesting that all the three proteins are part of the same complex. In HEK293T cells, overexpressed IRGM, p62, and NLRP3 co-localized with each other suggesting that they are indeed in a single complex (Figure 4M). IRGM increased the interaction of p62 with both NLRP3 (Figures 4N and 4O) and ASC (Figure 4P) suggesting that IRGM is vital for bridging p62 with NLRP3- and ASC-containing inflammasomes.

Next, we asked whether p62 as a part of the IRGM-p62-NLRP3 complex is required for IRGM-mediated autophagic degradation of NLRP3. Indeed, depletion of p62 by siRNA restored IRGM-mediated NLRP3 degradation (Figures 4Q and S3E). ULK1 plays an important role in autophagy initiation, whereas Beclin1 and ATG16L1 are required for autophagosome assembly and elongation. Since IRGM interacts with ULK1, Beclin 1, and ATG16L1 for assembly of the autophagy

Figure 3. IRGM Impedes the Homo- and Hetero-oligomerization of NLRP3 and ASC

(A) Left panel, coIP analysis to map the binding of IRGM over the NLRP3 domains in HEK293T cell lysates. Right panel, the domain organization map of NLRP3 and deletion constructs cloned as FLAG-tagged proteins. S.E., short exposure; L.E., long exposure.

(B) The western blotting analysis of DSS cross-linked insoluble fraction of LPS and nigericin-treated control and IRGM knockdown THP-1 cells.

(C) The soluble and insoluble fractions of DSS cross-linked HEK293T cells lysates expressing NLRP3 and GFP or GFP-IRGM were subjected to western blotting.

(D–F) CoIP analysis of interaction between (D) FLAG-NLRP3 and GFP-NLRP3, (E) FLAG-NLRP3-NACHT and NLRP3, and (F) FLAG-NLRP3-NACHT and mcherrry-NLRP3-NACHT in the absence and presence of GFP-IRGM in HEK293T cells lysates.

(G) Super-resolution micrograph of control and IRGM siRNA-transfected THP-1 cells stably expressing LPS-inducible GFP-ASC.

(H) Average ASC speck size measured (n = 2, mean ± SD [40 specks], *$p < 0.05$).

(I) IP analysis from HEK293T cell lysates expressing HA-ASC, FLAG-ASC, and NLRP3 along with GFP control vector or GFP-IRGM vector.

(J) The western blot analysis with DSS cross-linked insoluble fraction and soluble fractions of control and IRGM knockdown THP-1 cells stimulated with LPS (1 μg/mL, 3 hr) and nigericin (5 μM, 15 min).

(K) IP analysis of interaction between NLRP3 and ASC in the absence and presence of GFP-IRGM.

*In order to reduce the artifact coming from IRGM-mediated degradation of NLRP3 and ASC, the inputs ratios were adjusted to have equal inputs in both the conditions and the IP samples were run in the same ratios as of the inputs.

Scale bars are as indicated in figures. See also Figure S2.

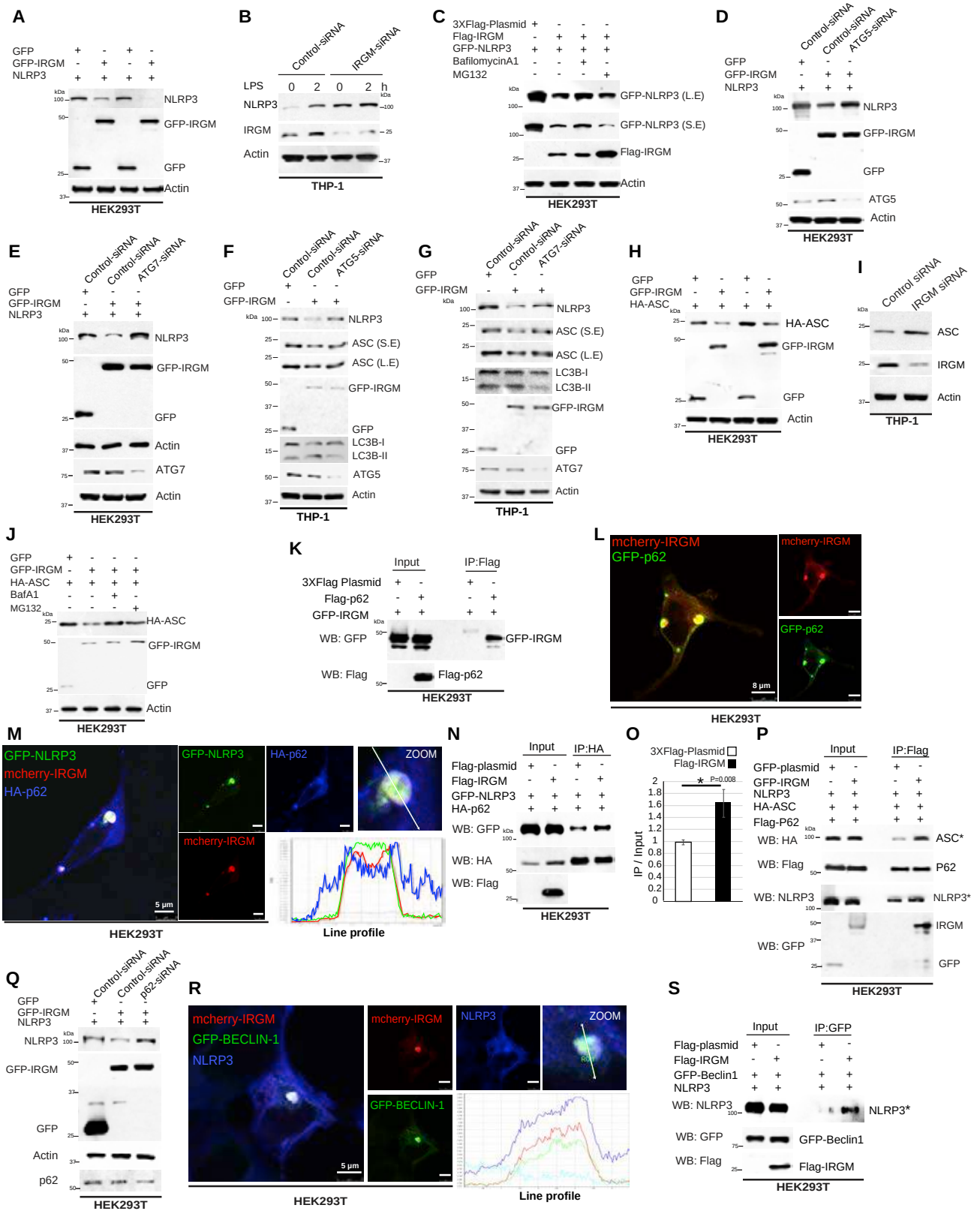

(legend on next page)

machinery (Chauhan et al., 2015), we next asked which of these autophagy proteins are utilized by IRGM for autophagy of NLRP3. NLRP3 and IRGM co-localized with all three autophagy regulatory proteins (Figures 4R, S3F, and S3G). Further, in coIP experiments, IRGM robustly increased NLRP3-Beclin1 and NLRP3-ATG16L1 interactions (Figures 4S and S3H) but did not affect NLRP3-ULK1 interaction (Figure S3I). Taken together, the data suggested a scaffolding role for IRGM in bringing the autophagy adaptor protein (p62), autophagy initiation (Beclin 1), and elongation protein (ATG16L1) over the NLRP3 inflammasomes.

We performed time-chase immunofluorescence experiments to understand whether the p62 docks to NLRP3/ASC complex first or the Beclin1/ATG16L1 reaches the complex first. The IRGM-p62-ASC showed co-localization in 5 min of stimulation, whereas ATG16L1 came later at 15 min or more prominently on 30 min post stimulation (Figures S4A and S4B). We also performed time-chase immunofluorescence experiments in overexpression system in HEK293T cells. The data show that, in the presence of p62, the NLRP3-IRGM puncta formation are fast, and all three p62, IRGM, and NLRP3 co-localized with each other 6 hr post-transfection (Figures S4C and S4D), whereas in the presence of Beclin1 the IRGM-NLRP3 complex appeared at 12 hr post-transfection (Figures S4C and S4D). Taken together, the data suggest that p62 being an adaptor protein recognizes the inflammasome first followed by docking of other autophagy proteins.

NLRC4 and AIM2 are other well-studied inflammasomes. The NLRC4 levels were unchanged, whereas, surprisingly, AIM2 levels were decreased on knocking down IRGM (Figures 5A and 5B). However, the overexpression of IRGM did not significantly affect the levels of overexpressed AIM2 in HEK293T (Figures S5C and S5D) suggesting that the reduction in AIM2 expression observed in IRGM knockdown THP-1 cells is not a direct effect of IRGM low expression but could be a secondary event. This notion is supported by negligible AIM2-IRGM co-localization (Figures S5E and S5F). Taken together, our data show that AIM2 or NLRC4 are not degraded by IRGM-mediated selective autophagy, and the discovered mechanism is specific to NLRP3.

Next, we investigated whether the LPS and inflammasome activator-induced general autophagy flux is controlled by IRGM. The results suggest that LPS-, LPS+nigericin-, and LPS+ATP-induced autophagy flux is inhibited upon IRGM depletion (Figures 5A and 5B), whereas the LPS+poly(dA-dT) (an AIM2 inflammasome inducer)-induced autophagy flux was not affected by knockdown of IRGM (Figure S5G).

IRGM mediates selective autophagy of NLRP3 and ASC and also regulates basal autophagy. We asked whether IRGM itself is an autophagy target. In cycloheximide chase experiments, we found that MG132 but not BafA1 could protect IRGM from degradation suggesting that IRGM is degraded by proteasome but not by the autophagy (Figures S5H and S5I).

Two Distinct Mechanisms Governed by IRGM Regulate NLRP3 Inflammasome Suppression

IRGM utilizes two mechanisms: (1) suppression of oligomerization and (2) autophagic degradation of NLRP3/ASC to inhibit the inflammasome activation. Next, we performed experiments to determine whether these two mechanisms are distinct or dependent on each other. In oligomerization assays, in the presence of autophagy inhibitor chloroquine, although the IRGM-mediated degradation of NLRP3 and ASC monomers (soluble fraction) was significantly restored, the oligomerization defect of NLRP3 and ASC was not rescued (Figures 5C and 5D). These data indicate that the IRGM-mediated autophagic degradation of NLRP3 and ASC is independent of IRGM-regulated inhibition of oligomerization. Next, we found that IRGM was able to inhibit the oligomerization of NLRP3, as well as ASC even in the presence of autophagy inhibitor (Figures 5E and 5F) suggesting that IRGM-mediated oligomerization defect is independent of IRGM-controlled autophagic degradation of NLRP3 and ASC.

A recent study showed that a single mutation in the GTPase domain (S47N) of IRGM makes it incompetent in interaction

Figure 4. IRGM Mediates Autophagic Degradation of NLRP3 and ASC

(A) Western blotting experiment with HEK293T cells expressing NLRP3 and GFP or GFP-IRGM plasmids.
(B) Western blot analysis with untreated or LPS-treated (100 ng/mL, 2 hr) control or IRGM siRNA-transfected THP-1 cells lysates.
(C) HEK293T cells expressing FLAG control vector, FLAG-IRGM, and GFP-NLRP3 were treated with MG132 or Bafilomycin A1, and lysates were subjected to western blotting. S.E., short exposure; L.E., long exposure.
(D and E) The control and (D) ATG5 siRNA or (E) ATG7 siRNA-transfected HEK293T cells expressing NLRP3, GFP, or/and GFP-IRGM were subjected to immunoblotting.
(F and G) The control and the (F) ATG5 siRNA or (G) ATG7 siRNA-transfected THP-1 cells expressing GFP or GFP-IRGM were stimulated with LPS (1 μg/mL, 3 hr), and the cell lysates were subjected to immunoblotting.
(H) HEK293T cells expressing HA-ASC and GFP or GFP-IRGM were subjected to immunoblotting.
(I) The control and IRGM siRNA-transfected THP-1 cells lysates were subjected to immunoblotting.
(J) Western blotting analysis with lysates from HEK293T cells transfected with HA-ASC and GFP or GFP-IRGM, untreated or treated with BafA1 or MG132.
(K) CoIP analysis of interaction between FLAG-p62 and GFP-IRGM in HEK293T cell lysates.
(L and M) Representative confocal images of HEK293T cells expressing (L) GFP-p62 and mcherry-IRGM (M) HA-p62, mcherry-IRGM, and GFP-NLRP3.
(N) CoIP analysis of interaction between HA-p62 and GFP-NLRP3 in the absence and presence of FLAG-IRGM.
(O) Graph depicts the quantification of GFP-NLRP3 band intensity in IP (normalized compared to inputs) (n = 3, mean ± SD, *$p \leq 0.05$, Student's unpaired t test)
(P) CoIP analysis of interaction between p62 and ASC in the absence and presence of IRGM in HEK293T cell.
(Q) Analysis of degradation of NLRP3 in the absence and presence of IRGM and in HEK293T cells transfected with control siRNA and p62 siRNA.
(R) Representative confocal images of HEK293T cells expressing mcherry-IRGM, GFP-Beclin-1, and NLRP3.
(S) CoIP analysis of interaction between NLRP3 and Beclin-1 in the absence and presence of IRGM in HEK293T cells expressing the indicated plasmids.
*In order to reduce the artifact coming from IRGM-mediated degradation of NLRP3 and ASC, the inputs ratios were adjusted to have equal inputs in both the conditions, and the IP samples was run in the same ratios as of the inputs. Scale bars are as indicated in figures. S.E., short exposure; L.E., long exposure. See also Figures S2 and S3.

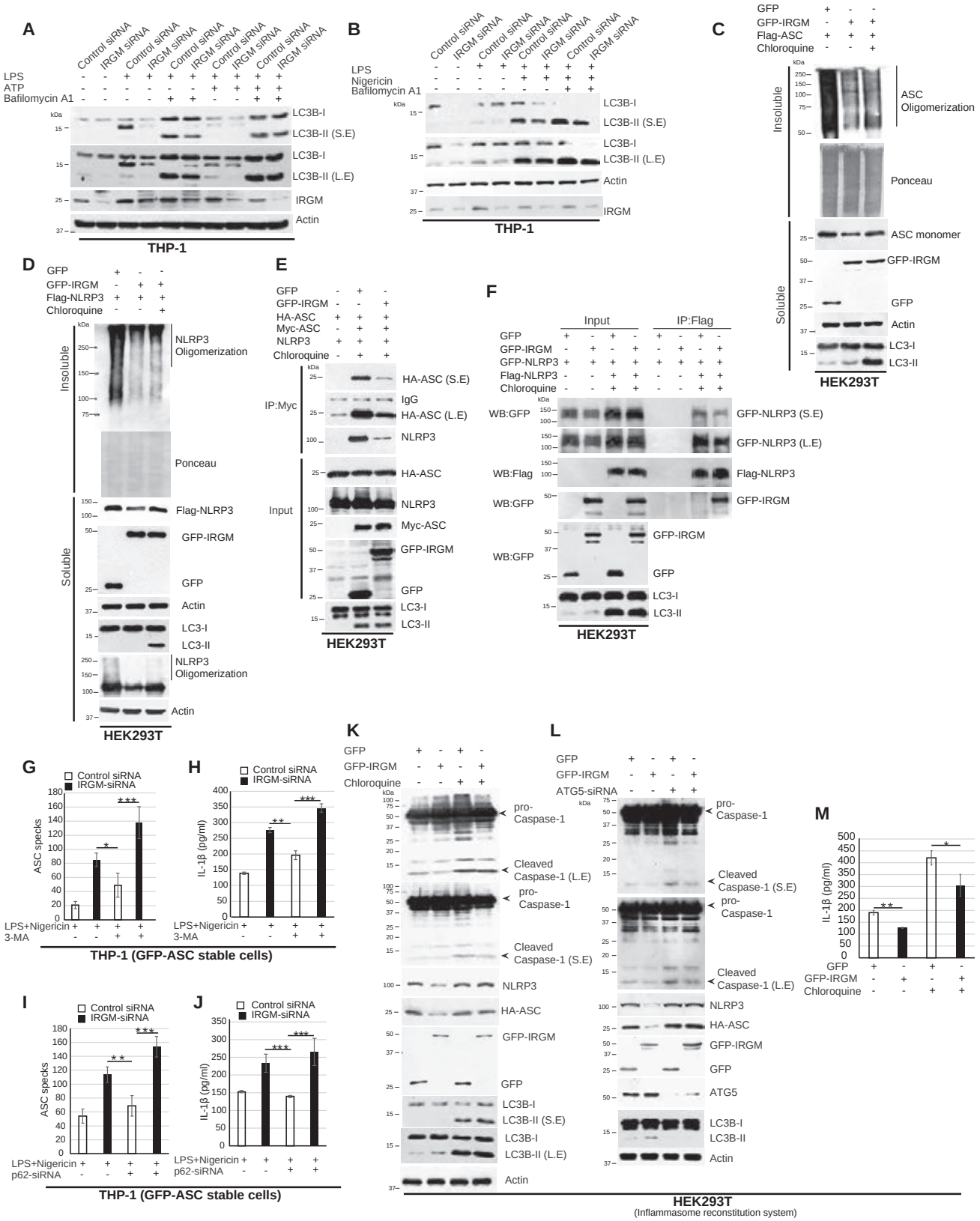

(legend on next page)

with Syntaxin 17, an autophagosome-lysosome fusion protein (Kumar et al., 2018). We found that this mutation (S47N, IRGM GTPase activity defective) in IRGM renders it inefficient in degrading NLRP3 suggesting the importance of IRGM GTPase activity in autophagy-mediated cargo degradation (Figure S5J). Very interestingly, this mutation was able to rescue the IRGM-mediated autophagic degradation of NLRP3 but not the oligomerization defect mediated by IRGM (Figure S5J). Taken together, the results suggest that IRGM controls two distinct mechanisms, autophagic degradation of NLRP3 (GTPase-dependent function) and inhibition of oligomerization of NLRP3 (GTPase-independent function).

Next, we performed several experiments to parse out the relative contribution of these two mechanisms in inhibiting NLRP3 inflammasome activation. We observed that the treatment of 3-MA (an autophagy inhibitor) results in increased inflammasomes (ASC specks) numbers and IL-1β secretion compared to the untreated THP-1 cells suggesting that autophagy reduces the NLRP3 inflammasome formation and activation (Figures 5G and 5H and S5K). We found that knockdown of IRGM induces significantly more ASC specks formation and also IL-1β secretion as compared to the 3-MA-treated THP-1 cells (Figures 5G and 5H). These data indicate that IRGM-mediated suppression of inflammasomes includes mechanisms more than autophagy-mediated degradation. The 3-MA-treated IRGM knockdown cells showed significantly higher ASC speck formation and IL-1β secretion than 3-MA-treated control cells (Figures 5G and 5H) suggesting that, in addition to autophagy-mediated suppression, the IRGM-mediated inhibition of oligomerization of inflammasomes may play a significant role in suppressing NLRP3 inflammasomes. Similar results were obtained when selective autophagic degradation of inflammasome was inhibited by knocking down of p62 in IRGM-depleted THP-1 cells (Figures 5I and 5J). Next, in HEK293T inflammasome reconstitution system, the overexpression of IRGM reduces caspase-1 cleavage (Figures 5K and 5L cf. lane 1 and 2 in SE) and also the IL-1β secretion (Figure 5M). The inhibition of autophagy (using chloroquine or ATG5 knockdown) in IRGM-overexpressing cells increased the caspase-1 cleavage and also IL-1β secretion but to lesser extent than autophagy-inhibited control cells (Figures 5K and 5L, cf. lane 4 with 3 in long exposure [L.E.], Figure 5M) suggesting yet again that IRGM mediates suppression of NLRP3 inflammasome by at least two distinct mechanisms discovered here.

IRGM Protects from Pyroptosis

Pyroptosis is an inflammatory cell death mediated by activation of inflammasomes (also called pyroptosomes) (Fernandes-Alnemri et al., 2007; Shi et al., 2017). Annexin V and propidium iodide (PI) double staining was used to access the role of IRGM in pyroptosis. Due to the formation of pores, pyroptotic cells are mainly stained by PI (PI is cell membrane impermeant). Annexin-V cannot distinguish between apoptotic cells and pyroptotic cells and stains both of them. In flow cytometry experiments, on exposure of inflammatory threats, both the apoptotic and pyroptotic populations were increased considerably in IRGM-depleted THP-1 cells compared to control cells (Figures 6A–6G, S6A, and S6B). These results suggest that IRGM protects the cells from inflammation-induced cell death. In the lactate dehydrogenase (LDH) release assays, there was a significant increase in the LDH amount in supernatant collected from LPS- and DAMP-treated IRGM-depleted THP-1 cells compared to the control cells (Figure S6C). Similar results were obtained using a trypan blue exclusion assay that accesses the integrity of the cell membrane during cell death (Figure S6D).

Recent studies identified Gasdermin D (GSDMD) as an effector protein for pyroptosis (Liu et al., 2016; Shi et al., 2015). In agreement with caspase-1 cleavage data presented in Figure 1, the cleavage of GSDMD was increased in IRGM-depleted cells compared to the control cells (Figure 6H). In agreement with flow cytometry data, apoptosis was also increased in IRGM knockdown cells compared to control cells as clear from the enhanced PARP1 (Poly [ADP-ribose] polymerase 1) cleavage (Figure 6I). Taken together, our data show that IRGM protects cells from inflammation-induced cell death.

Next, we blocked the caspase's activity using the pan-caspase inhibitor z-VAD-FMK or selective caspase-1 inhibitor Ac-YVAD-CMK to determine whether the inflammatory cell death observed in IRGM-depleted cells is caspase dependent or independent. The results (both by flow cytometry and western blotting) show that z-VAD-FMK and Ac-YVAD-CMK can block pyroptosis and also can reduce apoptosis induced by IRGM depletion (Figures 6J–6N) suggesting that IRGM suppresses caspase-1-dependent inflammatory cell death.

Mouse Irgm1 Suppresses the Gut Inflammation by Inhibiting the NLRP3 Inflammasome Activation

Although human IRGM and mouse Irgm1 possess biochemical differences, they have been found to have overlapping functions,

Figure 5. Both Autophagy and Inflammasome Assembly Defect Triggered by IRGM Leads to Inhibition of NLRP3 Inflammasome Activation

(A and B) Analysis of regulation of autophagy flux in control and IRGM knockdown THP-1 cells stimulated with LPS (1 μg/mL, 3 hr) or (A) LPS +ATP (5 mM, 60 min) or (B) LPS+nigericin (5 μM, 15 min) with or without Bafilomycin A1 (300 nM, 3 hr).

(C and D) Western blotting analysis of the DSS cross-linked insoluble and soluble fraction of HEK293T cells expressing (C) FLAG-ASC or (D) FLAG-NLRP3 and GFP or GFP-IRGM in absence or presence of chloroquine (50 μM, 5 hr).

(E and F) CoIP analysis of interaction between (E) myc-ASC and HA-ASC or (F) GFP-NLRP3 and FLAG-NLRP3 in the absence and presence of GFP-IRGM in HEK293T cells treated or untreated with chloroquine (50 μM, 5 hr).

(G–J) Average number of (G and I) ASC specks or (H and J) secreted IL-1 β from THP-1 GFP-ASC stable cells transfected with control and IRGM siRNA and stimulated with LPS+nigericin, in the absence and presence of (G and H) 3-MA (10 mM, 3 hr) or (I and J) p62 siRNA (n = 3, mean ± SD, *$p \leq 0.05$, **$p \leq 0.005$, ***$p \leq 0.0005$, Student's unpaired t test).

(K–M) HEK293T cells transfected with NLRP3, HA-ASC, caspase-1, pro-IL-1β, GFP-IRGM, and GFP for 30 hr and (K and M) treated with chloroquine for next 6 hr or (L) transfected with ATG5 siRNA. (K and L) The cell lysates were subjected to western blotting and (M) supernatant used in ELISA to measure IL-1β. (n = 3, mean ± SD, *$p \leq 0.05$, **$p \leq 0.005$, Student's unpaired t test).

S.E., short exposure; L.E., long exposure. See also Figures S4 and S5.

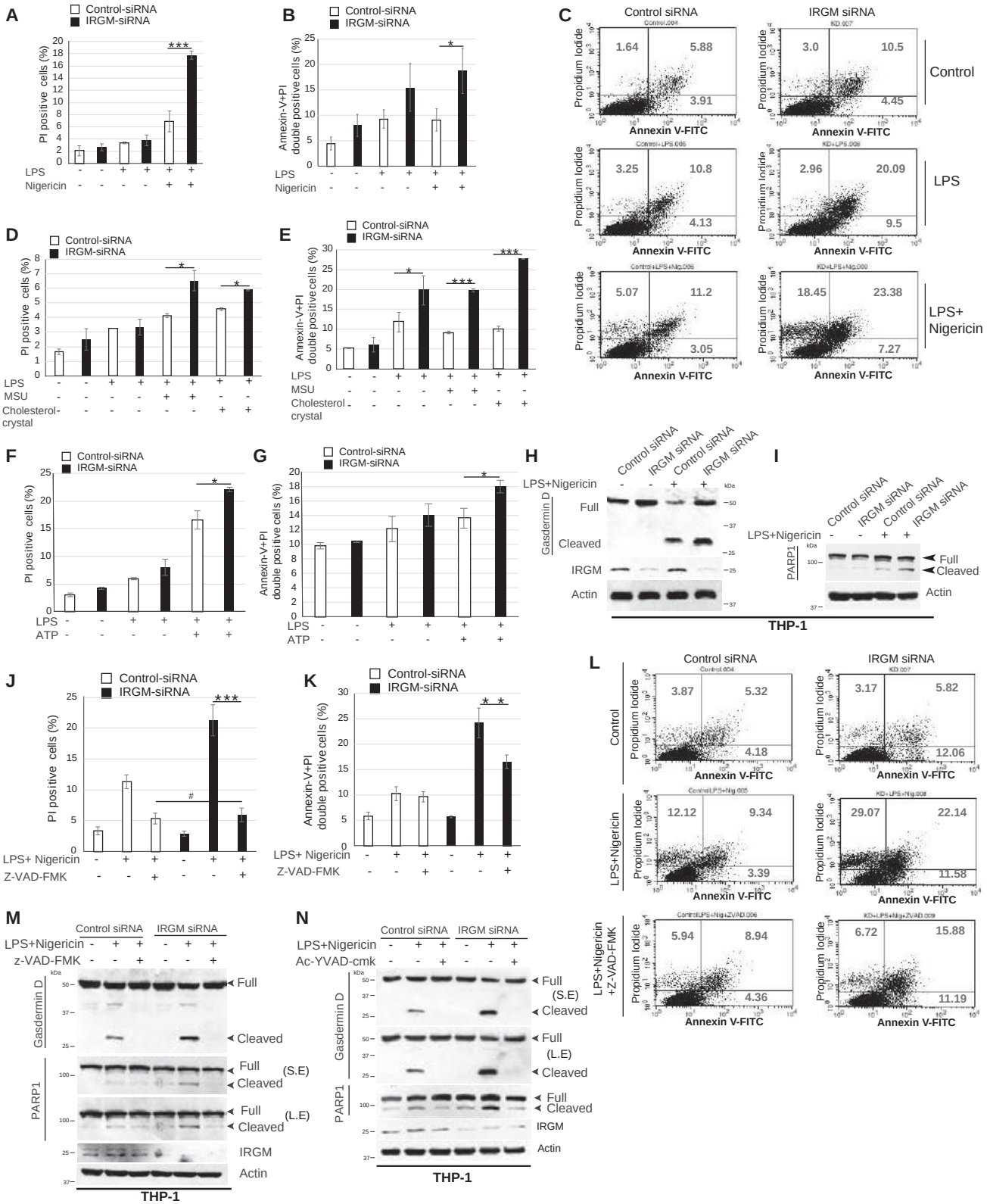

(legend on next page)

particularly as related to innate immunity and autophagy. Given the role of IRGM in inflammatory bowel disease (IBD) and Crohn's, we utilized the dextran-sulfate (DSS)-induced colitis model to investigate the role of Irgm1 in Nlrp3 inflammasome activation. *Irgm1*$^{-/-}$ mice have previously been shown to exhibit enhanced inflammation following DSS administration (Liu et al., 2013). Consistent with this report, we found here that the administration of DSS led to decreased body weight and colon length in *Irgm1*$^{-/-}$ mice relative to those responses in littermate *Irgm1*$^{+/+}$ mice (Figures S7A–S7D). Like in human colon cells, the expression of *IL-1β*, *TNF-α*, and *IL-18* was significantly increased in DSS-treated *Irgm1*$^{-/-}$ compared to *Irgm1*$^{+/+}$ mice (Figure 7A). Next, we scrutinized the expression of inflammasome components. In untreated mice, Nlrp3 expression was increased in *Irgm1*$^{-/-}$ mice compared to *Irgm1*$^{+/+}$ mice (Figure 7B); however, expression of ASC was not different (Figure 7B). In DSS-treated mice, the expression of both Nlrp3 and ASC in bone-marrow-derived macrophages and colon was more in *Irgm1*$^{-/-}$ mice compared to *Irgm1*$^{+/+}$ mice (Figures 7C and 7D). Also, ASC oligomerization was considerably higher in *Irgm1*$^{-/-}$ mice compared to *Irgm1*$^{+/+}$ mice (Figures 7C and 7D). In a cross-linking experiment with bone marrow-derived macrophages (BMDMs), both ASC and Nlrp3 oligomerization was found to be increased in *Irgm1*$^{-/-}$ mice compared *Irgm1*$^{+/+}$ mice (Figures 7E and S7E; STAR Methods). Under inflammasome-inducing conditions, the active caspase-1 amount was significantly higher in *Irgm1*$^{-/-}$ mice compared to control *Irgm1*$^{+/+}$ mice (Figure 7F). Similar to human cell lines studies, the basal autophagy and also the LPS-induced autophagy flux in BMDMs were dependent on the expression of Irgm1 (Figure 7G). Altogether, the data show that Irgm1, like its human ortholog, suppresses the activation of the NLRP3 inflammasome by inhibiting its assembly and by increasing autophagy.

Next, we analyzed whether increased Nlrp3 inflammasome activation is the cause for exacerbated outcomes of DSS-induced colitis in *Irgm1* knockout mice. MCC950 is the most potent and the most specific small-molecule inhibitor of activation of NLRP3 known to date (Coll et al., 2015; Strangward et al., 2018; Yao et al., 2018). We investigated whether selective pharmacologic blockade of the Nlrp3 inflammasome using MCC950 would reduce the colitis symptoms in *Irgm1*$^{-/-}$ mice. Indeed, we found that all the intensified outcomes of DSS-induced colitis in the Irgm1 knockout mice were reversed in the presence of MCC950 (Figures 7H–7J, S7F, and S7G). At molecular levels, in colon tissues, the increased amount of inflammasome components (Nlrp3, ASC monomers, and dimers) and also the enhanced inflammasome activity as measured by cleaved caspase-1 by western blot (Figure 7K) and fluorescent caspase-1 cleavage assay (Figure 7L) in *Irgm1*$^{-/-}$ mice were reversed by MCC950 treatment. Next, we isolated the BMDMs from these mice and induced the inflammasome (using LPS+ nigericin) in the absence and presence of MCC950. Again, the data show that inactivation of Nlrp3 by MCC950 considerably reduced the enhanced inflammasome activity in *Irgm1*$^{-/-}$ mice as measured by fluorescent caspase-1 cleavage assay (Figure 7M) and western blotting (Nlrp3, ASC dimer, and caspase-1 cleavage) (Figure 7N). Next, we used a genetic approach to determine whether enhanced inflammasome activation in Irgm1$^{-/-}$ mice BMDMs is because of increased activation of the Nlrp3/ASC inflammasome. In LPS+nigericin-stimulated BMDMs, the increased caspase-1 cleavage (Figures 7O and S7H) and the IL-1β secretion (Figures 7P and S7H) in *Irgm1*$^{-/-}$ mice BMDMs was blunted when Nlrp3 was depleted in these cells using siRNA.

Taken together, several lines of evidence suggest that NLRP3 activation is the primary factor behind enhanced inflammasome activity in IRGM-depleted cells, and also the activation of NLRP3 inflammasome is one of the major reasons for exacerbated outcomes of DSS-induced colitis in the *Irgm1* knockout mice. We conclude that the IRGM/Irgm1 suppresses the NLRP3 inflammasome to keep the gut inflammation under check.

DISCUSSION

In landmark genome-wide association studies conducted by Wellcome Trust Case Control Consortium to understand the genetic determinants of inflammatory diseases, SNPs in the *IRGM* locus were found to be strongly associated with Crohn's disease (Wellcome Trust Case Control, 2007; Craddock et al., 2010). Later, several studies showed similar genetic linkages of IRGM with Crohn's disease and other inflammatory and autoimmune diseases in different populations worldwide (Baskaran et al., 2014; Glas et al., 2013; Li et al., 2014; McCarroll et al., 2008; Xia et al., 2017; Yang et al., 2014). Most of these studies suggested a protective role of IRGM against the

Figure 6. IRGM Protects from Caspase-Dependent Inflammatory Cell Death

(A and B) Flow cytometry analysis of control and IRGM siRNA knockdown cells untreated or treated with LPS (1 μg/mL, 3 hr) and nigericin (5 μM, 30 min). Bar graphs show percentage of (A) PI positive or (B) Annexin V/PI double-positive cells.

(C) Representative dot plot showing flow cytometry analysis of control and IRGM siRNA knockdown cells untreated or treated with LPS and nigericin.

(D–G) Flow cytometry analysis of control and IRGM siRNA knockdown cells untreated or treated with LPS, MSU, cholesterol crystal, and ATP as indicated. Bar graph showing percentage of (D and F) PI positive and (E and G) Annexin V/PI double-positive cells.

(H and I) The control and IRGM siRNA-transfected THP-1 cells treated with LPS and nigericin were subjected to immunoblot analysis with (H) Gasdermin D or (I) PARP1 and actin antibodies.

(J and K) Flow cytometry analysis of control and IRGM siRNA knockdown cells untreated or treated with LPS, nigericin, and Z-VAD-FMK (5 μM, 30 min) as indicated. Bar graph showing the percentage of (J) PI positive and (K) Annexin V/PI double-positive cells.

(L) Representative dot plot is showing flow cytometry analysis of control and IRGM siRNA knockdown cells untreated or treated with LPS and nigericin and Z-VAD FMK as depicted.

(M and N) Western blot analysis of control and IRGM knockdown THP-1 cells untreated or treated with LPS, nigericin, and (M) Z-VAD-FMK or (N) Ac-YVAD-cmk. Unless otherwise stated, n = 3, mean ± SD, *p ≤ 0.05**p ≤ 0.005, ***p ≤ 0.0005, #insignificant, Student's unpaired t test). S.E., short exposure; L.E., long exposure. See also Figure S6.

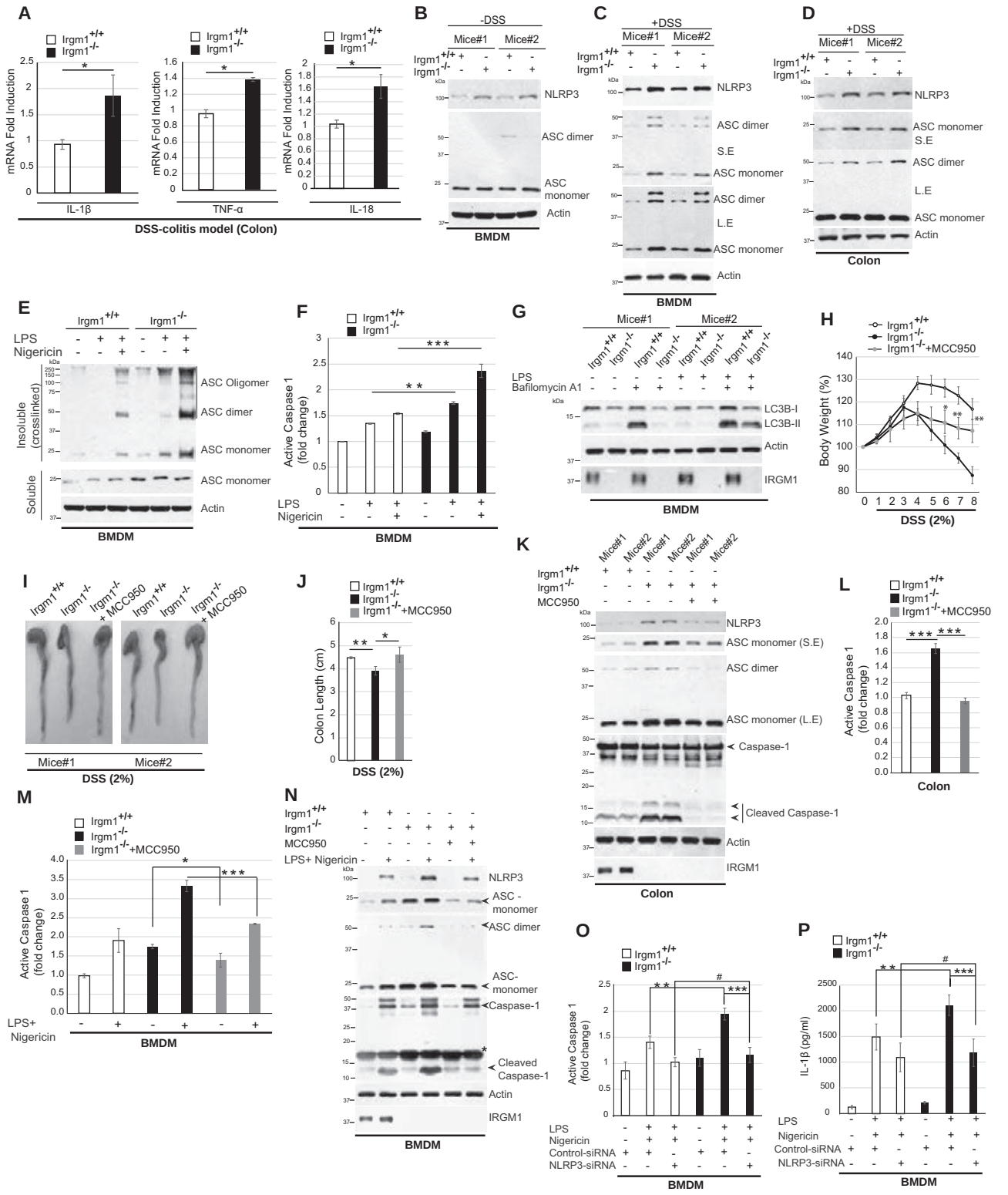

Figure 7. Irgm1 Suppresses Colitis via Inhibition of NLRP3 Inflammasome

(A) The qPCR analysis from the total RNA isolated from colon of DSS-treated *Irgm1*$^{+/+}$ and *Irgm1*$^{-/-}$ knockout mice (n = 3, mean ± SE, *p < 0.05, Student's unpaired t test).

(legend continued on next page)

inflammatory diseases; however, none of the studies revealed the mechanism(s).

This study defined the mechanism by which IRGM/Irgm1 regulates cellular inflammation in immune and gut epithelial cells (Figure S7I). We found here that IRGM suppresses IL-1β production by limiting the activation of the NLRP3 inflammasome (Figure S7I). Remarkably, IRGM performs this function by complexing directly with inflammasome components including NLRP3 and ASC. By binding to the oligomerization domain (NACHT) of NLRP3, it impedes the oligomerization of NLRP3. IRGM also hinders polymerization of ASC protein (Figure S7I), which is a key event for activation of inflammasome (Cai et al., 2014; Lu et al., 2014). Previous studies demonstrated the role of autophagy process in limiting the IL-1β production, and one of the mechanisms was by degrading the inflammasome and its components in a p62-dependent manner (Shi et al., 2012). Here, we found that IRGM is a key player in mediating p62-dependent selective autophagy of NLRP3 and ASC (Figure S7I). Thus, IRGM limits IL-1β production by two mechanisms: (1) by interfering in the assembly of the inflammasome and (2) by mediating autophagy of inflammasome. In the inflammatory bowel disease experimental mice model, Irgm1 suppresses the colitis by inhibiting the NLRP3 inflammasome. Taken together, this work revealed IRGM-mediated anti-inflammatory immune homeostasis mechanism by which IRGM could be protective against inflammatory diseases.

As compared to humans, where IRGM is a lone member of the IRG family, mice have 20 more homologs of Irgm1, presumably providing the compensation when the Irgm1 is knockout in the mice. Although human IRGM and mice Irgm1 are of different size (21 versus 47 kDa), they are strikingly similar in the regulation of autophagy and inflammation.

The dysregulated NLRP3 inflammasome has been linked to the pathogenesis of several inflammatory diseases including gout, type 2 diabetes, cancer, cardiovascular diseases, Alzheimer's, Parkinson's, and prion diseases (Alcocer-Gómez and Cordero, 2017; Lee et al., 2013; Song et al., 2017). Also, mutations in the NLRP3 gene have been linked with a range of dominantly inherited auto-inflammatory diseases (Masters et al., 2009). Therefore, it is of high importance to the medical science to understand the mechanisms by which the cell restrains the activation of NLRP3 inflammasome and IL-1β production. For similar reasons, understanding the protective nature of IRGM in human inflammatory diseases is crucial. This study delineates both. The therapeutic strategies to increase IRGM activity or targeting the IRGM-NLRP3 interaction could be useful for treating IRGM- and NLRP3-associated diseases.

STAR★METHODS

Detailed methods are provided in the online version of this paper and include the following:

- KEY RESOURCES TABLE
  - Cell Culture
  - Isolation of human peripheral blood mononuclear cells (PBMCs)
  - Plasmid Constructs and Transfection
  - Transient transfection with siRNA
  - Transient transfection with plasmids
  - Enzyme-linked immunosorbent assay (ELISA)
  - Bacterial Infections
  - ASC Oligomerization Assay
  - Western Blotting
  - Antibodies and dilution
  - Co-Immunoprecipitation
  - GST pull-down assay
  - Immunofluorescence Analysis
  - Cycloheximide chase assay
  - Macrophage differentiation and stimulation
  - Chloroform-methanol protein precipitation
  - Annexin-V/Propidium Iodide staining
  - Caspase-1 inhibition Assay
  - Soluble and Insoluble proteins fractionation
  - RNA Isolation and Quantitative Real-time PCR
  - Caspase 1 activity measurement assay
  - Mice experiments
  - Mice Bone marrow cells isolation and differentiation into macrophages
- DATA AND SOFTWARE ACCESSIBILITY

SUPPLEMENTAL INFORMATION

Supplemental Information includes seven figures and can be found with this article online at https://doi.org/10.1016/j.molcel.2018.11.018.

(B and C) Western blot analysis with BMDM lysates from (B) untreated or (C) DSS-treated *Irgm1*$^{+/+}$ and *Irgm1*$^{-/-}$ knockout mice with indicated antibodies.
(D) Western blot analysis with colon lysates from DSS-treated *Irgm1*$^{+/+}$ and *Irgm1*$^{-/-}$ mice.
(E) Western blotting analysis of cross-linked insoluble and soluble cell fraction from LPS- and nigericin-treated *Irgm1*$^{+/+}$ and *Irgm1*$^{-/-}$ BMDMs.
(F) The quantification of activated caspase-1 (FLICA assay) in LPS- and nigericin-treated *Irgm1*$^{+/+}$ and *Irgm1*$^{-/-}$ BMDM lysates.
(G) Western blotting analysis from LPS- and Bafilomycin A1-treated *Irgm1*$^{+/+}$ and *Irgm1*$^{-/-}$ BMDM cell lysates.
(H) Graph depicting the percentage of change in body weight during the course of DSS treatment.
(I) Representative pictures of colons of DSS- and MCC950-treated and -untreated *Irgm1*$^{+/+}$ and *Irgm1*$^{-/-}$ mice.
(J) Graph depicts colon length of DSS- and MCC950-treated and -untreated *Irgm1*$^{+/+}$ and *Irgm1*$^{-/-}$ mice.
(K) Western blot analysis from colon lysates of DSS- and MCC950-treated and -untreated *Irgm1*$^{+/+}$ and *Irgm1*$^{-/-}$ mice.
(L and M) The quantification of activated caspase-1 (FLICA assay) in (L) colon lysates of DSS and MCC950 or (M) BMDM lysates of LPS, nigericin, and MCC950 (1 μM)-treated and -untreated *Irgm1*$^{+/+}$ and *Irgm1*$^{-/-}$ mice.
(N) Western blot analysis from of LPS, nigericin, and MCC950 (1 μM)-treated or -untreated BMDM cell lysates from *Irgm1*$^{+/+}$ and *Irgm1*$^{-/-}$ mice. *Non-specific.
(O and P) Quantification of active caspase-1 (caspase-1 FLICA assay) (O) and secreted IL-1β (ELISA) (P) in LPS- (100 ng/mL, 3 hr) and nigericin- (5 μM, 15 min) treated NLRP3-depleted BMDMs from *Irgm1*$^{+/+}$ and *Irgm1*$^{-/-}$ mice.
S.E., short exposure; L.E., long exposure. n = 3, mean ± SD, *p < 0.05, **p < 0.005, ***p < 0.0005, #insignificant Student's t test unpaired). See also Figure S7.

ACKNOWLEDGMENTS

This work is funded by the Wellcome Trust/Department of Biotechnology (DBT) India Alliance (IA/I/15/2/502071) fellowship to Santosh Chauhan. Subhash Mehto, and Swati Chauhan are supported by a fellowship from SERB (NPDF, PDF/2016/001697) and DST (SR/WOS-A/LS-9/2016), respectively. We acknowledge the technical assistance of Kshitish Rout, Paritosh Nath (FACS facility), and Bhabani Sahoo (Microscopy facility). We gratefully acknowledge the reagents provided by Dr. Vojo Deretic (University of New Mexico, US) and Dr. Terje Johansen (The arctic university of Norway, Norway) during the course of study. We gratefully acknowledge the support of the Institute of Life Sciences central facilities funded by Department of Biotechnology (India).

AUTHOR CONTRIBUTIONS

Santosh Chauhan secured funding, conceived the project, designed experiments, and wrote the manuscript. S.M., K.K.J., P.N., Swati Chauhan, S.P.K., S.K.D., P.K.S., and A.J. carried out the experiments. G.A.T. provided critical inputs for experiments and edited the manuscript.

DECLARATION OF INTERESTS

The authors declare no competing interests.

Received: May 4, 2018
Revised: September 19, 2018
Accepted: November 15, 2018
Published: January 3, 2019

REFERENCES

Alcocer-Gómez, E., and Cordero, M.D. (2017). NLRP3 inflammasome: Common nexus between depression and cardiovascular diseases. Nat. Rev. Cardiol. *14*, 124.

Bafica, A., Feng, C.G., Santiago, H.C., Aliberti, J., Cheever, A., Thomas, K.E., Taylor, G.A., Vogel, S.N., and Sher, A. (2007). The IFN-inducible GTPase LRG47 (Irgm1) negatively regulates TLR4-triggered proinflammatory cytokine production and prevents endotoxemia. J. Immunol. *179*, 5514–5522.

Baskaran, K., Pugazhendhi, S., and Ramakrishna, B.S. (2014). Association of IRGM gene mutations with inflammatory bowel disease in the Indian population. PLoS ONE *9*, e106863.

Brest, P., Lapaquette, P., Souidi, M., Lebrigand, K., Cesaro, A., Vouret-Craviari, V., Mari, B., Barbry, P., Mosnier, J.F., Hébuterne, X., et al. (2011). A synonymous variant in IRGM alters a binding site for miR-196 and causes deregulation of IRGM-dependent xenophagy in Crohn's disease. Nat. Genet. *43*, 242–245.

Burada, F., Plantinga, T.S., Ioana, M., Rosentul, D., Angelescu, C., Joosten, L.A., Netea, M.G., and Saftoiu, A. (2012). IRGM gene polymorphisms and risk of gastric cancer. J. Dig. Dis. *13*, 360–365.

Cai, X., Chen, J., Xu, H., Liu, S., Jiang, Q.X., Halfmann, R., and Chen, Z.J. (2014). Prion-like polymerization underlies signal transduction in antiviral immune defense and inflammasome activation. Cell *156*, 1207–1222.

Chauhan, S., Mandell, M.A., and Deretic, V. (2015). IRGM governs the core autophagy machinery to conduct antimicrobial defense. Mol. Cell *58*, 507–521.

Chauhan, S., Kumar, S., Jain, A., Ponpuak, M., Mudd, M.H., Kimura, T., Choi, S.W., Peters, R., Mandell, M., Bruun, J., et al. (2016). TRIMs and Galectins Globally Cooperate and TRIM16 and Galectin-3 Co-direct Autophagy in Endomembrane Damage Homeostasis. Dev. Cell *39*, 13–27.

Che, N., Li, S., Gao, T., Zhang, Z., Han, Y., Zhang, X., Sun, Y., Liu, Y., Sun, Z., Zhang, J., et al. (2010). Identification of a novel IRGM promoter single nucleotide polymorphism associated with tuberculosis. Clin. Chim. Acta *411*, 1645–1649.

Chen, M., Meng, Q., Qin, Y., Liang, P., Tan, P., He, L., Zhou, Y., Chen, Y., Huang, J., Wang, R.F., and Cui, J. (2016). TRIM14 inhibits cGAS degradation mediated by selective autophagy receptor p62 to promote innate immune responses. Mol. Cell *64*, 105–119.

Choi, A.J., and Ryter, S.W. (2014). Inflammasomes: Molecular regulation and implications for metabolic and cognitive diseases. Mol. Cells *37*, 441–448.

Coll, R.C., Robertson, A.A., Chae, J.J., Higgins, S.C., Muñoz-Planillo, R., Inserra, M.C., Vetter, I., Dungan, L.S., Monks, B.G., Stutz, A., et al. (2015). A small-molecule inhibitor of the NLRP3 inflammasome for the treatment of inflammatory diseases. Nat. Med. *21*, 248–255.

Craddock, N., Hurles, M.E., Cardin, N., Pearson, R.D., Plagnol, V., Robson, S., Vukcevic, D., Barnes, C., Conrad, D.F., Giannoulatou, E., et al.; Wellcome Trust Case Control Consortium (2010). Genome-wide association study of CNVs in 16,000 cases of eight common diseases and 3,000 shared controls. Nature *464*, 713–720.

Deretic, V., and Klionsky, D.J. (2018). Autophagy and inflammation: A special review issue. Autophagy *14*, 179–180.

Deretic, V., Saitoh, T., and Akira, S. (2013). Autophagy in infection, inflammation and immunity. Nat. Rev. Immunol. *13*, 722–737.

Duncan, J.A., Bergstralh, D.T., Wang, Y., Willingham, S.B., Ye, Z., Zimmermann, A.G., and Ting, J.P. (2007). Cryopyrin/NALP3 binds ATP/dATP, is an ATPase, and requires ATP binding to mediate inflammatory signaling. Proc. Natl. Acad. Sci. USA *104*, 8041–8046.

Fernandes-Alnemri, T., Wu, J., Yu, J.W., Datta, P., Miller, B., Jankowski, W., Rosenberg, S., Zhang, J., and Alnemri, E.S. (2007). The pyroptosome: A supramolecular assembly of ASC dimers mediating inflammatory cell death via caspase-1 activation. Cell Death Differ. *14*, 1590–1604.

Glas, J., Seiderer, J., Bues, S., Stallhofer, J., Fries, C., Olszak, T., Tsekeri, E., Wetzke, M., Beigel, F., Steib, C., et al. (2013). IRGM variants and susceptibility to inflammatory bowel disease in the German population. PLoS ONE *8*, e54338.

Guo, H., Callaway, J.B., and Ting, J.P. (2015). Inflammasomes: Mechanism of action, role in disease, and therapeutics. Nat. Med. *21*, 677–687.

Henry, S.C., Daniell, X., Indaram, M., Whitesides, J.F., Sempowski, G.D., Howell, D., Oliver, T., and Taylor, G.A. (2007). Impaired macrophage function underscores susceptibility to Salmonella in mice lacking Irgm1 (LRG-47). J. Immunol. *179*, 6963–6972.

Hunn, J.P., Feng, C.G., Sher, A., and Howard, J.C. (2011). The immunity-related GTPases in mammals: A fast-evolving cell-autonomous resistance system against intracellular pathogens. Mamm. Genome *22*, 43–54.

Jo, E.K., Kim, J.K., Shin, D.M., and Sasakawa, C. (2016). Molecular mechanisms regulating NLRP3 inflammasome activation. Cell. Mol. Immunol. *13*, 148–159.

Kimura, T., Jain, A., Choi, S.W., Mandell, M.A., Schroder, K., Johansen, T., and Deretic, V. (2015). TRIM-mediated precision autophagy targets cytoplasmic regulators of innate immunity. J. Cell Biol. *210*, 973–989.

Kumar, S., Jain, A., Farzam, F., Jia, J., Gu, Y., Choi, S.W., Mudd, M.H., Claude-Taupin, A., Wester, M.J., Lidke, K.A., et al. (2018). Mechanism of Stx17 recruitment to autophagosomes via IRGM and mammalian Atg8 proteins. J. Cell Biol. *217*, 997–1013.

Lamkanfi, M., and Dixit, V.M. (2012). Inflammasomes and their roles in health and disease. Annu. Rev. Cell Dev. Biol. *28*, 137–161.

Lee, H.M., Kim, J.J., Kim, H.J., Shong, M., Ku, B.J., and Jo, E.K. (2013). Upregulated NLRP3 inflammasome activation in patients with type 2 diabetes. Diabetes *62*, 194–204.

Li, Y., Feng, S.T., Yao, Y., Yang, L., Xing, Y., Wang, Y., and You, J.H. (2014). Correlation between IRGM genetic polymorphisms and Crohn's disease risk: A meta-analysis of case-control studies. Genet. Mol. Res. *13*, 10741–10753.

Liu, B., Gulati, A.S., Cantillana, V., Henry, S.C., Schmidt, E.A., Daniell, X., Grossniklaus, E., Schoenborn, A.A., Sartor, R.B., and Taylor, G.A. (2013). Irgm1-deficient mice exhibit Paneth cell abnormalities and increased susceptibility to acute intestinal inflammation. Am. J. Physiol. Gastrointest. Liver Physiol. *305*, G573–G584.

Article

SOURCE DATA | TRANSPARENT PROCESS | OPEN ACCESS

THE EMBO JOURNAL

Selective autophagy of RIPosomes maintains innate immune homeostasis during bacterial infection

Subhash Mehto[1,*,†], Kautilya Kumar Jena[1,†,‡], Rina Yadav[1,2], Swatismita Priyadarsini[3], Pallavi Samal[1], Sivaram Krishna[1,2], Kollori Dhar[1,2], Ashish Jain[4,5], Nishant Ranjan Chauhan[1], Krushna C Murmu[6], Ramyasingh Bal[1,7], Rinku Sahu[1,2], Pundrik Jaiswal[1], Bhabani Sankar Sahoo[3], Srinivas Patnaik[7], Thomas A Kufer[8], Tor Erik Rusten[4,5], Swati Chauhan[6], Punit Prasad[6] & Santosh Chauhan[1,9,**]

Abstract

The NOD1/2-RIPK2 is a key cytosolic signaling complex that activates NF-κB pro-inflammatory response against invading pathogens. However, uncontrolled NF-κB signaling can cause tissue damage leading to chronic diseases. The mechanisms by which the NODs-RIPK2-NF-κB innate immune axis is activated and resolved remain poorly understood. Here, we demonstrate that bacterial infection induces the formation of endogenous RIPK2 oligomers (RIPosomes) that are self-assembling entities that coat the bacteria to induce NF-κB response. Next, we show that autophagy proteins IRGM and p62/SQSTM1 physically interact with NOD1/2, RIPK2 and RIPosomes to promote their selective autophagy and limit NF-κB activation. IRGM suppresses RIPK2-dependent pro-inflammatory programs induced by *Shigella* and *Salmonella*. Consistently, the therapeutic inhibition of RIPK2 ameliorates *Shigella* infection- and DSS-induced gut inflammation in Irgm1 KO mice. This study identifies a unique mechanism where the innate immune proteins and autophagy machinery are recruited together to the bacteria for defense as well as for maintaining immune homeostasis.

Keywords autophagy; inflammation; Irgm1; NOD1/2-RIPK2-NF-κB; RIPosomes

Subject Categories Autophagy & Cell Death; Microbiology, Virology & Host Pathogen Interaction

DOI 10.15252/embj.2022111289 | Received 28 March 2022 | Revised 12 September 2022 | Accepted 15 September 2022 | Published online 11 October 2022

The EMBO Journal (2022) 41: e111289

Introduction

NOD1 and NOD2 (NODs) are cytosolic pattern recognition receptors (PRRs) that detect pathogen-associated molecular patterns (PAMPs), iE-DAP (D-glutamyl-meso-diaminopimelic acid), and MDP (muramyl dipeptide; Tanabe *et al*, 2004; Laroui *et al*, 2011; Caruso *et al*, 2014). Stimulated NODs interact and activate adaptor protein RIPK2 (RICK, RIP2) for a cascade of events resulting in NF-κB activation and pro-inflammatory cytokine release (Girardin *et al*, 2001; Caruso *et al*, 2014). NODs-RIPK2 is one of the major innate immune axis that senses intracellular bacterial pathogens and mounts a powerful NF-κB-dependent pro-inflammatory cytokine response to eliminate bacteria.

An important step for triggering pro-inflammatory innate immune pathways is the oligomerization of PRRs and/or adaptor proteins (Hou *et al*, 2011; Xie *et al*, 2013; Xu *et al*, 2014; Wu & Fuxreiter, 2016). For example, activation of RIG-I signaling induces polymerization of MAVS to form detergent-resistant, protease-resistant, and self-perpetuating prion-like aggregates (filamentous structure) to activate and transmit antiviral signaling (Hou *et al*, 2011; Cai *et al*, 2014; Wu *et al*, 2014; Xu *et al*, 2014). The inflammasome is another classical example, where several self-polymerized inflammatory proteins interact with each other to form multiprotein signalosomes that execute pro-inflammatory responses (Cai *et al*, 2014; Lu *et al*, 2014, 2016). Recently, structural studies demonstrated that purified RIPK2 polymerizes to form filamentous structures that are important for NODs-dependent NF-κB signaling (Gong *et al*, 2018; Pellegrini *et al*, 2018). Also, ectopically

1 Cell Biology and Infectious Diseases Unit, Department of Infectious Disease Biology, Institute of Life Sciences, Bhubaneswar, India
2 Regional Centre for Biotechnology, NCR Biotech Science Cluster, Faridabad, India
3 Institute of Life Sciences, Bhubaneswar, India
4 Centre for Cancer Cell Reprogramming, Institute of Clinical Medicine, Faculty of Medicine, University of Oslo, Oslo, Norway
5 Department of Molecular Cell Biology, Institute for Cancer Research, Oslo University Hospital, Oslo, Norway
6 Epigenetic and Chromatin Biology Unit, Institute of Life Sciences, Bhubaneswar, India
7 School of Biotechnology, KIIT University, Bhubaneswar, India
8 Department of Immunology, Institute of Nutritional Medicine, University of Hohenheim, Stuttgart, Germany
9 CSIR–Centre For Cellular And Molecular Biology (CCMB), Hyderabad, India
*Corresponding author. Tel: +91 7503157368; E-mail: subhash@ils.res.in
**Corresponding author. Tel: +91 7077702598; E-mail: schauhan@ils.res.in; schauhan@ccmb.res.in
†These authors contributed equally to this work
‡Present address: Division of Immunology, Boston Children's Hospital, Harvard Medical School, Boston, MA, USA

expressed RIPK2 was shown to form detergent-insoluble higher-order oligomeric structures upon *Shigella* infection (Ellwanger *et al*, 2019). These structures were termed "RIPosomes." To date, it is not clear whether endogenous RIPK2 forms RIPosomes and if yes, how they regulate NF-κB signaling upon bacterial infection.

The NODs-RIPK2-NF-κB pro-inflammatory axis is critical for clearing pathogens; however, its aberrant activation can cause chronic inflammation, oncogenesis, and autoimmune disease (Miceli-Richard *et al*, 2001; Kanazawa *et al*, 2005; Henckaerts & Vermeire, 2007; Caso *et al*, 2015; Taniguchi & Karin, 2018). To avoid these conditions, a balanced immune state needs to be maintained by negative feedback mechanisms. Inflammophagy, the autophagic degradation of inflammatory aggregates and proteins, is an emerging mechanism to limit inflammation to maintain innate immune homeostasis (Chauhan *et al*, 2021; Deretic, 2021). Several of the cytosolic PRRs and adaptor proteins including RIG-I, NLRP3, AIM2, cGAS, MAVS, and STING are targeted by p62- or NDP52-dependent selective autophagy to dampen the excess inflammation (Shi *et al*, 2012; Liu *et al*, 2016; Du *et al*, 2018; Prabakaran *et al*, 2018; He *et al*, 2019; Mehto *et al*, 2019b; Jena *et al*, 2020; Chauhan *et al*, 2021; Deretic, 2021). To date, it is unclear how selective autophagy contributes to fine-tuning of the NODs-RIPK2-NF-κB pathways.

Genetic mutations in the Immunity-related GTPase M (IRGM) gene or promoter are suggested to increase susceptibility to several inflammatory and infectious diseases including Crohn's disease, tuberculosis, sepsis, and ankylosing spondylitis (Massey & Parkes, 2007; Parkes *et al*, 2007; Intemann *et al*, 2009; Lu *et al*, 2013; Kimura *et al*, 2014; Lin *et al*, 2016; Xia *et al*, 2017; Yao *et al*, 2018). IRGM is also a critical factor for antimicrobial autophagy (Singh *et al*, 2006; Chauhan *et al*, 2015). IRGM interacts with autophagy and lysosome regulatory proteins to stimulate autophagosome/lysosome biogenesis for efficient degradation of cargo including microbes (Singh *et al*, 2010; Chauhan *et al*, 2015; Kumar *et al*, 2018, 2020). IRGM plays a prominent role in the inflammophagy of several innate immune sensing proteins including NLRP3, RIG-I, and cGAS to limit inflammasome and interferon responses (Mehto *et al*, 2019a, 2019b; Jena *et al*, 2020; Chauhan *et al*, 2021; Nath *et al*, 2021). IRGM interacts with NOD2 to scaffold the signaling events for xenophagy (Chauhan *et al*, 2015); however, it is unclear whether IRGM also could regulate the activity of NODs and RIPK2 (RIPosomes) to control NF-κB pro-inflammatory cytokine response.

Here, we demonstrate that pathogenic bacteria induce the formation of endogenous RIPosomes in the proximity of the bacteria to activate the NF-κB cytokine response. Further, we found that NODs, RIPK2, and RIPosomes are targets of selective autophagy. The autophagy scaffolding proteins, IRGM and p62 physically interact with NODs, RIPK2, and RIPosomes, and using the canonical autophagy machinery coordinate their selective degradation to limit cytokine responses. In agreement, the global transcriptomic analysis revealed that during *Salmonella* and *Shigella* infection, IRGM suppresses multiple RIPK2-dependent pro-inflammatory pathways including NF-κB and interferon (IFN) response. Consistently, in animal studies, inhibition of RIPK2 using GSK583 ameliorated shigellosis- and dextran sodium sulfate (DSS)-induced gut inflammation, and pathology in *Irgm1*^{KO} mice. Together, this study delineates new cell-autonomous mechanisms of NODs-RIPK2-dependent pro-inflammatory response and its resolution by selective autophagy. Further, our study also suggests that inhibition of RIPK2 could be a good therapeutic strategy for suppression of gut inflammation associated with IRGM depletion, a risk factor in the progression of Crohn's disease.

Results

RIPosomes recruit over the bacteria

The existence of endogenous RIPK2 oligomeric structures (RIPosomes) is not reported. We found that infection of macrophage-like differentiated THP-1 cells with *Shigella flexneri* induces RIPosome formation. RIPosomes were detected only in infected cells but not in control cells (Appendix Fig S1A). Several of the RIPosomes were recruited over the bacteria (Fig 1A and Appendix Fig S1A–C and Movie EV1). However, not all the intracellular bacteria were covered with oligomeric RIPK2 puncta (Fig 1A). High-content microscopy was performed to quantitate the RIPosomes present in the cell (Fig 1B and Appendix Fig S1D). The presence of endogenous RIPK2 oligomeric structures was further confirmed by Western blotting of detergent-insoluble fractions from *Shigella*-infected cells (Fig 1C). To confirm specificity, next we depleted RIPK2 and tested the formation of RIPosomes by high-content microscopy and Western blotting. *Shigella*-induced RIPosomes were dramatically reduced upon RIPK2 siRNA knockdown in THP-1 macrophages (Fig 1D and E) or RIPK2 CRISPR knockout HT-29 cells (henceforth, RIPK2$^{-/-}$; Fig 1F).

Next, we infected mouse bone marrow-derived macrophages (BMDMs), HT-29 colon epithelial cells, and mouse embryonic fibroblast (MEF) cells with *Shigella*. RIPosomes were recruited over and adjacent to the bacteria in the infected cells (Fig 1G and Appendix Fig S1E–G), whereas the uninfected cells were devoid of them (Appendix Fig S1F). Thus, *Shigella* infection can induce RIPosome formation in different cell types. Next, C57BL/6 mice were infected by the intraperitoneal injection of *Shigella* (Yang *et al*, 2014), and immunohistochemistry with the colon tissues was performed. Several of the bacteria were covered with RIPosomes in colon tissues (Fig 1H).

To test whether RIPosome formation is specific to *Shigella* infection or is a generalized event during bacterial infection, we infected THP-1 cells with *Salmonella typhimurium*. Like *Shigella*, *Salmonella* enhanced the oligomerization of RIPK2 (Appendix Fig S1H) and triggered RIPosome formation (Fig 1I and J). Furthermore, infection with the Crohn's disease-associated adherent invasive *Escherichia coli* (AIEC) strain LF82 (Glasser *et al*, 2001) also prompted the formation of RIPosomes that were coating the bacteria (Fig 1K). Next, we compared RIPosome inducing capacity of pathogenic *Mycobacterium tuberculosis* (*M.tb*, H37Rv) and nonpathogenic *Mycobacterium smegmatis* (*M. smeg*, MC^{2}155). Surprisingly, only *M.tb* triggered the massive formation of RIPosomes over the bacteria (Fig 1L and M and Appendix Fig S1I and Movie EV2), indicating that only pathogenic bacteria could activate RIPosome formation. To further corroborate this notion, we compared the RIPK2 oligomerization capacity of nonpathogenic *E. coli* DH5α and pathogenic AIEC LF82. Indeed, LF82 was more efficient in triggering the oligomerization of RIPK2 (Fig 1N).

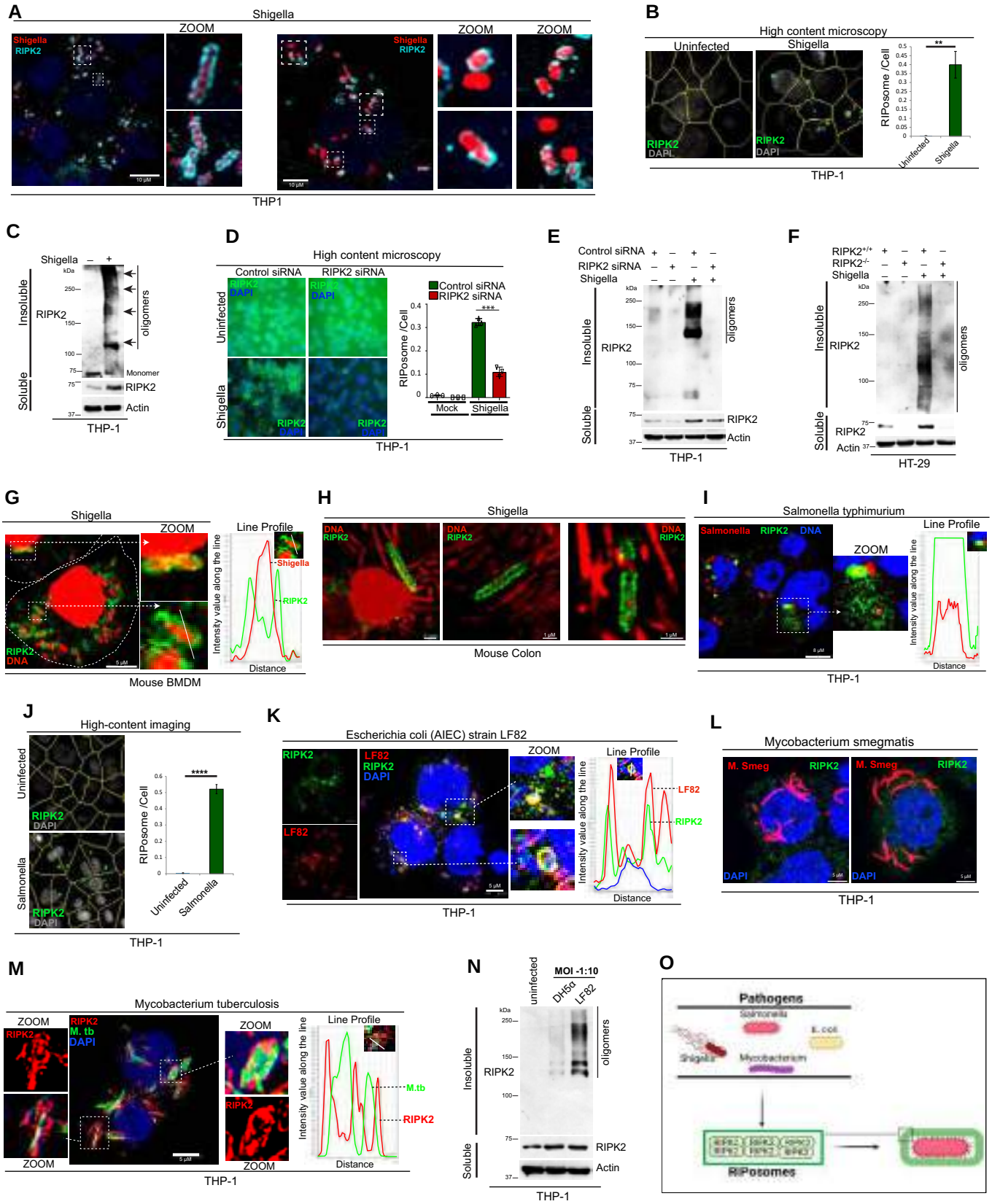

Figure 1.

Figure 1. Pathogenic bacteria trigger the formation of RIPosomes that recruit over the bacteria.

A Representative confocal images of RIPosomes in THP-1 cells infected with a red fluorescent protein (RFP) expressing *Shigella flexneri* (MOI 1:25, 8 h). Scale bar, 10 μm. Zoom panels are digital magnifications.

B Representative high-content microscopy images (see Appendix Fig S1D for full images; yellow masks represent software algorithms-defined cell boundaries) of RIPosomes in THP-1 cells infected with *S. flexneri* (MOI 1:25, 8 h). About 50,000 cells were plated per well and RIPosomes were screened in 35 fields per well in three technical replicates. Right panel, the graph depicts an average number of RIPosomes/cell, which is calculated from three biological replicates, Mean ± SD. ***$P < 0.005$, Student's unpaired *t*-test.

C Western blot analysis of soluble and insoluble fractions of *S. flexneri*-infected THP-1 cells (MOI 1:25, 8 h). Arrow indicates oligomers of RIPK2.

D Left panel, representative high-content microscopy image of control and RIPK2 knockdown THP-1 cells infected with *S. flexneri* (MOI 1:25, 8 h). Right panel, the graph depicts an average number of RIPosomes/cell, which is calculated from three biological replicates, Mean ± SD. ***$P < 0.0005$, Student's unpaired *t*-test.

E, F Western blot analysis of soluble and insoluble fractions of *S. flexneri*-infected (E) control siRNA and RIPK2 siRNA transfected THP-1 cells (F) Control CRISPR ($RIPK2^{+/+}$) cells and RIPK2 CRISPR knockout ($RIPK2^{-/-}$) HT-29 cells.

G Representative confocal images of RIPosomes in mouse BMDMs infected with *S. flexneri* (MOI 1:25, 8 h). Line profile: co-localization analysis using line intensity profile. Scale bar, 5 μm. Zoom panels are digital magnifications. DNA is stained with DAPI (pseudo-colored red for better contrast).

H Representative confocal images of mouse colon tissues showing recruitment of RIPK2 over the *S. flexneri*. Scale bar, 1 μm. Zoom panels are super-resolution confocal images. DNA is stained with DAPI (pseudo-colored red for better contrast).

I Representative confocal images of RIPosomes in THP-1 cells infected with RFP expressing *Salmonella typhimurium* (MOI 1:5, 4 h). Line profile: co-localization analysis using line intensity profile. Scale bar, 8 μm. Zoom panels are digital magnifications. DNA is stained with DAPI.

J Left panel, representative high-content microscopy images (yellow masks represent software algorithms-defined cell boundaries) of RIPosomes in THP-1 cells infected with *S. typhimurium* (MOI 1:5, 4 h). The same cell numbers and conditions are used as indicated in (B). Right panel, the graph depicts an average number of RIPosomes/cell. Mean ± SD, $n = 4$ (biological replicates), ****$P < 0.00005$, Student's unpaired *t*-test. DNA is stained with DAPI.

K–M Representative confocal images of RIPosomes in THP-1 cells infected with (K) *E. coli* LF82 strain (MOI 1: 10, 8 h), (LPS antibody is used to stain LF82) (L) mCherry expressing *M. smegmatis* (MOI 1:10, 4 h) (M) mCherry (pseudocolored to green) expressing *M. tuberculosis* (MOI 1:10, 8 h). Line profile: co-localization analysis using line intensity profiles. Scale bar, 5 μm. Zoom panels are digital magnifications. DNA is stained with DAPI.

N Western blot analysis of soluble and insoluble fractions from THP-1 cells, uninfected or infected with *E. coli* DH5α (MOI 1:10, 8 h) or *E. coli* LF82 strains (MOI 1:10, 8 h).

O Pictorial representation of data obtained in this figure shows that bacterial infection triggers oligomerization of RIPK2 or RIPosome formation that coats bacteria.

Source data are available online for this figure.

No RIPosomes were formed upon infection with GFP-tagged vesicular stomatitis virus (Appendix Fig S1J). Similarly, the NOD1 and NOD2 ligands, iE-DAP or MDP were not able to trigger visible RIPosome formation (Appendix Fig S1K). However, iE-DAP or MDP increased oligomerization of RIPK2 in the insoluble fraction of cells (Appendix Fig S1L and M), suggesting that they have a reduced capacity to induce RIPK2 oligomerization.

Altogether, these findings demonstrate that bacterial infection triggers RIPosome formation that is recruited at cytoinvasive bacteria both *in vitro* and *in vivo* conditions (Fig 1O).

RIPosomes are self-assembling structures that promote NODs oligomerization

RIPK2 is a common adaptor protein for NOD1 or NOD2-dependent NF-κB signaling. Several inflammatory proteins utilize their CARD domain to self-oligomerize and/or to hetero-oligomerize with downstream cognate signaling adaptor proteins for activation and signal transduction (Park, 2019). All three proteins, NOD1, NOD2, and RIPK2 possess CARD domain/s (Fig 2A); however, only RIPK2 self-oligomerized and formed RIPosomes (Fig 2A and B and Appendix Fig S2A) and fractionated in the insoluble (pellet) portion of cells (Appendix Fig S2B and C). Further, the CARD domain of RIPK2 ($RIPK2^{CARD}$) formed high-order oligomers (Fig 2C) and large filamentous structures (Fig 2D and Movie EV3), whereas the CARD domain of $NOD1^{CARD}$ and $NOD2^{CARDs}$ domain failed to do so (Fig 2C and D). These results suggest that only RIPK2 (but not NODs) can self-oligomerize using its CARD domain.

Interestingly, upon *Shigella* infection, endogenous NOD2 formed puncta (Appendix Fig S2D) and the oligomeric aggregates of both NOD1 and NOD2 were increased in the insoluble cell fractions (Fig 2E). NOD2 puncta were found to be juxtaposed to the bacteria (Appendix Fig S2D) where they co-localized/juxtaposed with RIPosomes (Fig 2F and Appendix Fig S2E). This apparent discrepancy between overexpressed and endogenous results could be due to the presence of endogenous RIPK2 in THP-1 cells (compared with HEK293T) whose self-assembly may have prompted co-oligomerization of NOD1/2 leading to puncta formation. Indeed, both the NOD1 and NOD2 formed insoluble oligomeric structures when co-expressed with RIPK2, as apparent from immunofluorescence (Fig 2G and Appendix Fig S2F), quantitative high-content microscopy (Appendix Fig S2G), and soluble/insoluble fractionation assays (Fig 2H). NODs were perfectly co-localized with RIPK2 in these structures (Fig 2G and Appendix Fig S2F and G). We termed these structures NODo-RIPosomes. These data were further supported by experiments where we found $NOD1^{CARD}$ or $NOD2^{CARDs}$ domain/s start oligomerizing once they are co-expressed with the $RIPK2^{CARD}$ (Fig 2I). Also, the $NOD1^{CARD}$ or $NOD2^{CARD}$ formed the punctate structures when co-expressed with $RIPK2^{CARD}$ (Appendix Fig S2H and I). Taken together, the data suggest that RIPK2 facilitates the oligomerization of NOD proteins via CARD domain/s. This notion was further tested in endogenous conditions by assessing the oligomerization of NOD proteins in the absence of RIPK2. *Shigella*-induced oligomerization of endogenous NODs was reduced in $RIPK2^{-/-}$ HT-29 cells compared with WT (Fig 2J and K). Thus, we conclude that RIPK2 self-assembling property is critical for inducing oligomerization of NOD1 and NOD2. Conversely, we noticed that the NOD proteins, in turn, enhanced the self-oligomerization capacity of RIPK2 (Appendix Fig S2J and K).

The formation of RIPosomes is important for the activation of NF-κB signaling (Gong *et al*, 2018; Pellegrini *et al*, 2018). We used a HeLa cell line expressing stable doxycycline-inducible human GFP-RIPK2 (Ellwanger *et al*, 2019) to evaluate whether *Shigella* infection-induced RIPosomes prompt nuclear translocation of NF-

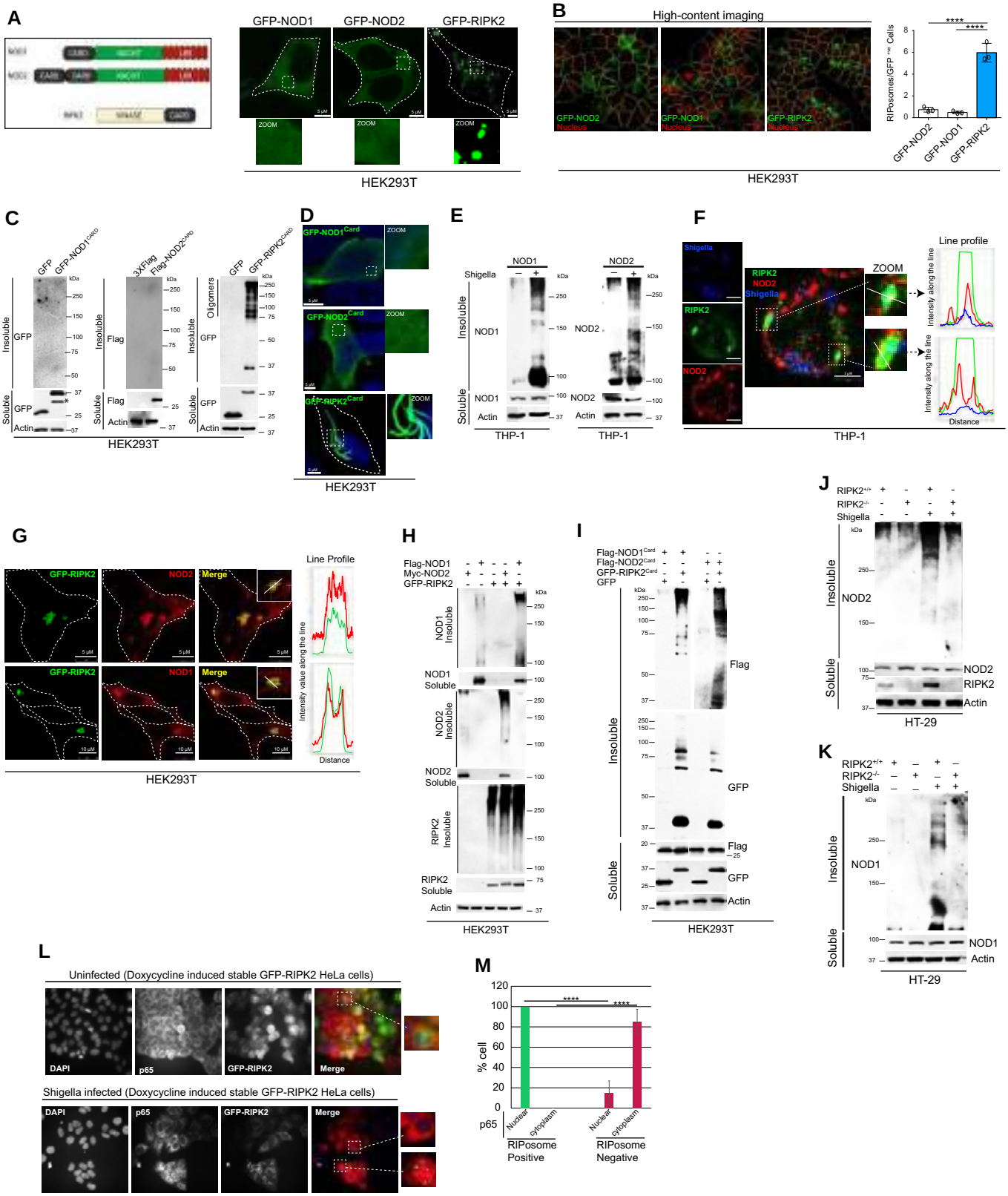

Figure 2.

Figure 2. RIPK2 oligomers provide a platform for NODs oligomerization.

A Left panel, the domain organization map of NOD1, NOD2, and RIPK2. Right panel, representative confocal images of immunofluorescence assays performed in HEK293T cells transfected with GFP-NOD1, GFP-NOD2, and GFP-RIPK2 plasmids for 9 h. Scale bar 5 μm.

B Left panel, representative high-content microscopy images of HEK293T cells transfected with GFP-NOD1, GFP-NOD2, and GFP-RIPK2 plasmids for 9 h. Right panel, the graph depicts the average number of RIPosomes per GFP-positive cell. About 15,000 cells were plated per well and RIPosomes were screened in 35 fields per well. Mean ± SD, $n = 3$ (biological replicates), $^{****}P < 0.00005$, ordinary one-way ANOVA (Tukey's multiple comparisons test).

C Western blot analysis of soluble and insoluble fractions of HEK293T cells transfected with the CARD domain-containing region of NOD1, NOD2, and RIPK2.

D Representative confocal images of HEK293T cells transfected with GFP-NOD1^{CARD}, GFP-NOD2^{CARD}, and GFP-RIPK2^{CARD}. Scale bar 5 μm.

E The soluble and insoluble fractions of *S. flexneri*-infected THP-1 (MOI 1:25, 8 h) cell lysates were subjected to Western blot analysis with indicated antibodies.

F Representative confocal images of immunofluorescence assays conducted with THP-1 cells infected with RFP expressing *S. flexneri* (pseudo-colored, blue) (MOI 1:25, 8 h). Line profile: co-localization analysis using line intensity profiles. Scale bar, 5 μm. Zoom panels are digital magnifications.

G Representative confocal images of immunofluorescence assays performed with HEK293T cells transfected with GFP-RIPK2 and Flag-NOD2 (upper panel) or Flag-NOD1 (lower panel). Line profile: co-localization analysis using line intensity profiles. Scale bar, 5 or 10 μm as indicated in figures. Inset zoom panels are digital magnifications.

H, I HEK293T cells were transfected with (H) full length and (I) CARD domains of NOD1, NOD2, and RIPK2 followed by Western blot analysis with soluble and insoluble fractions using indicated antibodies.

J, K Western blot analysis of soluble and insoluble fractions of RIPK2$^{+/+}$ and RIPK2$^{-/-}$ HT-29 cells infected with *S. flexneri* (MOI 1:25, 8 h) with indicated antibodies.

L, M Representative immunofluorescence images of doxycycline-inducible GFP-RIPK2 expressing HeLa cells. (L) Upper panel, uninfected. Lower panel, *S. flexneri*-infected MOI 1:25, 4 h). Immunostaining was performed with the p65 antibody (red) and DNA stained with DAPI (Blue). (M) The graph indicates % of cells that are RIPosomes positive or negative with nuclear/cytoplasmic p65 (5 fields (each group), Mean ± SD, $n = 3$). $^{****}P < 0.00005$, Student's unpaired *t*-test.

Source data are available online for this figure.

κB-p65, a signature of NF-κB activation. The p65 was not translocated into the nucleus in uninfected GFP-RIPK2 expressing cells (Fig 2L, upper panel), whereas a distinct nuclear translocation was observed in the *Shigella*-infected cells in which the RIPosomes are formed (Fig 2L, lower panel and M). However, within the *Shigella*-infected cells, the cells that are negative for RIPosomes, a majority had cytoplasmic p65 (Fig 2L, lower panel and M). Also, the nuclear translocation of phospho-p65 (Ser536) is significantly induced upon *Shigella* infection in GFP-RIPK2 overexpressing HeLa cells (Appendix Fig S2L). The data suggest that the biogenesis of RIPosome is important for the activation of NF-κB response.

To evaluate whether the NODo-RIPosomes could also induce NF-kB activation, we electroporated purified RIPosomes and NODo-RIPosomes into HEK293T cells. Both RIPosomes and NODo-RIPosomes induced NF-κB activation measured by luciferase reporter assays, where NODo-RIPosomes were consistently more efficient than RIPosomes in triggering NF-κB activation (Appendix Fig S2M).

NODs, RIPK2, and RIPosomes are the target of selective autophagy

We performed cycloheximide chase assays to determine the role of proteasome and/or autophagy processes in the turnover of endogenous NODs and RIPK2. The inhibition of autophagy flux using Bafilomycin A1 (Baf A1) completely protected RIPK2 and NOD1 from degradation, whereas proteasome inhibition using MG132 was partially protective (Fig EV1A and B). In the case of NOD2, only inhibition of autophagy protected it from degradation (Fig EV1C). These data indicate that autophagy plays a major role in the degradation of NODs and RIPK2. To confirm the role of autophagy in NODs and RIPK2 degradation, we monitored the levels of these proteins in ATG5 knockdown THP-1 or ATG5 knockout MEFs cells in uninfected and *Shigella*-infected cells. Enhanced amounts of RIPK2, NOD1, and NOD2 were detected in the ATG5-depleted cells both in control or *Shigella*-infected cells confirming that autophagy is critical in suppressing the levels of NODs and RIPK2 (Fig 3A and B).

Next, we tested whether RIPosomes are the target of autophagy. Treatment of cells with rapamycin dramatically reduced the number of RIPosomes (Fig 3C). This effect was completely rescued when the cells were additionally treated with Baf A1 (Fig 3C). Further, the numbers of RIPosome were significantly increased in the absence of ATG5 in *Shigella*-infected THP-1 cells (Fig 3D). Additionally, although RIPK2 soluble levels were induced in ATG5-depleted cells in basal conditions, RIPosomes (insoluble oligomeric aggregates) were formed only as a result of *Shigella* infection and were further induced in ATG5 KD cells (Fig 3E). Collectively, these results demonstrate that NODs and RIPK2 proteins as well as RIPosomes are the targets of autophagy.

SQSTM1/p62 mediates selective autophagy of ubiquitinated RIPosomes

Ubiquitin marks cargoes before the autophagy machinery recognizes them and degrades them (Shaid *et al*, 2013). The infection of *Shigella* induced the K63-linked ubiquitination of RIPK2 (Fig EV1D). An evident co-localization or juxtaposition of ubiquitin with RIPosomes was observed in HEK293T cells (Fig 3F) and *Shigella*-infected THP-1 cells (Fig EV1E). To understand whether ubiquitination of RIPosomes is important for their autophagic degradation, we inhibited ubiquitination in cells using PYR-41, which is a selective and cell-permeable inhibitor of ubiquitin-activating enzyme E1. In high-content microscopy, we found that rapamycin-induced autophagic degradation of RIPosomes is blocked by PYR-41 (Fig EV1F), indicating that ubiquitinated RIPosomes are the target of autophagy.

Autophagy receptor proteins are critical in bridging the ubiquitinated cargoes to the autophagosomes (Shaid *et al*, 2013). To identify the receptor that recognizes RIPK2, we screened the interaction between RIPK2 and key autophagy receptors, including p62, NBR1, NDP52, TAX1BP1, and Optineurin (Fig 3G). A strong physical interaction was observed between RIPK2 and p62 (Fig 3G). NBR1 was faintly bound and other receptors completely failed to interact with RIPK2 (Fig 3G). Thus, we tested whether p62 mediates autophagic degradation of RIPK2 and RIPosomes. Levels of both soluble and insoluble forms of RIPK2 were increased in *Shigella*-infected THP-1 cells upon p62 knockdown (Fig 3H). Also, we found an increased number of RIPosomes in p62 knockdown cells compared with

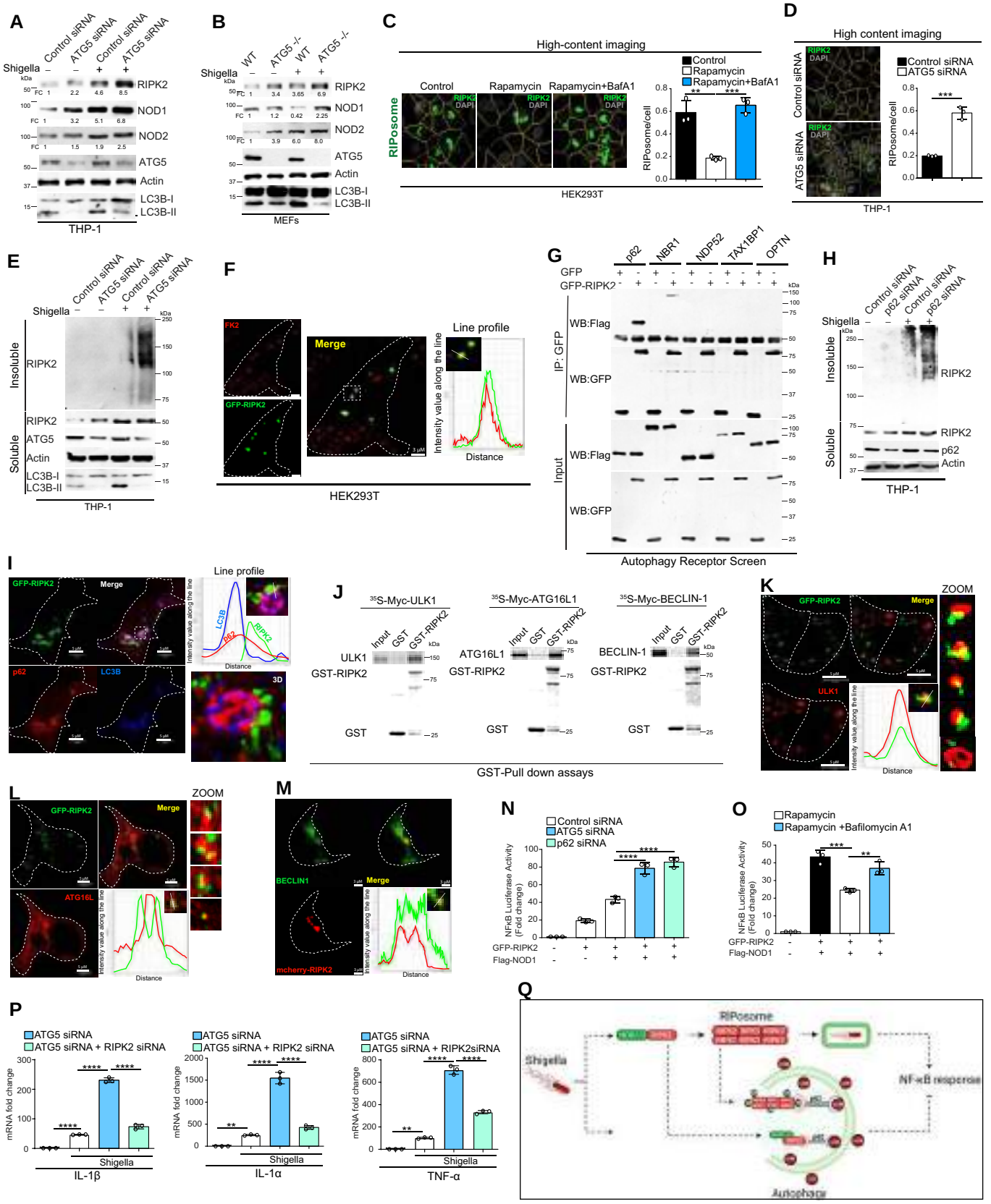

Figure 3.

Figure 3. NODs, RIPK2, and RIPosomes are degraded by p62-dependent selective autophagy.

A, B Western blot analysis with cell lysate of uninfected and *S. flexneri*-infected (MOI 1:25, 8 h) (A) control and ATG5 siRNA knockdown THP-1 cells, (B) wild-type (WT) and ATG5 knockout ($ATG5^{-/-}$) MEF cells with indicated antibodies. Densitometric analysis was performed using Image J software. FC, fold change.

C Left panel, representative high-content microscopy images of RIPosomes in HEK293T cells that are control cells or cells treated with rapamycin (500 nM, 4 h) or cells treated with rapamycin (500 nM, 4 h) and bafilomycin A1 (BafA1, 300 nM). Right panel, the graph depicts the average number of RIPosomes/cell. About 15,000 cells were plated per well and RIPosomes were screened in 35 fields per well. Mean ± SD, $n = 3$ (biological replicates), $^{**}P < 0.005$ and, $^{***}P < 0.0005$, ordinary one-way ANOVA (Tukey's multiple comparisons test).

D Left panel, representative high-content microscopy images of RIPosomes in control and ATG5 siRNA transfected THP-1 cells infected with *S. flexneri* (8 h). Right panel, the graph depicts average number of RIPosomes/cell. About 50,000 cells were plated per well and RIPosomes were screened in 35 fields per well. Mean ± SD, $n = 3$ (biological replicates), $^{***}P < 0.0005$, Student's unpaired *t*-test.

E The soluble and insoluble fractions of *S. flexneri*-infected (MOI 1:25, 8 h) control and ATG5 siRNA knockdown THP-1 cells were subjected to Western blot analysis with indicated antibodies.

F Representative confocal images of HEK293T cells transfected with GFP-RIPK2 and immunostained with anti-FK2 antibodies. Line profile: co-localization analysis using line intensity profiles. Scale bar, 3 μm.

G Autophagy receptor screen using co-immunoprecipitation (Co-IP) assay to analyze the interaction between GFP-RIPK2 and Flag-p62 or Flag-NBRI or Flag-NDP52 or Flag-TAX1BP1 or Flag-OPTINEURIN in HEK293T cell lysate.

H Western blot analysis of soluble and insoluble fractions of control and p62 siRNA transfected and *S. flexneri*-infected THP-1 cells (MOI 1:25, 8 h).

I Representative confocal images of HEK293T cells expressing GFP-RIPK2 (6 h) immunostained with p62 and LC3B antibodies. Zoom panels are digital magnifications.

J GST pull-down assay using purified GST or GST-RIPK2 proteins with in vitro translated ^{35}S radiolabeled myc-ULK1 or myc-ATG16L or myc-BECLIN1.

K–M Representative confocal images of HEK293T cells transfected with GFP-RIPK2 or mcherry-RIPK2 (9 h) and immunofluorescence assay performed with antibodies specific to (K) ULK1, (L) ATG16L (M) BECLIN1. Line profile: co-localization analysis using line intensity profiles. Scale bar, 5 or 3 μm as indicated. Zoom panels are digital magnifications.

N Luciferase assays were performed with ATG5 or p62 knockdown HEK293T cells transfected with NF-κB luciferase reporter vector pGL4.32 NFκB-RE, GFP-RIPK2, and Flag-NOD1 plasmids. Mean ± SD, $n = 3$ (biological replicates), $^{****}P < 0.00005$, ordinary one-way ANOVA (Tukey's multiple comparisons test).

O Luciferase assays performed with HEK293T cells transfected with NF-κB luciferase reporter vector pGL4.32NFκB-RE, GFP-RIPK2, and Flag-NOD1 plasmids followed by treatment with rapamycin (500 nM, 4 h) alone or in combination with bafilomycin A1 (300 nM, 5 h). Mean ± SD, $n = 3$ (biological replicates), $^{**}P < 0.005$ and $^{***}P < 0.0005$, ordinary one-way ANOVA (Tukey's multiple comparisons test). The control conditions and readings for Fig 3N and P are the same.

P The qRT–PCR analysis with total RNA isolated from the uninfected and *S. flexneri*-infected (MOI 1:25, 6 h) control or ATG5 knockdown or ATG5 and RIPK2 double knockdown THP-1 cells. Mean ± SD, $n = 3$ (biological replicates), $^{**}P < 0.005$, and $^{****}P < 0.00005$, ordinary one-way ANOVA (Tukey's multiple comparisons test).

Q Pictorial representation of results obtained in this section where we found that p62-dependent selective autophagy degrades NODs, RIPK2, and RIPosomes to suppress NF-κB cytokine response.

Source data are available online for this figure.

control cells (Fig EV1G), suggesting that p62 plays a critical role in the autophagic degradation of RIPosomes. In agreement, p62 and LC3B (autophagosomes) were either co-localized or juxtaposed to RIPosomes (Figs 3I and EV1H). The high-resolution microscopy and 3D rendering of images indicate that p62 tethered the RIPosome to LC3B decorated autophagosomes (Fig 3I). Also, LC3B was found to be co-localized with RIPosome recruited over the *Shigella* (Fig EV1I).

Next, we asked whether other key autophagosome initiations (ULK1) and elongation proteins (ATG16L1 and BECLIN1) interact and co-localize with RIPK2/RIPosomes. We found that *in vitro* translated ULK1, BECLIN1, and ATG16L1 directly interacted with purified GST-RIPK2 in GST pull-down assays (Fig 3J). Further, all the three important autophagy proteins were either completely co-localized or juxtaposed to the RIPosomes (Figs 3K–M and EV1J and K) indicating a *de novo* biogenesis of autophagosomes occurring adjacent to the RIPosomes for their degradation. When cargo is degraded via autophagy, typically autophagy receptors specifically p62 also subjected to degradation. We observed that p62 is degraded upon *Shigella* infection and this degradation is rescued upon Bafilomycin A1 treatment, suggesting that p62 is targeted by autophagy along with cargo upon *Shigella* infection (Fig EV1L).

The depletion of ATG5 and p62 significantly increased NOD1/RIPK2-dependent NF-κB activity in luciferase reporter assays (Fig 3N). Conversely, autophagy activation by rapamycin reduced the NOD1/RIPK2-dependent NF-κB activity (Fig 3O) that was rescued by Baf A1 treatment (Fig 3O). Finally, the depletion of ATG5 *or p62* significantly enhanced *Shigella*-induced NF-κB-mediated pro-inflammatory cytokine response (TNFα, IL-1β, and IL-1α) in THP-1 cells (Figs 3P and EV1M). This enhanced cytokine response was rescued by RIPK2 silencing (Figs 3P and EV1M), suggesting that autophagy suppresses RIPK2-dependent NF-κB pro-inflammatory cytokine response.

Altogether, we found that p62-dependent selective autophagy mediates the degradation of NODs, RIPK2, and RIPosomes to suppress NF-κB activation and pro-inflammatory cytokine response (Fig 3Q).

Autophagy protein, IRGM is recruited over the bacteria and interacts with RIPosomes

IRGM is an autophagy protein that plays a critical role in the selective autophagic degradation of pro-inflammatory proteins (Mehto *et al*, 2019a, 2019b; Jena *et al*, 2020; Chauhan *et al*, 2021). We set out to examine the role of IRGM in the autophagic degradation of NODs, RIPK2, and RIPosomes. For that, first, we tested whether IRGM interacts with NODs and RIPK2. In the immunoprecipitation (IP) assays, endogenous IRGM interacted with RIPK2 and NODs (Fig 4A and B). The interaction of IRGM with NOD1/RIPK2 and NOD2/RIPK2 complex is further increased when the cells were treated with iE-DAP (NOD1 agonist) or MDP (NOD2 agonist), respectively (Fig 4A and B). In IP assays with the HT-29 cell line stably expressing Flag-IRGM, IRGM immunoprecipitated endogenous NOD1, NOD2, and RIPK2 (Appendix Fig S3A). A strong interaction between overexpressed IRGM with NOD1, NOD2, and RIPK2 was also observed in HEK293T cells (Fig 4C and D, and Appendix Fig S3B). Furthermore, a direct interaction of purified

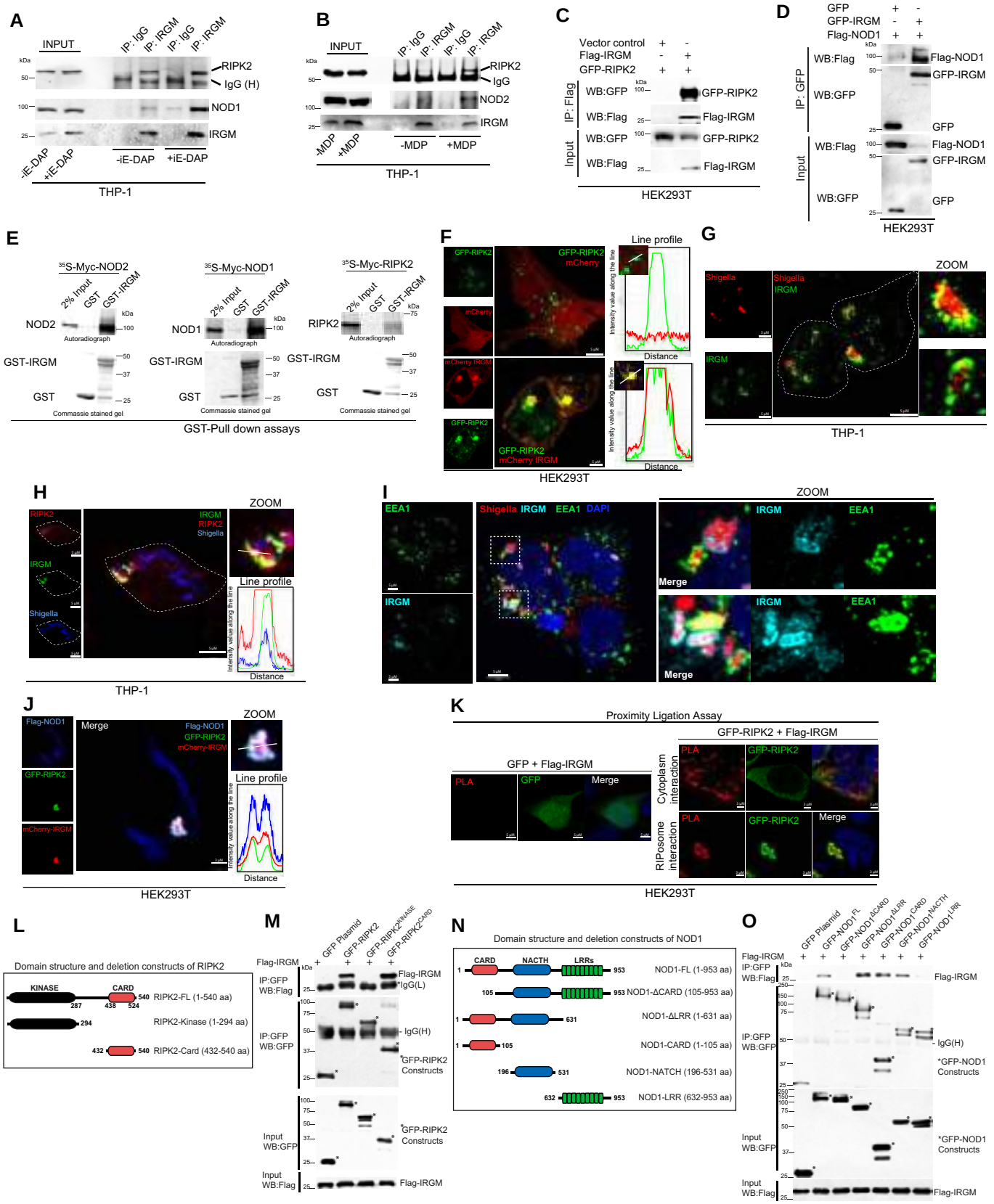

Figure 4.

Figure 4. Autophagy protein IRGM interacts and co-localizes with NODs, RIPK2, and RIPosomes.

A, B The THP-1 cell lysates were subjected to immunoprecipitation analysis (A) untreated and treated with iE-DAP (40 μg/ml, 6 h), (B) untreated and treated with MDP (40 μg/ml, 6 h). IP was performed with isotype control IgG or IRGM antibody and Western blotting was performed with indicated antibodies. IgG (H), IgG heavy chain.

C, D Co-IP analysis of the interactions between (C) GFP-RIPK2 and Flag-IRGM or (D) Flag-NOD1 and GFP-IRGM in HEK293T cell lysates.

E GST pull-down assay using purified GST and GST-IRGM and *in vitro* translated ^{35}S radiolabeled myc-NOD2, myc-NOD1, and myc-RIPK2.

F Representative confocal images of HEK293T cells expressing GFP-RIPK2 and mCherry or mCherry-IRGM. Line profile: co-localization analysis using line intensity profiles. Scale bar, 5 μm.

G, H Representative confocal images of THP-1 cells infected with RFP expressing *S. flexneri*, (MOI 1:25, 8 h) and immunostained with, (G) IRGM antibody (H) IRGM and RIPK2 antibody. Line profile: co-localization analysis using line intensity profiles. Scale bar, 5 μm. Zoom panels are digital magnifications. In image (H) for better contrast, RFP expressing *Shigella* is pseudo-colored to blue.

I Representative confocal images of THP-1 cells infected with RFP expressing *S. flexneri*, (MOI 1:25, 20 min) and immunostained with IRGM and EEA1 antibodies. DNA stained with DAPI. Scale bar, 5 μm. Zoom panels are digital magnifications.

J Representative confocal images of HEK293T cells expressing GFP-RIPK2, Flag-NOD1, and mCherry-IRGM. Line profile: co-localization analysis using line intensity profiles. Scale bar, 3 μm. Zoom panels are digital magnifications.

K Representative confocal images of proximity ligation assay (PLA) in HEK293T transfected with GFP or GFP-RIPK2 and Flag-IRGM plasmid. Scale bar 3 or 5 μm as indicated.

L The domain organization map of RIPK2 and deletion construct cloned as GFP-tagged proteins.

M A co-IP analysis is performed with HEK293T cell lysates expressing various domains of RIPK2 and IRGM to map the domain/s of RIPK2 interacting with IRGM. Asterisk indicates the main band of overexpressed protein.

N The domain organization map of NOD1 and deletion construct cloned as GFP-tagged proteins.

O A co-IP analysis is performed with HEK293T cell lysates expressing various domains of NOD1 and IRGM to map the domain/s of NOD1 interacting with IRGM. Asterisk indicates the main band of overexpressed protein.

Source data are available online for this figure.

GST-IRGM with NODs and RIPK2 was observed in GST pull-down assays (Fig 4E).

IRGM does not form oligomeric structures alone in the cells (Appendix Fig S3C). However, when expressed together with RIPK2, IRGM formed structures that were fully co-localized or juxtaposed to RIPosomes (Fig 4F and Appendix Fig S3D). Analysis of data from quantitative high-content microscopy displayed a high level of co-localization between IRGM and RIPK2 (Appendix Fig S3E). Interestingly, in *Shigella*-infected cells, IRGM was recruited to the intracellular bacteria (Fig 4G and Movie EV4) together with RIPosomes (Fig 4H). In some cells, we observed the formation of cage-like structures of RIPK2 and IRGM surrounding the bacteria (Appendix Fig S3F). *Shigella* is a predominantly cytosolic bacterium that ruptures its bacteria-containing vesicle very rapidly (within 10–15 min) after the invasion (Ray *et al*, 2010; Lopez-Montero & Enninga, 2018). Also, *Shigella* tends to avoid the recruitment of Rab GTPases and other maturation proteins (including LAMP proteins) using several mechanisms (Ray *et al*, 2010; Lopez-Montero & Enninga, 2018). We infected THP-1 cells with *Shigella* for 20 min and performed immunofluorescence with EEA1 (early phagosome/endosome marker) or LAMP2A (late phagosome maturation marker) and IRGM to understand whether IRGM is recruited to phagosomal or cytosolic *Shigella*. We found that very few bacteria were positive for EEA1 protein (Fig 4I) and did not observe LAMP2A recruitment over the *Shigella* (Appendix Fig S3G) confirming the previous observations. EEA1-marked phagosomes were rarely localized with IRGM, whereas IRGM was recruited to several of the bacteria. The data suggest that IRGM is recruited to *Shigella* once they escape phagosomes and are in the cytosolic compartment. Also, IRGM was found to be recruited on NODo-RIPosome complexes (Fig 4J and Appendix Fig S3H). IRGM and RIPK2 interaction was confirmed by proximity ligation assay (PLA), which reports direct protein–protein interactions (Fig 4K). Direct interaction between IRGM and RIPK2 was observed in the cytosol as well as over the RIPosomes (Fig 4K).

NOD2 interacts with IRGM primarily via CARD domain (Chauhan *et al*, 2015). We mapped the domain by which RIPK2 or NOD1 interact with IRGM. RIPK2 has one kinase and one CARD domain (Fig 4L), but only the CARD domain interacted with IRGM (Fig 4M). NOD1 consists of a CARD, a NACHT, and several LRR domains (Fig 4N). The CARD and NACTH domains are utilized by NOD1 to interact with IRGM (Fig 4O, lanes 5 and 6). No interaction was detected with the LRR domain (Fig 4O, lane 7). Consistently, deleting LRR domains did not affect the NOD1-IRGM interaction (or rather increased interaction; Fig 4O, lane 4); however, removing the CARD domain abolished NOD1-IRGM interaction (Fig 4O, lane 3), suggesting that the CARD domain may provide a primary interface for the interaction (Fig 4O, lane 3). Thus, the findings suggest that the CARD domain of NODs and RIPK2 provides a primary interface for interaction with IRGM.

In summary, IRGM strongly and specifically interacts with NODs and RIPK2. We show that IRGM is recruited to the cytosolic *Shigella* bacteria where it co-localizes with RIPosomes. Along with IRGM, other autophagy proteins including ULK1 and p62 were recruited to the *Shigella* bacteria (Appendix Fig S3I and J). ULK1 which is a known interaction partner of IRGM (Chauhan *et al*, 2015) was found to be completely covering the bacteria along with IRGM (Appendix Fig S3J).

IRGM mediates NODs, RIPK2, and RIPosome degradation to suppress NF-κB response

Next, we investigated how IRGM interaction with NODs, RIPK2, and RIPosomes modulates their functions. An increased protein level of RIPK2 and NODs was observed in IRGM CRISPR (partial) knockout HT-29 (IRGM$^{+/-}$) cells compared with the control cells (Fig 5A). The IRGM$^{+/-}$ HT29 cells are described previously (Jena *et al*, 2020). Also, *Shigella*-induced expression of NODs and RIPK2 was further enhanced in IRGM$^{+/-}$ HT-29 cells (Fig EV2A). Increased protein levels of NODs and RIPK2 were detected in colons and BMDMs of *Irgm1* knockout

(*Irgm1*$^{-/-}$) mice (Fig 5B). An increased amount of insoluble oligomeric RIPK2 was observed in Irgm1$^{-/-}$ BMDMs lysates as compared to the control cells (Fig 5B). Next, we used a HeLa cell line expressing stable doxycycline-inducible human GFP-RIPK2 (Ellwanger *et al*, 2019). Silencing IRGM in the *Shigella*-infected cells enhanced the levels of NODs and RIPK2 (Fig EV2B), and a significantly increased number of RIPosomes was observed (Fig 5C). Conversely, transient and stable overexpression of IRGM in HT-29, THP-1, and HEK293T cells resulted in degradation of endogenous and overexpressed NODs and RIPK2 (Figs 5D and E, and EV2C–E). Overexpression of IRGM significantly reduced the RIPosomes and NODo-RIPosomes formed in the cells (Figs 5F and EV2F). Also, the expression of IRGM reduced the insoluble oligomeric forms of RIPK2 and NOD2/RIPK2 (Figs 5G and EV2G). IRGM was found to be co-localized with RIPK2^{CARD} and was able to degrade the RIPK2^{CARD} filamentous structure into small punctate assemblies (Figs 5H, and EV2H and I). Taken together, the data show that IRGM mediates the degradation of NODs, RIPK2, and RIPosomes.

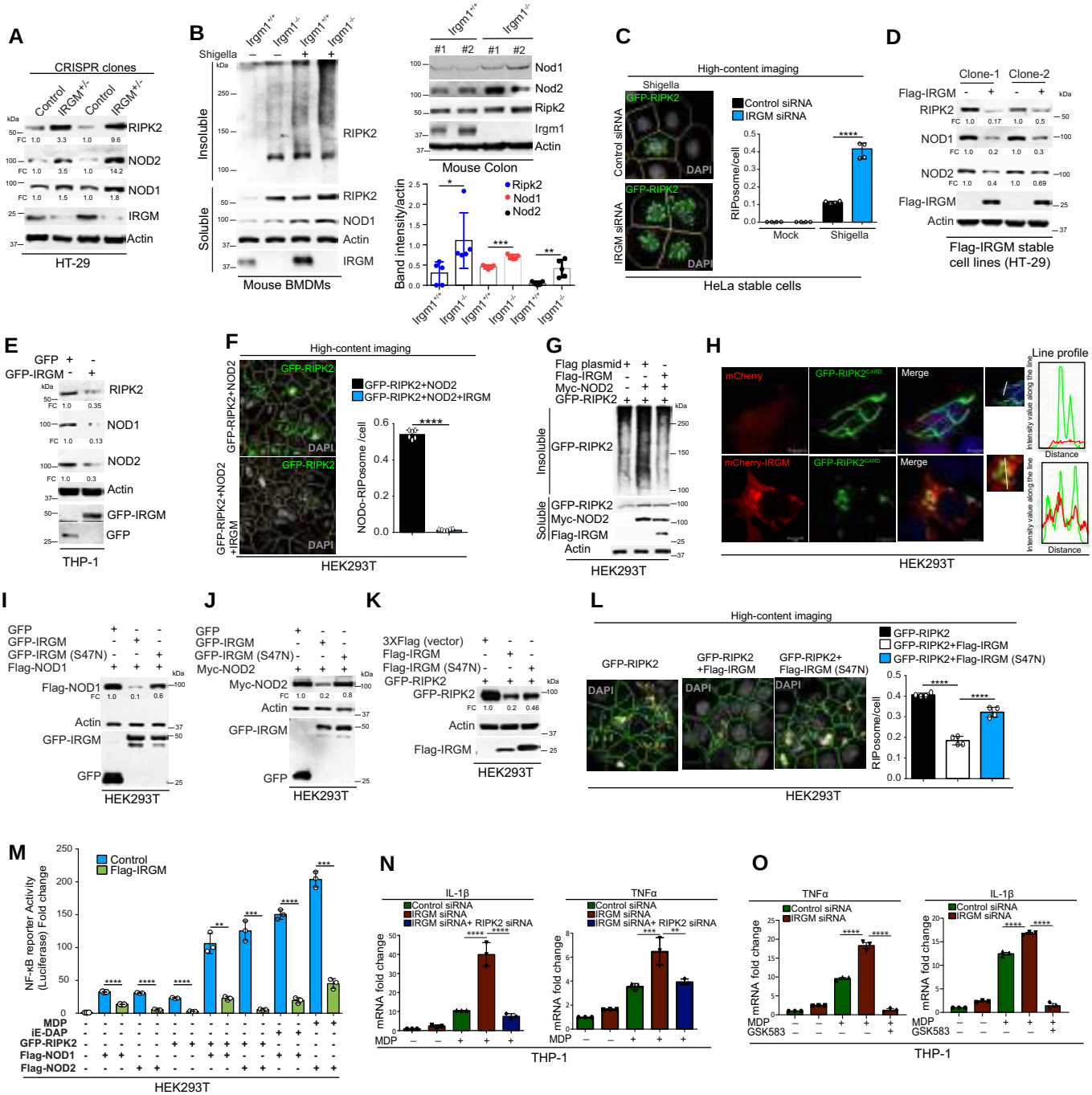

Figure 5.

Figure 5. IRGM mediates the degradation of NODs, RIPK2, and RIPosomes to suppress NF-κB-dependent cytokine response.

A Western blot analysis with the cell lysates of control CRISPR cells and CRISPR-Cas9 mediated IRGM partial knockout ($IRGM^{+/-}$) HT-29 cells (2 clones were tested). Densitometric analysis was performed using Image J software. FC, fold change.

B Left panel, soluble and insoluble fractions of *S. flexneri* (MOI 1:25, 8 h) infected mouse BMDMs from $Irgm1^{+/+}$ and $Irgm1^{-/-}$ mice were subjected to immunoblot analysis with antibodies as indicated. Right panel, Western blot analysis with the colon lysates from $Irgm1^{+/+}$ and $Irgm1^{-/-}$ mice with indicated antibodies. The graph indicate ratio of band intensity (measured using ImageJ) and actin (n = 5, Mean ± SD, *P < 0.05, **P < 0.005, and ****P < 0.00005, Student's unpaired t-test).

C Doxycycline-inducible stable GFP-RIPK2 HeLa cells were transfected with control siRNA or IRGM siRNA followed by infection with *S. flexneri* (MOI 1:25, 4 h). The cells were fixed and subjected to high-content microscopy to quantitate the number of RIPosomes formed. The graph depicts an average number of RIPosome/cell. About 10,000 cells were plated per well and RIPosomes were screened in 35 fields per well. Mean ± SD, n = 4 (biological replicates), ****P < 0.00005, Student's unpaired t-test.

D, E Western blot analysis with the cell lysate of (D) HT-29 clones stably expressing Flag-vector control or Flag-IRGM (E) THP-1 cells transiently transfected with GFP or GFP-IRGM for 6 h. Densitometric analysis was performed using Image J software. FC, fold change.

F Left panel, representative high-content microscopy images of NODo-RIPosomes in HEK293T cells transfected with GFP-RIPK2 and myc-NOD2 (upper panel) or GFP-RIPK2, myc-NOD2, and Flag-IRGM (lower panel). Right panel, the graph depicts average number of NODo-RIPosome/cell. About 15,000 cells plated per well and RIPosomes were screened in 35 fields per well. Mean ± SD, n = 5 (biological replicates), ****P < 0.00005, Student's unpaired t-test.

G The soluble and insoluble fractions of HEK293T cells transfected with indicated plasmids were subjected to immunoblot analysis with indicated antibodies.

H Representative confocal images of HEK293T cells transfected with mCherry and GFP-$RIPK2^{CARD}$ or mCherry-IRGM and GFP-$RIPK2^{CARD}$ for 9 h. Line profile: co-localization analysis using line intensity profiles. Scale bar, 5 μm.

I–K Western blot analysis with the cell lysates of HEK293T transfected with indicated plasmids and probe with Actin, Flag, Myc, and, GFP antibodies as indicated. Densitometric analysis was performed using Image J software. FC, fold change.

L Left panels, representative high-content microscopy images of HEK293T cells transfected with GFP-RIPK2 or GFP-RIPK2 and Flag-IRGM or GFP-RIPK2 and Flag-IRGM (S47N). The graph depicts the average number of RIPosome/cell. The details are mentioned in the legends of Fig 1F. Mean ± SD, n = 4 (biological replicates), ****P < 0.00005, ordinary one-way ANOVA (Tukey's multiple comparisons test).

M Luciferase assays performed with HEK293T cells transfected with NF-κB luciferase reporter vector pGL4.32NFκB-RE, along with plasmids as indicated, followed by treatment with MDP (10 μg/ml, 4 h) or iE-DAP (10 μg/ml, 4 h) as indicated. Mean ± SD, n = 3 (biological replicates), **P < 0.005, ***P < 0.0005 and ****P < 0.00005, Student's unpaired t-test.

N, O The qRT–PCR analysis with total RNA isolated from THP1 cells transfected with indicated siRNA and treated with (N) L-18 MDP (1 μg/ml, 6 h) for indicated genes (O) L-18 MDP (1 μg/ml, 6 h) and GSK583 (1 μM). Mean ± SD, n = 3 (biological replicates), *P < 0.05, **P < 0.005, ***P < 0.0005 and, ****P < 0.00005, ordinary one-way ANOVA (Tukey's multiple comparisons test).

Source data are available online for this figure.

A point mutation in the GTPase domain (Serine to Glycine at 47th position, S47N) of IRGM renders it inactive to perform autophagy functions (Chauhan *et al*, 2015; Kumar *et al*, 2018; Mehto *et al*, 2019a; Jena *et al*, 2020). As compared to wild-type IRGM, the catalytic mutant (S47N) of IRGM was unable to mediate the degradation of NOD1 (Fig 5I), NOD2 (Fig 5J), RIPK2 (Fig 5K), $RIPK2^{CARD}$ (Fig EV2J), and their oligomers (Figs 5L and EV2K). These results demonstrate the specificity of IRGM-mediated effects and also indicate the role of GTPase-dependent autophagy activity of IRGM in the degradation of NODs, RIPK2, and their oligomers.

Next, we examined the effect of IRGM on NODs/RIPK2-dependent NF-κB activation. First, we chased the phosphorylation (Ser536) status of p65 (p-p65) in the presence and absence of IRGM. The p-p65 is induced upon *Shigella* infection that is further increased upon IRGM knockdown (Appendix Fig S4A). The data suggest that *Shigella*-induced IRGM expression suppresses the NF-κB activation. In luciferase NF-κB reporter assays, IRGM strongly suppressed basal and NODs agonists (MDP and iE-DAP) induced NF-κB promoter activity (Fig 5M). We also employed an MDP-inducible NOD2 expressing secreted alkaline phosphatase (SEAP)-based NF-κB reporter cell line (Invivogen) to assess the effect of IRGM on NF-κB response. The overexpression of IRGM diminished MDP-induced NOD2 and NOD2-RIPK2 dependent NF-κB reporter activity (Fig EV2L). By contrast, silencing IRGM in MDP-treated THP-1 cells resulted in increased mRNA expression of IL-1β and TNFα (Fig 5N), which was restored in the RIPK2-depleted cells (Fig 5N). Similarly, GSK583, a specific and potent inhibitor of RIPK2 (Haile *et al*, 2016), suppressed the cytokine response increased upon IRGM knockdown (Fig 5O). Taken together, our results show that IRGM facilitates the degradation of NODs, RIPK2, and their oligomers to suppress NF-κB activity and cytokine response.

Endogenous IRGM levels in cells were increased upon exposure to *Shigella*, (Figs 5B, and EV2A and B; compare lanes 1 and 3), MDP (Appendix Fig S4B and D), and iE-DAP (Appendix Fig S4C and E). Thus, microbes and NODs agonists induce expression of IRGM that by a negative feedback loop mediates degradation of NODs-RIPK2 signaling proteins to suppress NF-κB response to maintain cell-autonomous innate immune homeostasis.

IRGM and p62 cooperate to conduct selective autophagy of NODs and RIPK2/RIPosomes

We scrutinized whether IRGM-dependent degradation of NODs and RIPK2 is mediated through proteasome or autophagy. Inhibition of autophagy flux (using Baf A1) but not proteasome (using MG132) restored the IRGM-dependent degradation of NODs and RIPK2 (Appendix Fig S5A–C). Further, the depletion of ATG5 rescued the IRGM-mediated degradation of endogenous (THP-1 cells; Fig EV3A and B) or overexpressed (HEK293T cells) NODs and RIPK2 (Fig EV3C–E). Also, the IRGM-dependent RIPosome degradation is restored when the cells were either depleted of ATG5 or were treated with Baf A1 (Fig EV3F). This and the above-discussed catalytic mutant ($IRGM^{S47N}$) data demonstrate that IRGM utilizes autophagy to degrade NODs, RIPK2, and RIPosomes. Further, PYR-41 (inhibitor of ubiquitin-activating enzyme E1) rescued the IRGM-mediated degradation of RIPK2, indicating that ubiquitinated RIPK2 is targeted by IRGM-dependent autophagy (Appendix Fig S5D).

Like RIPK2, IRGM interacts only with p62 among the autophagy receptor proteins (Jena *et al*, 2020). Therefore, we tested whether IRGM cooperates with p62 for the autophagic degradation of RIPK2 and RIPosomes. First, we investigated whether IRGM, p62, and RIPK2 are present in the same molecular complex. IRGM and p62 were co-localized or juxtaposed to the RIPosomes (also NODo-RIPosomes; Fig EV3G and Appendix Fig S5E and F). Also, co-localization/juxtaposition of RIPosomes, IRGM, and p62 with LC3B was observed (Appendix Fig S5G). Using sequential IP assay, we found that RIPK2, p62, and IRGM were present in the same complex (Fig EV3H). Silencing of p62 rescued the IRGM-dependent autophagic degradation of RIPosomes (Fig EV3I), and also IRGM-mediated degradation of overexpressed as well as endogenous RIPK2, NOD1, and NOD2 (Fig EV3J–M). Thus, IRGM utilizes p62 adaptor protein to mediate autophagic degradation of NODs, RIPK2, and RIPosomes. Next, we tested whether IRGM is required for the interaction between p62 and RIPK2. Indeed, the depletion of IRGM reduced the interaction between p62 and RIPK2 (Fig EV3N). Conversely, the presence of IRGM increased the interaction of p62 with NODs and RIPK2 (Fig EV3O–Q).

Taken together, the results show that IRGM and p62 cooperate to conduct inflammophagy of NODs, RIPK2, and RIPosome complexes. In addition, we observed that autophagy initiation and elongation protein ULK1 and ATG16L1 were co-localized with IRGM over the RIPosomes (Appendix Fig S5H and I), indicating that IRGM engages canonical autophagy machinery for degradation.

Combined results from this and the previous sections suggest microbes induce RIPosome formation and IRGM expression. Both IRGMs and RIPosomes are recruited over bacteria. Where RIPosome formation induces NF-κB response, IRGM-dependent autophagic degradation of NODs-RIPK2 complex suppresses the NF-κB response to balance the inflammatory outputs (Fig EV3R).

IRGM negatively regulates bacteria-induced RIPK2-dependent pro-inflammatory signaling pathways

To understand the role of IRGM in regulating host response to bacterial infection, we performed RNA-sequencing (RNA-seq) experiment with *Salmonella typhimurium* infected control and stable IRGM shRNA knockdown HT-29 colon cells. Hierarchical clustering based on gene ontology (GO) terms was performed using genes differentially regulated ($P < 0.05$, 1.5-fold) in basal and *Salmonella*-infected IRGM-depleted cells compared with controls. Several inflammatory (e.g., Interferon signaling and cytokine signaling) and infection-related processes (e.g. ER-phagosome and antigen processing/presentation) were among the top-enriched pathways (Reactome pathway analysis) induced in IRGM-depleted cells, which were further increased upon *Salmonella* infection (Datasets EV1 and EV2, and Fig EV4A). In basal conditions, IRGM suppresses a large number of IFN-stimulated genes (ISGs; Jena *et al*, 2020). Here, we found that during *Salmonella* infection, in addition to ISGs, IRGM suppressed a large number of chemokines (*CXCL1*, *2*, *3*, *5*, *6*, *8*, *10* and *CCL20*, *22*, *28*, etc.) interleukins (*IL1A*, *IL1B*, *IL1E/36G*, *IL17C*, *IL32*, *IL15*, etc.) and TNF superfamily genes (*TNFSF9*, *TNFSF10*, *TNFSF13*, *TNFSF15*, etc.; Dataset EV3, and Fig EV4B and C). Several other pathways such as endoplasmic reticulum-phagosome response, endosomal/vacuolar pathways, and antigen processing and presentation were upregulated in *Salmonella*-infected IRGM-depleted cells (Fig EV4A and B). The RNA-seq results were validated by performing qRT–PCR with several chemokines and interleukins (Fig EV4D). Next, to define the IRGM-dependent transcriptome that is exclusively upregulated upon *Salmonella* infection, we filtered out all the basal level deferentially upregulated genes and performed Reactome pathway analysis (Fabregat *et al*, 2018) with the rest of the transcriptome (Dataset EV4). In this analysis, the top-enriched pathways were TNFα signaling, IL-17 signaling, NF-κB signaling, interleukin-dependent signaling, interferon-gamma response, and NOD-like receptor signaling pathway (Fig EV4E). These data indicate that during bacterial infection IRGM limits an extensive and comprehensive program of pro-inflammatory response including NF-κB, TNFα, NODs, and IFN signaling pathways.

Our next step was to evaluate the extent to which IRGM-mediated suppression of the inflammatory response was dependent upon NOD1/2-RIPK2 signaling. For that, we performed RNA-seq analysis with *Shigella flexineri* infected WT, IRGM$^{+/-}$, and RIPK2-depleted IRGM$^{+/-}$ HT-29 cells. To better understand whether the suppression of the pro-inflammatory response by IRGM is specific to *Salmonella* or applies globally, we performed transcriptome analysis on *Shigella*-infected cells. A comparison of the analysis of the transcriptome induced in *Shigella* versus *Salmonella*-infected IRGM-depleted cells suggests that almost similar genes and pathways were upregulated in both the conditions (Fig EV4B vs. F, Dataset EV5), suggesting that IRGM has identical anti-inflammatory functions during different bacterial infections. Next, we performed the analysis with a set of genes that are significantly upregulated in IRGM$^{+/-}$ HT-29 cells (compared with control, $P < 0.05$, 1.5-fold, $n = 3$) and at the same time were significantly rescued by RIPK2 depletion ($P < 0.05$, 0.8, $n = 3$; Dataset EV6). A large number of genes (~250 genes) that were induced upon IRGM depletion were rescued by RIPK2 knockdown, suggesting that IRGM regulates pro-inflammatory responses through modulation of RIPK2 protein levels (Fig 6A and Dataset EV6). Metascape pathway analysis (Tripathi *et al*, 2015) with this gene set revealed that upon *Shigella* infection, IRGM suppresses several inflammatory responses including IFN response, NF-κB signaling, and interleukin signaling in a RIPK2-dependent manner (Fig 6B). Several of the NF-κB-regulated genes such us *NINJ1*, *MAPK11*, and cytokines such as CXCLs (*CXCL1*, *3*, *6*, *10*, *and 11*), Interleukins (*IL1α and IL1β*), tumor necrosis factors, and receptors (*TNF-α*, *TNSFAIP's*, *and TNSF's*), that were induced upon IRGM$^{+/-}$ were rescued by additional siRNA knockdown of RIPK2 (Fig 6C and D). Interestingly, during bacterial infection IRGM limited the interferon response in a RIPK2-dependent manner (Fig 6E and F). This was evident by the partial rescue of several sentinels' interferon-responsive genes including *IFITM's*, *GBP's*, *OAS1-3*, *MX1/2*, *ISG15*, and *RSAD2* when RIPK2 is knockdown in IRGM$^{+/-}$ HT-29 cells (Fig 6E and F). In agreement with these results, TRRUST (database of literature-curated human TF-target interactions; Han *et al*, 2018) analysis predicted RELA, NF-κB, and STAT1 as the major transcription factors for this response (Fig EV4G).

Taken together, these results demonstrate that IRGM suppresses multiple inflammatory responses during bacterial infection and limits the array of RIPK2-dependent pro-inflammatory responses.

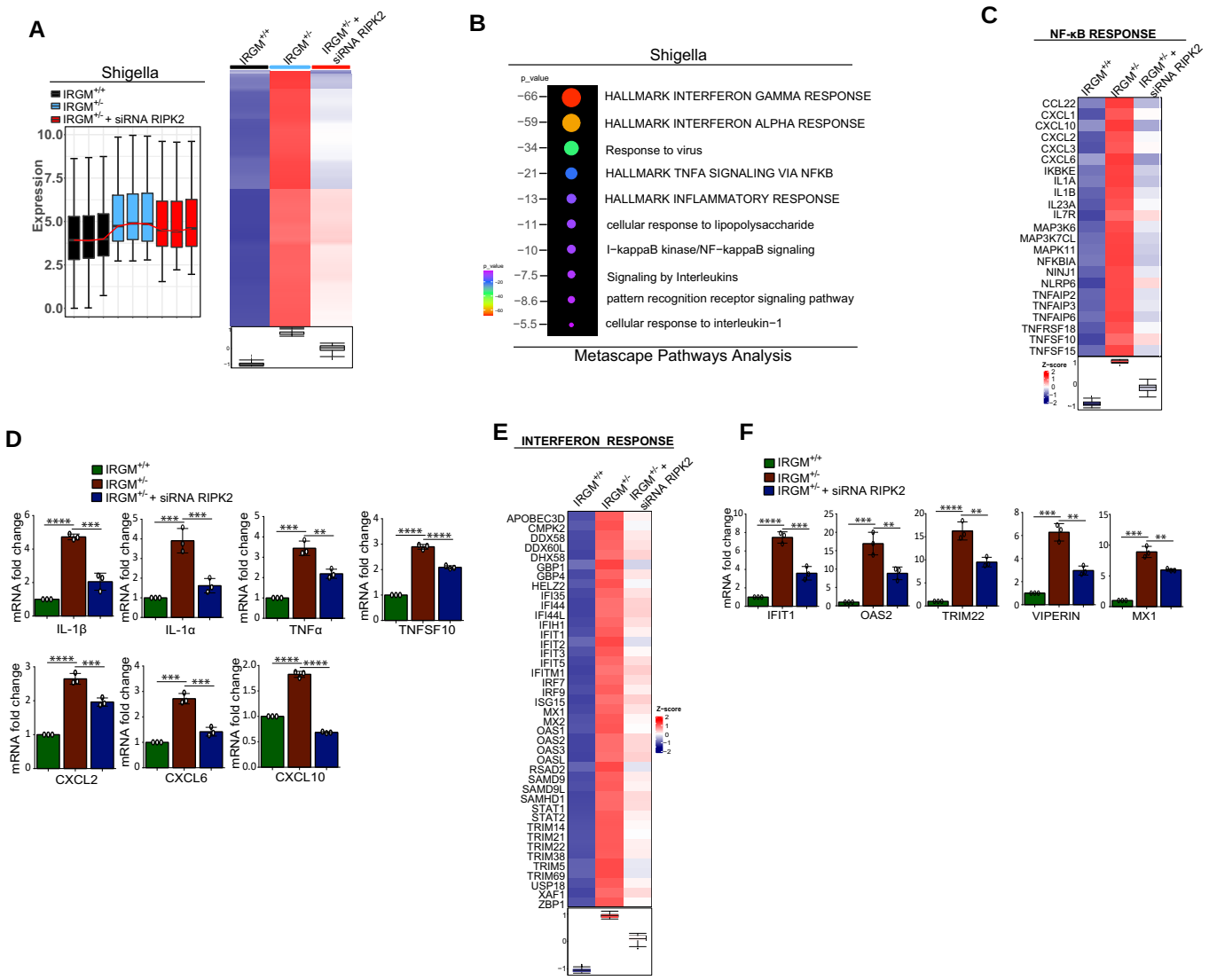

Figure 6. IRGM negatively regulates *Shigella*-induced RIPK2-dependent pro-inflammatory signaling pathways.

A Box plot distribution with normalized log expression (Left panel) and heatmap (Right panel) of the genes that were significantly upregulated in IRGM$^{+/-}$ HT-29 cells (compared with control; 1.5-fold, $P < 0.05$, Wald Chi-Squared test, $n = 3$, biological replicates) and at the same time were significantly rescued by RIPK2 depletion in IRGM$^{+/-}$ HT-29 cells ($P < 0.05$, 0.8, $n = 3$) infected with *S. flexneri* for 6 h (MOI 1:25). Left panel, the box and whisker plot shows upper and lower quartile of the datasets. Right panel, the graph below the heat map shows box plot with median obtained from data scaled to Z-score.

B Bubble plot graph depicting the overrepresented pathways (in order of *P*-value) obtained using Metascape pathway analysis software from the genes significantly upregulated in IRGM$^{+/-}$ cells (compared with control; 1.5-fold, $P < 0.05$, Wald Chi-Squared test, $n = 3$) and at the same time were significantly rescued by RIPK2 depletion in IRGM$^{+/-}$ HT-29 cells ($P < 0.05$, 0.8, $n = 3$) infected with *S. flexneri* for 6 h (MOI 1:25).

C Heatmap depicting the representative NF-κB responsive genes that were significantly upregulated in IRGM$^{+/-}$ cells (compared with control; 1.5-fold, $P < 0.05$, Wald Chi-Squared test, $n = 3$ biological replicates) and at the same time were significantly rescued by RIPK2 depletion in IRGM$^{+/-}$ HT-29 cells ($P < 0.05$, Wald Chi-Squared test, 0.8, $n = 3$ biological replicates). The graph below the heat map shows box plot with median obtained from data scaled to Z-score.

D The qRT–PCR analysis of NF-κB responsive cytokines and chemokines with total RNA isolated from the *S. flexneri*-infected IRGM$^{+/+}$, IRGM$^{+/-}$, and RIPK2-depleted IRGM$^{+/-}$ HT-29 cells. Mean ± SD, $n = 3$ (biological replicates), $^{**}P < 0.005$, $^{***}P < 0.0005$ and $^{****}P < 0.00005$, ordinary one-way ANOVA (Tukey's multiple comparisons test).

E Heatmap depicting the representative IFN response genes significantly upregulated in IRGM$^{+/-}$ cells (compared with control; 1.5-fold, $P < 0.05$, Wald Chi-Squared test, $n = 3$ biological replicates) and at the same time were significantly rescued by RIPK2 depletion in IRGM$^{+/-}$ HT-29 cells ($P < 0.05$, Wald Chi-Squared test, 0.8, $n = 3$, biological replicates). The graph below the heat map shows box plot with median obtained from data scaled to Z-score.

F The qRT–PCR analysis of NF-κB responsive cytokines and chemokines with total RNA isolated from the *S. flexneri*-infected IRGM$^{+/+}$, IRGM$^{+/-}$, and RIPK2-depleted IRGM$^{+/-}$ HT-29 cells. Mean ± SD, $n = 3$ (biological replicates), $^{**}P < 0.005$, $^{***}P < 0.0005$ and $^{****}P < 0.00005$, ordinary one-way ANOVA (Tukey's multiple comparisons test).

Source data are available online for this figure.

RIPK2 inhibition ameliorates shigellosis and DSS-induced gut inflammation in *Irgm1*^{KO} mice

Genetic variations in *IRGM* are associated with increased susceptibility to sepsis, bacterial infections, and gut inflammatory diseases (Massey & Parkes, 2007; Parkes *et al*, 2007; Intemann *et al*, 2009; Kimura *et al*, 2014). Consistently, *Irgm1*$^{-/-}$ mice were found to be more susceptible to DSS-induced colitis (Liu *et al*, 2013). Since we found that IRGM negatively regulates RIPK2-dependent pro-inflammatory responses, we hypothesized that therapeutic inhibition of RIPK2 could reduce gut inflammation associated with *Irgm1* depletion in shigellosis- and DSS-induced colitis models.

For *Shigella* infection in mice, we used the intraperitoneal model of shigellosis (Yang *et al*, 2014). In both colitis models, *Irgm1*-deficiency significantly accelerated body weight loss (Fig 7A and B) and increased the scores of stool consistency and rectal bleeding (Fig EV5A and B). Treatment of *Irgm1*$^{-/-}$ mice with the RIPK2 inhibitor GSK583 (Haile *et al*, 2016; Goncharov *et al*, 2018) significantly ameliorated the acute colitis symptoms (Figs 7A and B, and EV5A and B). Consistently, GSK583 was able to suppress the colon shortening in *Irgm1*$^{-/-}$ mice in both shigellosis- and DSS-induced colitis models (Figs 7C and EV5C). Next, we examined the severity of colon damage and inflammation by histopathological analysis using hematoxylin and eosin (H&E) staining. In *Irgm1*$^{-/-}$ mice, a significant increase in DSS-induced epithelial injury, loss of goblet cells, hyperplasia, and immune cell (neutrophils) infiltration was observed in the colon (Figs 7D and EV5D). Treatment of *Irgm1*$^{-/-}$ mice with GSK583 significantly attenuated histopathology and immune cell invasion (Figs 7D and EV5D). Similarly, *Shigella*-induced colon histopathology in *Irgm1*$^{-/-}$ mice was significantly improved by treatment with GSK583 (Fig EV5E and F).

An enhanced oligomerization of RIPK2 was observed in *Irgm1*$^{-/-}$ mice colon lysates that were dampened by the administration of GSK583 in these mice (Fig 7E). The increased levels of NF-κB (IL1α, IL1β, and TNF-α) and IFN (MX1, IFIT1, and ISG15) dependent cytokine response in *Irgm1*$^{-/-}$ mice colon were suppressed by treatment of GSK583 in both shigellosis- and DSS-induced colitis models (Figs 7F and EV5G). Immunohistochemistry analysis showed enhanced staining of IL1β in *Irgm1*$^{-/-}$ mice colon that was significantly reduced in GSK583-treated *Irgm1*$^{-/-}$ mice (Fig 7G). The enhanced expression of ISG15, RSAD2 (Viperin), and protein ISGylation (IFN response markers) in *Irgm1*$^{-/-}$ mice colon was considerably reduced upon treatment with GSK583 (Fig 7H). Similarly, GSK583 administration considerably diminished the increased protein levels of pro-caspase-1, cleaved caspase-1, phospho-p65, and phospho-p38MAPK in *Irgm1*$^{-/-}$ mice colon (Fig 7H and I).

Taken together, the data show that RIPK2 inhibition can ameliorate the gut inflammation and pathology associated with *Irgm1* deprivation in mouse colitis models.

Discussion

In this study, we made two major advances in understanding the regulation of NODs-RIPK2-NF-κB signaling. First, we revealed that when pathogenic bacteria infect cells, RIPK2 forms RIPosomes, which recruit over the bacteria and induce NF-κB response. Second, we show that autophagy suppresses NF-κB pro-inflammatory signaling by selectively degrading NODs, RIPK2, and RIPosomes. Consequently, this study demonstrates how the two cells' autonomous systems that are loaded over the bacteria work in concert for innate immune defense against the pathogens and cutting down excess inflammation as a safeguard.

The cryogenic electron microscopic (Cryo-EM) structure of RIPosomes was illustrated by two recent studies (Gong *et al*, 2018; Pellegrini *et al*, 2018). They found that RIPK2 forms a filamentous structure in cells using its CARD domain. Interestingly, the helical symmetry of RIPosomes and ASC filaments (Lu *et al*, 2014) was found to be strikingly similar suggesting that their assembly is governed by a similar mechanism. Further, they suggest that the CARDS of NOD1/2 may transiently interact with the CARD of RIPK2 to induce their oligomerization, similar to the phenomenon observed in RIG-I–MAVS signaling complexes (Wu & Hur, 2015). We found that RIPK2 can self-polymerize; however, both NOD1 and NOD2 failed to do so unless co-expressed with RIPK2. This is consistent with previous studies that suggest that NOD1/2 has a low propensity to self-associate (Fridh & Rittinger, 2012; Gong *et al*, 2018). Taken together, it appears that NODs monomers trigger RIPK2 oligomerization, which in turn increases the propensity of NODs to oligomerize and form NODo-RIPosomes.

Ellwanger *et al*, 2019 demonstrated that XIAP controls RIPK2 signaling by preventing its depositions in speck-like structures. Given the role of XIAP in autophagy, it will be interesting to determine whether XIAP has a role in the autophagic degradation of RIPosomes.

Figure 7. RIPK2 inhibition ameliorates shigellosis- and DSS-induced gut inflammation in *Irgm1* knockout mice.

A, B Upper panels, schematic representation of shigellosis- and DSS-induced colitis models used. In lower panels, the graph depicts percentage loss in body weight in *Irgm1*$^{+/+}$ and GSK583 untreated or treated *Irgm*$^{-/-}$ mice when (A) infected with *S. flexneri* (n = 6 mice) or (B) administrated with DSS (n = 3 mice). Mean ± SD, *P < 0.05, **P < 0.005, Student's unpaired t-test.

C Left panel, representative pictures of colons of *Irgm1*$^{+/+}$ and *Irgm*$^{-/-}$ mice untreated or treated with GSK583 infected with *S. flexneri*. Right panel, the graph depicts the average colon lengths of the mice groups. Mean ± SD, n = 6, **P < 0.005, ***P < 0.0005, Student's unpaired t-test.

D Representative microscopic images of H&E staining of colon tissues of *Irgm1*$^{+/+}$ and *Irgm*$^{-/-}$ mice untreated or treated with GSK583 administrated with DSS. The graph depicts the combined histological scores. Mean ± SD, n = 3 (DSS), **P < 0.005, Student's unpaired t-test. Scale bar, 200 μm.

E The soluble and insoluble fractionations of lysates from colon tissues of *Shigella*-infected or DSS-treated *Irgm1*$^{+/+}$ and *Irgm*$^{-/-}$ mice treated with GSK583 as indicated, were subjected to immunoblot analysis with indicated antibodies.

F The qRT–PCR analysis with total RNA isolated from the colon tissues of *S. flexneri*-infected Irgm1$^{+/+}$ or Irgm1$^{-/-}$ or GSK583-treated Irgm1$^{-/-}$ mice. Mean ± SD, n = 6–8, *P < 0.05, **P < 0.005, ***P < 0.0005, ordinary one-way ANOVA (Tukey's multiple comparisons test).

G Representative confocal images of IL-1β immunostained colon tissues of DSS-treated *Irgm1*$^{+/+}$ or *Irgm1*$^{-/-}$ or GSK583-treated *Irgm1*$^{-/-}$ mice. Scale bar, 10 μm.

H, I Western blot analysis with the colon tissue lysates of DSS-treated or *S. flexneri*-infected mice groups as indicated.

Source data are available online for this figure.

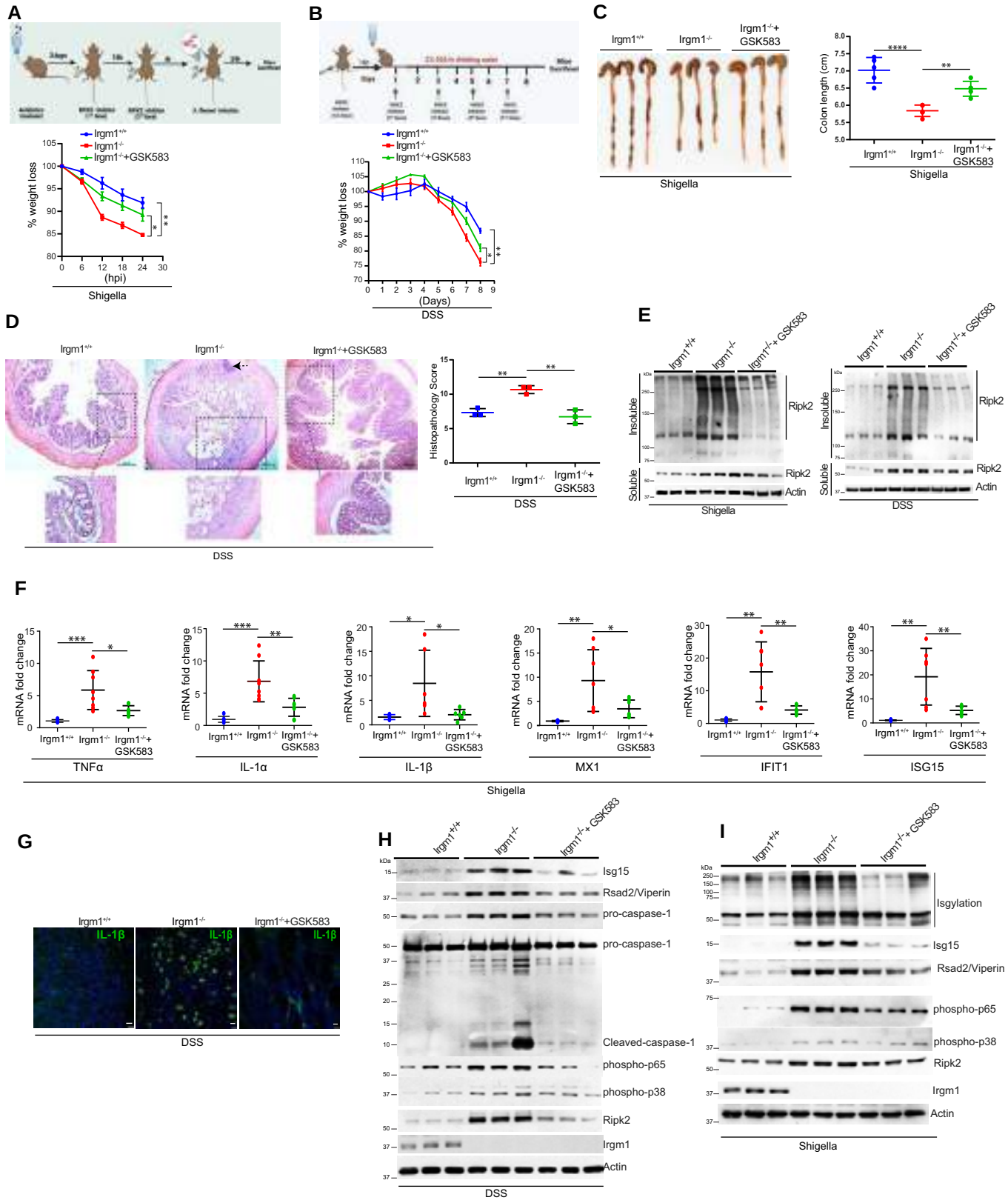

Figure 7.

We found that upon bacterial infection endogenous RIPK2 undergoes oligomerization to form RIPosomes in macrophages. Also, we found that pathogenic bacteria have a greater ability to induce RIPosome formation than nonpathogenic bacteria. At present, we do not understand the basis of this difference as both pathogenic and nonpathogenic bacteria produce ligands for NODs activation. It could be a possibility that, in addition to these ligands, some other bacterial factors are required to induce endogenous oligomerization of RIPK2. Consistently, the NODs agonist, MDP, or iE-DAP were inefficient in inducing RIPosome formation. Further studies are needed to identify the bacterial factors that enhance RIPosomes biogenesis. RIPosomes were either juxtaposed or recruited over the pathogenic bacteria. While NODs puncta co-localize with RIPosomes over bacteria, they are less consistent than RIPosome depositions suggesting that like RIG-I-MAVS interaction (Wu & Hur, 2015), NODs might transiently interact with RIPK2 to activate it.

The NODs-RIPK2-dependent NF-κB pro-inflammatory response is important to eliminate the invading pathogens. However, extensive inflammation could be deleterious and lead to immuno-pathologies. To prevent damage, cells employ several cell-autonomous mechanisms to tone down the inflammation. Genetic mutations in components of the NODs-RIPK2-NF-κB pathway predispose toward chronic autoimmune and inflammatory diseases (Miceli-Richard *et al*, 2001; Kanazawa *et al*, 2005; Henckaerts & Vermeire, 2007; Caso *et al*, 2015; Taniguchi & Karin, 2018). Therefore, it is critically important to understand the mechanisms that negatively control this pathway. Autophagy plays a significant role in suppressing inflammation and maintaining innate immune balance in the cell by degrading multiple inflammatory proteins/complexes (Chauhan *et al*, 2021; Deretic, 2021). Our previous study showed that IRGM act as a scaffold protein to bring NOD2-dependent bacterial sensing and autophagy machinery together to conduct antimicrobial defense (Chauhan *et al*, 2015). Here, we found that IRGM utilizes autophagy machinery to dampen the NOD2-RIPK2-dependent inflammation induced by pathogenic bacteria. Together, it emerges that IRGM has a dual function during bacterial infection. On the one hand, it leads to the clearance of intracellular bacteria by inducing xenophagy, and on the other hand, it reduces inflammation by inducing autophagic degradation of NODs and RIPK2.

IRGM is a genetic risk factor for several inflammatory and infectious diseases including inflammatory bowel disease, and tuberculosis (Massey & Parkes, 2007; Parkes *et al*, 2007; Lu *et al*, 2013; Kimura *et al*, 2014; Lin *et al*, 2016; Xia *et al*, 2017; Yao *et al*, 2018). The depletion of *Irgm1* in mice triggers inflammasome and IFN responses leading to autoimmune-like conditions. Depletion of IRGM led to upregulation of several inflammatory responses including NF-κB and IFN responses in a RIPK2-dependent manner that is blocked by chemical inhibition of RIPK2. These data suggest that RIPK2 inhibitors could be used as therapeutic options in patients with inflammatory diseases caused by the loss of function of IRGM.

Materials and Methods

Cell culture

All the common cell lines including THP-1 (ATCC TIB-202), HT-29 (ATCC HTB-38), and HEK293T (ATCC CRL-3216) cells were obtained from the American Type Cell Culture (ATCC), US. HEK-Blue hNOD2 cells were purchased from InvivoGen and maintained as per the instructions. HT-29, HEK293T, and HeLa cells were maintained in DMEM (GIBCO) supplemented with 10% heat-inactivated fetal bovine serum (FBS) and penicillin/streptomycin. THP-1 cells were maintained in RPMI-1640 (GIBCO) supplemented with 10% heat-inactivated FBS, Glucose (5%), HEPES buffer (10 mM), L-glutamine (5 mM), sodium pyruvate (1 mM), and penicillin/streptomycin. All the cell lines were tested for mycoplasma contamination routinely (every 2–3 months). All the experiments were performed with cells below the 20th passage.

Generation of CRISPR/Cas9 KO cell lines

The RIPK2 knockout HT-29 cell line is generated using the CRISPR-Cas9 method. Briefly, HT-29 cells seeded in 6-well plates and transfected with RIPK2/RICK Double Nickase Plasmid (Santacruz; sc-400,731-NIC) using ViaFect transfection reagent (Promega # E4981). After 48 h, GFP-positive cells were sorted into 96-well plates using MoFlo Asterio cell sorter (Beckman Coulter Life Sciences). The cells were grown in a growth medium containing 1 μg/ml puromycin for 1 week. The individual clones were selected and screened for knockout using Western blot analysis. The IRGM knockout HT-29 cell line was generated as described previously (Jena *et al*, 2020).

Inhibitors and reagents

N-Acetylmuramyl-L-alanyl-D-isoglutamine, MDP (InvivoGen # tlrl-mdp); γ-D-glutamyl-meso-diaminopimelic acid, iE-DAP (InvivoGen # tlrl-dap); 6-[(1,1-dimethylethyl) sulfonyl]-N-(5-fluoro-1H-indazol-3-yl)-4-quinolinamine, GSK583 (Cayman # 19739); Phorbol 12-myristate 13-acetate, PMA (Sigma # P8139); Bafilomycin A1 (CST# 54645S); Z-leu-leu-leu-al, MG132 (Sigma # C2211-5MG); Dextran sulfate sodium salt, DSS (MP Biomedicals # 160110), Ubiquitin E1 Inhibitor, PYR-41 (Sigma # 662105), ProLong Gold antifade reagent with DAPI (Invitrogen # P36931), ProLong Gold antifade reagent (Invitrogen # P36930).

Soluble-insoluble fractionation

For soluble-insoluble protein fractionation, cells were lysed in 1% Triton X-100 lysis buffer containing 150 mM NaCl, 50 mM Tris (pH 7.5), 10% glycerol, 1 mM EDTA, 1 mM PMSF, and protease inhibitor cocktail at 4°C for 20 min followed by centrifugation for 10 min at 17,000 *g* at 4°C. After centrifugation, the supernatant was used as a soluble fraction and the pellet was resuspended in lysis buffer with 1% SDS and used as an insoluble fraction for Western blot analysis.

Nuclear and cytoplasmic fractionation

Nuclear and cytoplasmic fractionation assay was performed using the NE-PER Nuclear and Cytoplasmic Extraction Reagents (ThermoFisher Scientific # 78833) according to the manufacturer's protocol. Briefly, 2 × 10^6 HeLa cells were infected with *S. flexneri* (MOI 1:25) for 4 h. The cells were harvested with trypsin–EDTA and centrifuged at 500 × *g* for 5 min. The cell pellet was washed with 1× PBS and resuspended in 200 μl CER I, vortexed vigorously for 15 s, and incubated on ice for 10 min. After the incubation, 11 μl of ice-

cold CER II were added to each sample, vortexed followed by incubation on ice for 1 min. The samples were centrifuged at 16,000 × *g* for 5 min to extract cytoplasmic fraction (supernatant) and the pellet (insoluble fraction) was resuspended in 100 µl NER, vortexed, incubated on ice with intermittent vortexing for 40 min. The samples were centrifuged at 16,000 × *g* for 10 min at 4°C to isolate nuclear fraction and subjected to western blot analysis.

Cycloheximide chase assay

Approximately, 2×10^6 HT-29 cells were plated in a 6-well plate and grown overnight. The next day, cells were treated with cycloheximide (100 µg/ml) with or without Bafilomycin A1 (300 nM) or MG132 (20 µM) for various time points. The cells were lysed in NP-40 lysis buffer containing 1× protease inhibitors cocktail and 1 mM PMSF and subjected to Western blotting with indicated antibodies.

Western blotting

The cells were lysed using NP-40 lysis buffer (Invitrogen # FNN0021) containing 1 mM PMSF (Sigma # P7626), phosSTOP (Roche # 49068455001), and protease inhibitors cocktail (Roche # 1183617000). Mice tissue were homogenized in radio-immunoprecipitation assay (RIPA) buffer (20 mM Tris, pH 8.0; 0.5 EGTA; 1 mM EDTA; 150 mM NaCl; 1% IGEPAL (Sigma); 10% glycerol; 0.1% Sodium deoxycholate). The protein concentration in the lysate was determined using the BCA method (Pierce™ BCA Protein Assay Kit # 23225). Lysates were separated using SDS–PAGE, transferred onto a nitrocellulose membrane (Bio-Rad), and blocked for 1 h in 5% skimmed milk followed by incubation in primary antibody overnight at 4°C. The membrane was washed with 1× PBS/PBST three times and then incubated with HRP conjugated secondary antibody for 1 h at room temperature. After washing with 1× PBS/PBST, the blots were developed using enhanced chemiluminescence reagents.

Immunofluorescence assay

Approximately, HEK293T/HeLa 10^5 cells were seeded on a coverslip and allowed to adhere overnight before transfection with plasmids. For THP-1 cells, approximately, 5×10^5 cells were treated with 50 ng/ml of PMA (Sigma # P8139) and seeded on the coverslip for differentiation into macrophages for 16 h. After a resting period of 24 h, cells were treated with stimulants or infected as required. The cells were fixed in 4% paraformaldehyde for 15 min, permeabilized with 0.1% Triton X-100 (or 0.1% saponin) for 15 min, followed by blocking with 1% bovine serum albumin (BSA) for 30 min at room temperature (RT). The permeabilized cells were then incubated with primary antibody as indicated for 1 h at RT or overnight at 4°C, washed thrice with 1× PBS, followed by incubation with Alexa fluor-conjugated secondary antibodies for 1 h at RT. The cells were washed thrice with 1× PBS, mounted with ProLong™ Gold antifade mountant with or without DAPI, air-dried, and visualized using a super-resolution Leica SP8 lightning confocal microscope.

Proximity ligation assay (PLA)

Proximity ligation assay (PLA) was performed using a Duolink *in situ* detection kit as per the manufacturer's protocol (Sigma #DUO92008). Briefly, 2×10^5 HEK293T cells were seeded on the coverslip and allowed to adhere overnight before transfection with the desired plasmids. After 12 h of transfection, cells were fixed with a 4% paraformaldehyde solution. Next, antigen retrieval was performed in sodium citrate buffer (10 mM, pH 6.0) and the cells were permeabilized with 0.1% Triton X-100 followed by blocking with 1× blocking solution (provided with the kit) in a preheated humidity chamber for 1 h at 37°C. The cells were incubated overnight with primary antibody diluted with diluent at 4°C. Next, the coverslips were washed twice with 1× wash buffer-A followed by incubation with Duolink *in situ* PLA probes in a preheated humidity chamber for 1 h at 37°C. After PLA probe incubation, coverslips were washed twice with 1× wash buffer-A followed by ligation with Duolink *in situ* ligase for 30 min in a preheated humidity chamber at 37°C. Next, coverslips were washed twice with 1× wash buffer-A followed by amplification through Duolink *in situ* polymerase for 90 min in a preheated humidity chamber at 37°C. Final washing was done twice with 1× and 0.01× wash buffer-B. The coverslips were mounted over glass slides using Duolink *in situ* mounting media with DAPI and the edges of the coverslip were sealed, mounted, and visualized using a Leica SP8 confocal microscope.

High-content microscopy imaging

For high-content microscopy imaging, approximately 17,000 HEK293T cells, 8,000 HeLa cells, and 50,000 PMA-treated THP-1 cells were seeded in a black flat bottom 96-well plate (Thermo Scientific, Nunc) and transfected with plasmids or treated or infected as indicated. The cells were fixed with 4% PFA and permeabilized with 0.1% Triton X-100 for 15 min, followed by blocking with 1% bovine serum albumin (BSA) for 30 min and incubation with primary antibody for 1 h. The cells were washed thrice with 1× PBS and incubated with secondary antibody for 1 h and then counterstained with 0.5 µg/ml of DAPI for 5 min. Imaging was performed by using Cell insight CX7 LZR high-content screening platform (Thermo Scientific). Automated image scanning and analysis were carried out using HCS studio and iDEV software, respectively. Automated images were captured at 10× (or 20×) by taking 1,500–20,000 cells and 35 fields per well or as indicated in figure legends. Images were quantified using scanning parameters and object mask definitions. A threshold value was set to find out the primary objects (cells). DAPI staining was used for autofocus and identification of the primary objects. The cells and regions of interest (ROI) or desired targets were further validated by total area, shape/segmentation, maximum/minimum average intensity, and total intensity. By using the cell mask and intensity of the puncta, the number of puncta per cell was counted. All data processed and analyzed were computer-based.

Hematoxylin and eosin (H&E) staining and immunohistochemistry analysis for mice colon tissue

The colon sections were deparaffinized and hydrated through an alcohol gradient followed by 1× PBS wash. For hematoxylin and eosin staining, the sections were stained with hematoxylin for 5 min followed by washing in water to remove excess stain. The sections were then incubated in Scott's tap water followed by staining with Eosin dye. The slides were washed, dehydrated in absolute ethanol, cleared in xylene, and mounted with DPX. Finally, slides were observed under Zeiss Apotome 2.0 microscope.

For immunohistochemistry, colon sections were deparaffinized and hydrated through ethanol gradient followed by 1× PBS wash. Antigen retrieval was performed in sodium citrate buffer (pH 6.0) for 10 min followed by permeabilization with 1× PBS (pH 7.4) containing 0.25% Triton X-100, blocked with goat serum. The slides were washed for 2 min thrice with PBS (pH 7.4) containing 0.05% Tween 20 followed by incubation of sections with an unconjugated affinity purified F(ab) fragment anti-mouse IgG (H + L) (Abcam #ab6668) for 1 h at room temperature. The sections were incubated overnight at 4°C with antibodies as indicated. The next day, the sections were washed twice with 1× PBS (pH 7.4) containing 0.05% Tween 20, followed by incubation with goat anti-rabbit/mouse IgG (H + L) Alexa Fluor 488/568 conjugated secondary antibody for 1 h. Sections were again washed and counterstained with DAPI for 1 min followed by incubation with an auto-fluorescence quencher (Vector Labs #SP-8400). Sections were finally mounted with Vectashield Vibrance Antifade mounting media. The slides were visualized under Leica TCS SP8 STED confocal microscope.

Co-immunoprecipitation assay

The cells were lysed in NP-40 lysis buffer containing 1× protease inhibitors cocktail and 1 mM PMSF for 20 min at 4°C and centrifuged at 12,000 *g* for 30 min at 4°C. The supernatant was incubated with the antibody at 4°C for 2 h on a rotational cell mixer followed by incubation with protein G Dynabeads (ThermoFisher#10003D) for 2 h at 4°C on a rotational cell mixer. The beads were washed with ice-cold 1× PBS four times, and the proteins were eluted from the beads in 2× SDS–PAGE Laemmli buffer by boiling for 5 min for Western blot analysis.

Glutathione S-Transferase (GST)-pull-down assay

The glutathione S-transferase (GST) pull-down assay was performed according to the previously described methods (Mehto *et al*, 2019a, 2019b). Briefly, GST or GST-RIPK2 or GST-IRGM recombinant proteins were expressed in *E. coli* SoluBL21 (Amsbio), and the proteins were purified on Glutathione Sepharose 4 Fast-Flow beads (GE Healthcare). The [^{35}S] labeled- Myc-NOD1, Myc-NOD2, Myc-RIPK2, Myc-ULK1, Myc-ATG16L1 or Myc-Beclin-1 proteins were *in vitro* translated using TnT T7–coupled reticulocyte lysate system (Promega). The GST proteins were incubated with [^{35}S]-labeled proteins in 200 µl of NETN-E buffer (50 mmol/l Tris, pH 8.0, 100 mm NaCl, 6 mm EDTA, 0.5% NP-40, and 1 mm dithiothreitol (DTT) supplemented with complete mini EDTA-free protease inhibitor cocktail; Roche) for 2 h at 4°C. After incubation, the beads were washed five times with NETN-E buffer, boiled with loading buffer, and subjected to SDS–PAGE. The gels were stained with coomassie blue and vacuum-dried. The GST was detected by staining with coomassie blue stain, whereas the [^{35}S]- labeled Myc-tagged proteins were detected in PharosFX imager (Bio-Rad Laboratories).

Antibodies and dilutions

Western blotting:

IRGM (Abcam # 69494; 1:500), NOD1 (CST# 3545S; 1:1000), NOD2 (Proteintech # 20980-1-AP; 1:1000), RIPK2 (CST#4142S; 1:1000), Anti-beta Actin (Abcam # ab6276; 1:5000), GFP (Abcam # ab290; 1:5000), Flag M2 (Sigma # F3165; 1:1000), p62 (BD Biosciences # BD-610832; 1:1000), ATG5 (CST # 2630S; 1:1000), c-Myc (Santa Cruz # sc-40; 1:1000), HA-Tag (CST # 3724S; 1:1000), RICK (Santa Cruz # sc-22,763; 1:1000), Anti-LC-3B antibody (Sigma # L7543; 1:1000), Anti-RICK A-10 (Santa Cruz # sc-166,765; 1:1000), IL-1β (CST#12242), Anti-pro Caspase1 + p10 + p12 Antibody (Abcam # ab179515; 1:1000), ISG15 (Santa Cruz# sc-166755; 1:500), Phospho-p38 MAPK (Thr180/Tyr182; 1:1000; CST#9211; 1:1000), Phospho-NF-κB p65 (ser536) (93H1) (CST# 3033; 1:1000). HRP conjugate secondary antibodies were purchased from Novus (1:2000) or Promega (1:5000).

Immunofluorescence

IRGM (Santa Cruz #68202; 1:50), RICK H-300 (Santa Cruz # sc-22,763; 1:100), NOD2 (Millipore # 04-145; 1:50), p62 (BD Biosciences # BD-610832; 1:250), LC3b (Sigma # L7543; 1:250), LC3b (MBL # PM036; 1:100), LAMP2A (Abcam # ab18528; 1:50), EEA1 (CST # 3288; 1:50), FK2 (MBL # D058-3;1:250), LC3b (CST # 83506, 1:50), IL-1β (CST # 12242), ULK1 (Santa Cruz # 33182; 1:100), c-Myc (Santa Cruz # sc-40; 1:500), Flag M2 (Sigma # F3165; 1:250), Alexa fluor Secondary antibodies (1:2000) were purchased from Thermo Fisher Scientific.

Plasmids and deletion constructs

The mcherry-RIPK2, GFP-RIPK2 and its deletion construct, GFP-NOD1 and its deletion construct and GFP-NOD2 were generated using gateway cloning strategy as per standard protocols (Invitrogen). pGL4.32[luc2P NF-kB-RE Hygro] purchased from Promega (Promega # E8491).

Transient transfection with siRNA

The THP-1 cells were electroporated using the Neon transfection system (Invitrogen # MPK5000; setting: 1400 V, 10 ms, 3 pulses, 100 µl tip) with 30 nM siRNA or as indicated: nontargeting siRNA, p62 siRNA (SASI_Hs01_00118616), IRGM siRNA (SASI_HS02_00518571), ATG5 (SASI_Hs01_00173156), human RIPK2 siRNA (SASI_Hs01_00199696), mice RIPK2 siRNA (SASI_Mm01_00188069) from Sigma-Aldrich. After 24-h transfection, one more time transfection was performed in a similar condition and incubated for an additional 48 h before the start of each experiment. The HT-29, HeLa, and HEK293T cells were transfected with 30 nM siRNA using Lipofectamine RNAiMAX transfection reagents (Invitrogen# 13778075) as per the manufacturer's instructions.

Transient transfection with plasmid

For transient transfection in THP-1, cells were electroporated using the Neon transfection system (Invitrogen # MPK5000; setting: 1400 V, 10 ms, 3 pulses, 100 µl tip). For overexpression experiments in HEK293T cells, required plasmids were transfected using the calcium phosphate method as per the manufacturer's instruction (Clontech, Promega).

Flag-RIPK2 protein electroporation

Approximately, 2×10^6 HEK293T cells transiently expressing pGL4.32NFκB-RE reporter plasmid electroporated with 10 µg

Purified Flag-RIPK2 in 100 µl neon resuspension buffer (setting: 1300 V, 10 ms, 1 pulse, 100 µl tip). The cells were harvested 6-h postelectroporation, and a luciferase assay was performed as described below.

NF-κB reporter assay

The NF-kb reporter assay was performed using a luciferase assay kit (Promega) according to the manufacturer's instructions and as described previously (Jena *et al*, 2020). Briefly, HEK293T cells were seeded into the 24-well plate. The next day, cells were transfected with pGL4.32 NF-κB-RE (Addgene100 ng) together with required plasmids using the calcium phosphate method. After 9 h, the growth medium was removed and cells were washed thrice with 1× PBS and lysed using 100 µl (1X) passive lysis buffer (Promega). The cell lysates were cleared by centrifugation at 12,000 *g* for 30 s at 4°C, and protein concentration was estimated using the BCA method. In a 96-well plate, 15 µg/20 µl lysate mixed with 100 µl LARII reagent and luminescence measurement was performed using a PerkinElmer VICTOR Nivo Multimode plate reader.

Secreted embryonic alkaline phosphatase (SEAP) reporter assay

Approximately, 3×10^5 HEK293-hNOD2 Blue cells were plated in a 6-well culture plate and incubated at 37°C in a 5% CO_2 incubator overnight. The next day, cells were transfected with the plasmids as indicated using the calcium phosphate method as per the manufacturer's instruction (Clontech, Promega). Six-hours post-transfection, the cell culture medium was replaced with fresh medium with or without L-18 MDP (100 ng/ml) and incubated at 37°C in a 5% CO_2 incubator for 24 h. SEAP activity was determined using QUANTI-Blue reagent as per the manufacturer's instruction. Briefly, in a flat bottom 96-well plate, 20 µl of sample supernatant was mixed with 180 µl of QUANTI-Blue solution and incubated for 30 min at 37°C. Optical density (OD) was measured at 620–655 nm using a microplate reader (Bio-Rad).

RNA isolation and quantitative real-time PCR

The total RNA was extracted using TRIzol™ isolation reagent (Invitrogen # 15596026) according to the manufacturer's protocol. One to two microgram of total RNA was used to synthesize cDNA using the high-capacity cDNA synthesis kit (Applied Biosystem #4368813), and qRT–PCR was performed using Power SYBR green PCR master mix (Applied Biosystem #4367659) or TaqMan master mix (Applied Biosystem # 4369016) according to the manufacturer's protocol. The assay was normalized using the housekeeping gene (GAPDH or β-Actin). The fold change in gene expression was calculated by the $2^{-\Delta\Delta Ct}$ method. The graphs were generated using Graph Pad software. The sequence for human and mouse qRT–PCR primers is shown in Appendix Table S1.

RNA-sequencing sample preparation

The total RNA was extracted from the cells using an RNeasy mini kit (QIAGEN #74104). The quality and quantity of RNA were checked using agarose gel and Qubit 3.0. After assessing the quality of RNA, ~850 ng of total RNA was taken for library preparation using NEBNext®Ultra™ II Directional RNA Library kit for Illumina® (# E7760L) and NEBNext® Poly (A) mRNA Magnetic Isolation Module (# E7490L) as per manufacturer's protocol. The prepared library was quantified using a Qubit dsDNA assay kit (Invitrogen, Q32851) followed by a quality check (QC) and fragment size distribution using a High Sensitivity Tape station Kit (Agilent 2200, 5067–5585, and 5067–5584). The library was sequenced using the HiSeq 4000 Illumina platform.

RNA-sequencing data processing and gene expression analysis

The paired-end (PE) reads quality checks for each sample were performed using FastQC v.0.11.5 (http://www.bioinformatics.babraham.ac.uk/projects/fastqc/). The adapter sequence was trimmed using the BBDuk version 37.58, and the alignment was performed using STAR v.2.5.3a with default parameters (Dobin *et al*, 2013) with human hg38 genome build, gencode v21 gtf 9GRCh38 from the gencode. Duplicates were removed using Picard-2.9.4 (https://broadinstitute.github.io/picard/) from the aligned files, and read counts were generated using featureCount v.1.5.3 from subread-1.5.3 package (https://bioweb.pasteur.fr/packages/pack@subread@1.5.3) with Q = 10 for mapping quality. The count files were used as input for downstream differential gene expression analysis with DESeq2 version 1.14.1 9. (Love *et al*, 2014). The genes with read counts of ≤ 10 in any comparison were removed followed by count transformation and statistical analysis using DESeq "R." The "*P*" values were adjusted using the Benjamini and Hochberg multiple testing correction (Haynes, 2013), and the differentially expressed genes were identified (fold change of ≥ 1.5, *P*-value < 0.05). A unified nonredundant gene list was made for different comparisons and subjected to gene ontology (GO) analysis using reactome database (https://reactome.org/). The top pathways ($P < 0.05$) were used for generating heat maps using Complexheatmap (Version 2.0.0) through unsupervised hierarchical clustering. The expression clusters were annotated based on enriched GO terms. Normalized gene expression was used to generate the boxplots with median depicting the trends in the expression across the different conditions using ggplot2 [version 3.3.5]. The pathways analysis was performed using Metascape database (https://metascape.org/gp/index.html#/main/step1). The top pathways ($P < 0.05$) were taken for constructing bubble plots using ggplot2 [version 3.3.5].

The basal conditions groups (for the *Salmonella* infection group) for the dataset E-MTAB-12074 are the same as described previously (Jena *et al*, 2020) and deposited under the accession number E-MTAB-9142 (http://www.ebi.ac.uk/arrayexpress/experiments/E-MTAB-9142). The RNA-sequencing experiment for the basal conditions (dataset E-MTAB-9142) and Salmonella-infected conditions (dataset E-MTAB-12074) was performed together. However, we have used basal conditions groups' dataset E-MTAB-9142 in our previous publication (Jena *et al*, 2020) and reanalyzed it here along with Salmonella-infected dataset E-MTAB-12074.

Bacterial strains and infection of cells in culture

Escherichia coli DH5α, *Salmonella typhimurium* strain *S*T 1433, and *Shigella flexneri* (MTCC:1457) (gifted by Dr. Suraj Kumar Tripathy, KIIT, India) were cultured in Luria-Bertani (LB) overnight at 37°C with shaking. Bacteria were subcultured (1:100 dilution) in fresh LB

broth and grown until OD_{600} reached 0.4–0.6. *Mycobacterium smegmatis* MC^2 155 *and Mycobacterium tuberculosis* H37Rv (gifted by Dr. Sunil Raghav, ILS, India) were grown in Middlebrook 7H9 liquid medium supplemented with 5 g/l albumin, 2 g/l dextrose, and 0.003 g/l catalase along with 0.05% tween 80.

For fluorescence microscopy, THP-1 cells were treated with PMA (50 ng/ml) and seeded onto glass coverslips in 12-well plates and kept for differentiation. After 16 h, the medium was replaced with fresh medium and incubated for another 24 h. Cells were infected with *Shigella flexneri* 1457 (MOI, 1:25 or 1:50), *Salmonella typhimurium* strain *S*T 1433 (MOI, 1:10), *E. coli* LF-82 (MOI, 1:10), *Mycobacterium smegmatis* MC^2 155 (MOI, 1:10), *and Mycobacterium tuberculosis* H37Rv (MOI, 1:10). Infection was facilitated by centrifugation at 700 × *g* for 10 min at room temperature and proceeded for 2 h at 37°C on 5% CO_2 incubator. Infected cells were washed three times with 1× PBS and fixed with 4% paraformaldehyde for 30 min at room temperature.

For the RNA-sequencing experiment, approximately 3×10^6 HT-29 cells were seeded in a 60 mm dish and allowed to adhere overnight. The cells were infected with *Shigella flexneri* 1457 (1:25 MOI, 6 h) or *Salmonella typhimurium* strain *S*T 1433 (MOI, 1:10, 8 h).

Intraperitoneal *Shigella* infection in mice

The mice experiments were performed with the procedure approved by the institutional animal ethical committee at the Institute of Life Sciences (ILS), Bhubaneswar, India. The mice were housed at the animal house facility of ILS. C57BL/6 wild-type and *Irgm1* knockout mice were described previously (Liu *et al*, 2013). About 6–8-week-old male $Irgm1^{+/+}$ (wild-type, $n = 9$) and $Irgm1^{-/-}$ ($n = 18$, includes GSK583 group) mice were used for the infection. Intraperitoneal infection of *S. flexneri* was performed as reported previously (Yang *et al*, 2014). Briefly, *Shigella* was cultured to the O.D. of 0.4–0.5 and 10^8 colony-forming units (CFU) were injected intraperitoneal into the mice. GSK583 (30 mg/kg of body weight) is administered intraperitoneally 6 h before the infection. Mice were monitored for body weight, stool consistency, and other clinical parameters. All mice were sacrificed 24-h postinfection. The fecal pathology scores were assigned as follows: stool consistency (0, normal; 1, loose; 2, soft; 3, hard) and color (0, brown; 1, yellow; 2, light green; 3, green).

Pathological scores assigned in colon tissue sections for *Shigella* infection in mice based on the following parameter (Erben *et al*, 2014): hyperplasia (1, less than 25%; 2, mild 26–35%; 3, moderate 36–50%; 4, marked 51% above), loss of goblet cells(1, minimal less than 25%; 2, mild 26–35%; 3, moderate 36–50%; 4, marked 51% above), Leucocytes infiltrate (1, minimal less than 10%; 2, mild 26–35%; 3, moderate 36–50%; 4, marked 51% above).

Dextran sulfate sodium (DSS)-induced colitis model in mice

The 6–7-week-old female C57BL/6 $Irgm1^{+/+}$ ($n = 3$) and $Irgm1^{-/-}$ ($n = 6$, including GSK583 group) mice were used for the DSS-induced colitis experiment. All the mice were given 2% (wt/vol) DSS dissolved in drinking water for 8 days. The DSS solution was replaced on alternate days. To inhibit the RIPK2, GSK583 (25 mg/kg) was injected intraperitoneally (i.p) 16 h before the start of DSS treatment and also injected intraperitoneally on the 1st, 3rd, 5th, and 7th day. The control group mice were injected intraperitoneally with vehicle control. Each day, mice were monitored for body weight, stool consistency, and the presence of blood in feces. The stool scores were assigned as follows: 0, well-formed pellets; 1, semisolid; 2, semisolid and not adhere to the anus; 3, liquid and adhere to the anus; and 4, diarrhea. Bleeding scores were assigned as follows; 0, no blood in stool; 1, light faint; 2, clear visible; and 3 gross rectal bleeding. The mice were sacrificed on the 9th day. The entire colon was extracted and measured using the vernier scale. The colon tissue was homogenized in RIPA buffer or Triton X-100 buffer containing PMSF, phosSTOP, and protease inhibitors cocktails and subjected to Western blotting. The tissue was homogenized in trizol for total RNA extraction.

Pathological scores assigned in colon tissue sections for DSS-induced colitis mice based on the following parameter (Erben *et al*, 2014): hyperplasia (1, less than 25%; 2, mild 26–35%; 3, moderate 36–50%; 4, marked 51% above), loss of goblet cells (1, minimal less than 25%; 2, mild 26–35%; 3, moderate 36–50%; 4, marked 51% above), Leucocytes infiltrate (1, minimal less than 10%; 2, mild 26–35%; 3, moderate 36–50%; 4, marked 51% above).

Software and statistical significance

GraphPad Prism 6 was used to analyze and present most of the data. High-content microscopy imaging data were scanned and analyzed using HCS studio and iDEV software, respectively. The number of biological/technical replicates mentioned in each figure legend. The unpaired Student's *t*-test or ordinary one-way ANOVO (Tukey's multiple comparison test) statistical methods are used as appropriate. The *P*-values are mentioned in graphs as appropriate. The densitometry analysis was performed using Image J software.

All the graphical representations are created using Biorender online tool (https://biorender.com/).

Data availability

The RNA-seq datasets produced in this study have been deposited in the ArrayEXpress database at EMBL-EBI (www.ebi.ac.uk/arrayexpress) under accession numbers E-MTAB-12067 and E-MTAB-12074.

Expanded View for this article is available online.

Acknowledgements
This work is funded by Wellcome Trust/Department of Biotechnology (DBT) India Alliance (IA/I/15/2/502071) fellowship to SC, extramural grant from the Department of Biotechnology (DBT, BT/PR45223/MED/29/1613/2022) to SC, and DST-Inspire faculty fellowship (DST/INSPIRE/04/2019/001857) to SM. Funding from EMBO Global investigator fellowship to SC is greatly acknowledged. We gratefully acknowledge the support of the Institute of Life Sciences central facilities (Animal house, microscopy, FACS, and sequencing) funded by the Department of Biotechnology (India).

Author contributions
Santosh Chauhan: Conceptualization; data curation; formal analysis; supervision; funding acquisition; investigation; visualization; methodology; writing – original draft; project administration; writing – review and editing.
Subhash Mehto: Data curation; supervision; funding acquisition;

validation; investigation; methodology; writing – review and editing. **Kautilya Kumar Jena:** Data curation; formal analysis; investigation; methodology; writing – review and editing. **Rina Yadav:** Data curation; investigation; methodology. **Swatismita Priyadarsini:** Validation; investigation; methodology. **Pallavi Samal:** Investigation; methodology. **Sivaram Krishna:** Investigation; methodology. **Kollori Dhar:** Investigation; methodology. **Ashish Jain:** Investigation; methodology. **Nishant Ranjan Chauhan:** Investigation; methodology. **Krushna Chandra Murmu:** Investigation; methodology. **Ramyasingh Bal:** Investigation; methodology. **Rinku Sahu:** Investigation; methodology. **Pundrik Jaiswal:** Investigation; methodology. **Bhabani Sankar Sahoo:** Investigation; visualization. **Srinivas Patnaik:** Supervision; methodology. **Thomas A Kufer:** Resources; writing – review and editing. **Tor Erik Rusten:** Resources; supervision. **Swati Chauhan:** Data curation; investigation; methodology. **Punit Prasad:** Resources; supervision; visualization.

Disclosure and competing interests statement

The authors declare that they have no conflict of interest.

References

Cai X, Chen J, Xu H, Liu S, Jiang QX, Halfmann R, Chen ZJ (2014) Prion-like polymerization underlies signal transduction in antiviral immune defense and inflammasome activation. *Cell* 156: 1207 – 1222

Caruso R, Warner N, Inohara N, Nunez G (2014) NOD1 and NOD2: signaling, host defense, and inflammatory disease. *Immunity* 41: 898 – 908

Caso F, Galozzi P, Costa L, Sfriso P, Cantarini L, Punzi L (2015) Autoinflammatory granulomatous diseases: from Blau syndrome and early-onset sarcoidosis to NOD2-mediated disease and Crohn's disease. *RMD Open* 1: e000097

Chauhan S, Jena KK, Mehto S, Chauhan NR, Sahu R, Dhar K, Yadav R, Krishna S, Jaiswal P, Chauhan S (2021) Innate immunity and inflammophagy: balancing the defence and immune homeostasis. *FEBS J* 289: 4112 – 4131

Chauhan S, Mandell MA, Deretic V (2015) IRGM governs the core autophagy machinery to conduct antimicrobial defense. *Mol Cell* 58: 507 – 521

Deretic V (2021) Autophagy in inflammation, infection, and immunometabolism. *Immunity* 54: 437 – 453

Dobin A, Davis CA, Schlesinger F, Drenkow J, Zaleski C, Jha S, Batut P, Chaisson M, Gingeras TR (2013) STAR: ultrafast universal RNA-seq aligner. *Bioinformatics* 29: 15 – 21

Du Y, Duan T, Feng Y, Liu Q, Lin M, Cui J, Wang RF (2018) LRRC25 inhibits type I IFN signaling by targeting ISG15-associated RIG-I for autophagic degradation. *EMBO J* 37: 351 – 366

Ellwanger K, Briese S, Arnold C, Kienes I, Heim V, Nachbur U, Kufer TA (2019) XIAP controls RIPK2 signaling by preventing its deposition in speck-like structures. *Life Sci Alliance* 2: e201900346

Erben U, Loddenkemper C, Doerfel K, Spieckermann S, Haller D, Heimesaat MM, Zeitz M, Siegmund B, Kuhl AA (2014) A guide to histomorphological evaluation of intestinal inflammation in mouse models. *Int J Clin Exp Pathol* 7: 4557 – 4576

Fabregat A, Jupe S, Matthews L, Sidiropoulos K, Gillespie M, Garapati P, Haw R, Jassal B, Korninger F, May B *et al* (2018) The Reactome pathway knowledgebase. *Nucleic Acids Res* 46: D649 – D655

Fridh V, Rittinger K (2012) The tandem CARDs of NOD2: intramolecular interactions and recognition of RIP2. *PLoS ONE* 7: e34375

Girardin SE, Tournebize R, Mavris M, Page AL, Li X, Stark GR, Bertin J, DiStefano PS, Yaniv M, Sansonetti PJ *et al* (2001) CARD4/Nod1 mediates NF-kappaB and JNK activation by invasive *shigella* flexneri. *EMBO Rep* 2: 736 – 742

Glasser AL, Boudeau J, Barnich N, Perruchot MH, Colombel JF, Darfeuille-Michaud A (2001) Adherent invasive *Escherichia coli* strains from patients with Crohn's disease survive and replicate within macrophages without inducing host cell death. *Infect Immun* 69: 5529 – 5537

Goncharov T, Hedayati S, Mulvihill MM, Izrael-Tomasevic A, Zobel K, Jeet S, Fedorova AV, Eidenschenk C, deVoss J, Yu K *et al* (2018) Disruption of XIAP-RIP2 association blocks NOD2-mediated inflammatory signaling. *Mol Cell* 69: 551 – 565

Gong Q, Long Z, Zhong FL, Teo DET, Jin Y, Yin Z, Boo ZZ, Zhang Y, Zhang J, Yang R *et al* (2018) Structural basis of RIP2 activation and signaling. *Nat Commun* 9: 4993

Haile PA, Votta BJ, Marquis RW, Bury MJ, Mehlmann JF, Singhaus R Jr, Charnley AK, Lakdawala AS, Convery MA, Lipshutz DB *et al* (2016) The identification and pharmacological characterization of 6-(tert-Butylsulfonyl)-N-(5-fluoro-1H-indazol-3-yl)quinolin-4-amine (GSK583), a highly potent and selective inhibitor of RIP2 kinase. *J Med Chem* 59: 4867 – 4880

Han H, Cho JW, Lee S, Yun A, Kim H, Bae D, Yang S, Kim CY, Lee M, Kim E *et al* (2018) TRRUST v2: an expanded reference database of human and mouse transcriptional regulatory interactions. *Nucleic Acids Res* 46: D380 – D386

Haynes W (2013) Benjamini–Hochberg method. In *Encyclopedia of Systems Biology*, Dubitzky W, Wolkenhauer O, Cho K-H, Yokota H (eds), pp 78 – 78. New York, NY: Springer New York

He X, Zhu Y, Zhang Y, Geng Y, Gong J, Geng J, Zhang P, Zhang X, Liu N, Peng Y *et al* (2019) RNF34 functions in immunity and selective mitophagy by targeting MAVS for autophagic degradation. *EMBO J* 38: e100978

Henckaerts L, Vermeire S (2007) NOD2/CARD15 disease associations other than Crohn's disease. *Inflamm Bowel Dis* 13: 235 – 241

Hou F, Sun L, Zheng H, Skaug B, Jiang QX, Chen ZJ (2011) MAVS forms functional prion-like aggregates to activate and propagate antiviral innate immune response. *Cell* 146: 448 – 461

Intemann CD, Thye T, Niemann S, Browne EN, Amanua Chinbuah M, Enimil A, Gyapong J, Osei I, Owusu-Dabo E, Helm S *et al* (2009) Autophagy gene variant IRGM -261T contributes to protection from tuberculosis caused by *Mycobacterium tuberculosis* but not by *M. africanum* strains. *PLoS Pathog* 5: e1000577

Jena KK, Mehto S, Nath P, Chauhan NR, Sahu R, Dhar K, Das SK, Kolapalli SP, Murmu KC, Jain A *et al* (2020) Autoimmunity gene IRGM suppresses cGAS-STING and RIG-I-MAVS signaling to control interferon response. *EMBO Rep* 21: e50051

Kanazawa N, Okafuji I, Kambe N, Nishikomori R, Nakata-Hizume M, Nagai S, Fuji A, Yuasa T, Manki A, Sakurai Y *et al* (2005) Early-onset sarcoidosis and CARD15 mutations with constitutive nuclear factor-kappaB activation: common genetic etiology with Blau syndrome. *Blood* 105: 1195 – 1197

Kimura T, Watanabe E, Sakamoto T, Takasu O, Ikeda T, Ikeda K, Kotani J, Kitamura N, Sadahiro T, Tateishi Y *et al* (2014) Autophagy-related IRGM polymorphism is associated with mortality of patients with severe sepsis. *PLoS ONE* 9: e91522

Kumar S, Jain A, Choi SW, da Silva GPD, Allers L, Mudd MH, Peters RS, Anonsen JH, Rusten TE, Lazarou M *et al* (2020) Mammalian Atg8 proteins and the autophagy factor IRGM control mTOR and TFEB at a regulatory node critical for responses to pathogens. *Nat Cell Biol* 22: 973 – 985

Kumar S, Jain A, Farzam F, Jia J, Gu Y, Choi SW, Mudd MH, Claude-Taupin A, Wester MJ, Lidke KA *et al* (2018) Mechanism of Stx17 recruitment to autophagosomes via IRGM and mammalian Atg8 proteins. *J Cell Biol* 217: 997 – 1013

Laroui H, Yan Y, Narui Y, Ingersoll SA, Ayyadurai S, Charania MA, Zhou F, Wang B, Salaita K, Sitaraman SV *et al* (2011) L-ala-gamma-D-Glu-meso-